# ENABLING INTERVENTIONAL MRI USING AN ULTRA-HIGH FIELD LOOPLESS ANTENNA

by
Mehmet Arcan Ertürk

A dissertation submitted to Johns Hopkins University in conformity with the requirement for the degree of Doctor of Philosophy

Baltimore, Maryland
April, 2014

# Abstract

Interventional magnetic resonance imaging (iMRI) utilizes multi-functional capabilities of MRI, for targeting therapy and monitoring response. Up to recently, most of the iMRI procedures have been conducted at magnetic field strengths ($B_0$) of 1.5T or lower. MRI at ultra-high $B_0$ (UHF, $B_0 \geq 3T$) provides higher signal-to-noise ratio (SNR) that can be traded for better image resolution and/or shorter scan durations. This dissertation investigates the performance of the interventional loopless antenna at UHF and introduces new methods to enable UHF iMRI using interventional loopless antennae.

First, a new MRI denoising method based on a spectral subtraction technique that can provide up to 45% of SNR improvement is introduced. While achievable SNR gains using post-processing methods are limited, the SNR of MRI is intrinsically improved by moving to higher $B_0$. Here, the performance of a loopless antenna was tested at 7T. The results show that SNR increases quadratically with $B_0$ ($SNR \sim B_0^2$) up to 7T. The increased SNR of the loopless antenna at UHF enables MRI at sub-50µm in-plane resolutions.

At UHF, excitation of tissue deep within the body becomes challenging due to the decreased penetration depth, and radiofrequency (RF) safety limitations when external coils are used. To overcome these problems, we used the loopless antenna for both transmitting the RF field, and receiving the MR signal from the tissue. Spatially

selective $B_1$-insensitive pulses were employed to improve the excitation homogeneity, providing a ~10cm FOV, which would be suitable for both device-tracking and localizing potential targets inside the body.

Use of interventional devices in transmit and/or receive mode may elevate temperatures near the device above levels considered safe. To address this problem, we built a loopless antenna RF radiometer operating at 3T MRI frequency, 128MHz, to monitor the local temperature around the device. We investigated its performance inside bio-analogous phantoms and using electromagnetic and thermal numerical simulations. The radiometer was able to detect uniform temperature with an accuracy <0.3°C at 2 measurements/second, and estimate the peak 1g-averaged temperature rise within 0.4°C. The loopless antenna radiometer can be used to ensure safety of interventional procedures, without requiring any additional leads or sensors, or even MRI.

*Advisor and first reader:* Prof. Paul A. Bottomley, PhD

Russell H. Morgan Professor, Department of Radiology and Radiological Science, School of Medicine, Johns Hopkins University

*Second reader:* Prof. Frederic M. Davidson, PhD

Professor of Electrical and Computer Engineering,

Whiting School of Engineering, Johns Hopkins University

this page is intended to be left blank

# Acknowledgments

I thank my advisor, Prof. Paul Bottomley, for his guidance and support throughout my studies. As a pioneer in the MRI field and an exemplary scientist, he has been a source of inspiration. He always prioritizes benefits of his students over his own and has been a great mentor. I deeply appreciate his guidance, admire his work ethic and personality. I am proud to be his student.

I thank Prof. Ergin Atalar from Bilkent University for introducing me to the field of MRI and encouraging me to pursue a career in MRI research. I am grateful for his friendly attitude and advices. I feel very lucky to work with Dr. AbdEl-Monem El-Sharkawy. I learned a lot from him and enjoyed working with him. He has been a great mentor, a very hard-working and a meticulous colleague. He always shared his wisdom and experiences with, and I consider him as an older brother. Without him, I would not be able to complete this work.

I feel privileged to be working in an environment surrounded by sincere and successful scientists; Prof. Bill Edelstein, Dr. Shashank Hegde, Dr. Michael Schär and Dr. Bob Weiss. They have not only provided scientific support and guidance, but also offered their friendship. I will never forget my favorite quote from Bill: '*Stay curious!*', he will be missed deeply. Mike has provided a tremendous help by sharing his knowledge on the Philips MRI systems. I appreciate Shashank's help during numerous experiments. His expertise and craftiness were vital in various parts of this study. I am grateful for

Bob's constructive comments, that culminated fruitful discussions during our weekly lab meetings. I also thank my labmates and colleagues working in other research labs, Dr. Di Qian, Yi Zhang, Guan Wang, Sahar Soleimanifard, Dr. Harsh Agarwal and Dr. Jing Yu for providing motivation and helping me to overcome the hurdles of the graduate student life. I enjoyed my time with their company. I will miss our daily lunch discussions ranging from scientific subjects to daily topics. I thank Peggy Herman for keeping everything running smoothly and Debbie Race for administrative help in the ECE Department. Last but not least, I thank my friends and colleagues in the Division of MR Research at the Johns Hopkins University.

I am thankful for my friends that I met in Baltimore for infusing fun and happiness into my life, and in no particular order I thank, Recep Özgün, Ozan Sayın, Tutkun Şen, Erbil Abaci, Alpay Hızal, Deniz Hızal, Orhan Ozgüner, Deniz Ayhan, Gökhan Karapınar, Buse Güven, Reyhan Taşpınar, Emre Oğuzöncül, Mustafa Köten, Sarper Güdek, Okay Kayaoğlu, Sezgi Nuzumlalı, Berk Gönenç, Burak Tekeş, Bora Erdemli, Jenny Poliwka, Areli Lopez, Viviane Lima, Leonel Maldonado, Eva Cunha, Miguel Bastos, Luciane Kagohara, Marisa Porro, Nuno Jorge, Lin Lock and Brett Linnenkohl for their company.

Support and friendship of my Turkish friends from my high school and college are very important for me. Time I spent traveling with my friends were among the highlights of my life. I thank Can Özvarlık, Emrecan Demirörs, Efecan Poyraz, Yusuf Yücel, Göktuğ Çınar, Özgür Balkan, İrem Bor, Sertaç Özdemir, Damla Hatipoğlu, Mehmet Koç,

Merve Yüksel, Sinan Yıldırım, Miraç Parlatan and Uğur Yıldız for their generous friendship.

Finally, I am grateful to my dear parents, Arzu and Özcan, my beautiful sister Mine Su, and my wise grandmother Zekiye Kaner; without their love, support and sacrifice, this journey would never have happened.

# Table of Contents

# List of Figures

# List of Tables

# Abbreviations

| | |
|---|---|
| $^{1}H$ | Proton |
| 2D | Two-dimensional |
| 3D | Three-dimensional |
| AHP | Adiabatic half passage |
| AU | Arbitrary units |
| BIR4 | Excitation field insensitive rotation adiabatic pulse |
| BW | Bandwidth |
| ECG | Electrocardiogram |
| EM | Electromagnetic |
| FA | Flip angle |
| FDA | U.S. Food and Drug Administration |
| FFE | Fast field echo |
| FFT | Fast Fourier Transform |
| FT | Fourier Transform |
| FOV | Field-of-view |
| GRE | Gradient echo |
| IEC | International Electrotechnical Commission |
| IV | Intravascular |
| MoM | Method-of-moments |
| MRI | Magnetic resonance imaging |
| NF | Noise figure |
| NMR | Nuclear magnetic resonance |
| Q | Quality factor |
| PSD | Power spectral density |
| RF | Radio frequency |
| SAR | Specific absorption rate |
| SD | Standard deviation |
| SENSE | Sensitivity encoding |
| SNR | Signal-to-noise ratio |
| SPGR | Spoiled gradient echo |
| SSD | Spectral subtraction de-noising |
| SSFP | Steady state free precession |
| T/R | Transmit/Receive |

# List of Symbols

| | |
|---|---|
| $B_0$ | Magnetic fields |
| $B_1^+$ | Transmit excitation field |
| ε | Dielectric constant |
| f | Frequency |
| γ | Gyro-magnetic constant |
| Hz | Hertz |
| i | Square root of -1 |
| j | Square root of -1 |
| K | Thousand |
| λ | Wavelength |
| $k_t$ | Thermal conductivity |
| μ | Magnetic permeability |
| M | Million |
| $M_0$ | Fully-relaxed magnetization |
| $M_{xy}$ | Transverse magnetization |
| $M_z$ | Longitudinal magnetization |
| Ω | Ohm |
| ρ | Mass density |
| r | Spatial location |
| s | Second |
| σ | Electric conductivity |
| T | Tesla |
| $T_1$ | Longitudinal relaxation |
| $T_2$ | Transverse relaxation |
| TE | Echo-time |
| TR | Repetition-time |
| X,Y,Z | Cartesian directions |
| ν | Spatial frequency |
| ω | Angular frequency |
| ΔT | Temperature change |
| ∇ | Gradient opearion |
| ∇ x | Curl operation |

# Chapter 1.

# Introduction

## 1.1. Interventional MRI

Magnetic resonance imaging (MRI) is a medical imaging modality that can provide exceptional soft-tissue contrast in any arbitrary imaging plane without ionizing radiation. MRI is considered a relatively safe imaging modality whose safety hazards are primarily limited to those associated with the effect of the magnetic field on metallic implants or peripheral equipments, and induced radiofrequency (RF) heating during MRI transmission. In addition to morphological information; it can provide functional and metabolic assessment on various biological processes.

Within a decade of its inception, MRI was used with an internal catheter coil for measuring heart metabolism[3]. The absence of ionizing radiation is not only important for the patient, but also for the operator who is routinely exposed to the scanner environment. Clinical MRI-guided (MRIg) interventional procedures began in 1980s using passive catheters visualized by their intrinsic material properties[4]. Development of open bore MRI systems[5], catheter tracking methods[6], design of active interventional imaging detectors[7, 8] and the advancement in fast imaging methods[9] paved the way for more advanced interventional MRI (iMRI) procedures. Breast and prostate biopsies[10-15], musculoskeletal procedures[16-19], endovascular and cardiac interventions[20-26], targeted stem cell delivery[27], various intracranial neurosurgical operations[28-31], radiofrequency

(RF) and microwave ablation[32-34], cryotherapy[35, 36] and MRIg-focused ultrasound (FUS) procedures[37-39] and many more applications, have been done under MRI guidance using MR compatible interventional tools, devices and robotics. Most but not all iMRI procedures have been conducted at field strengths 1.5 Tesla (T) or lower. MRI at or above 3T field strength ($B_0$) offer potential improvements in image quality and/or speed due to the higher signal-to-noise ratio (SNR) available. However, device safety is a concern at higher $B_0$ due to magnetic displacement forces, RF heating and biocompatibility issues. These must be addressed and the performance gains for interventional devices and their pulse sequences at ultra-high field strengths (UHF; $B_0 \geq 3T$) must be analyzed in order to proceed.

Devices used under MRI-guidance can be visualized by either passive or active mechanisms. With passive visualization mechanisms, the device appears in the image by virtue of its intrinsic material properties. Some devices create a signal void in the image and appear darker compared to the background[40]. Devices including ferrous materials can be visualized by their susceptibility artifacts[41]. Devices filled[42] or coated[43] with MRI contrast agents appear hyper-intense. Passive visualization methods do not require additional hardware and/or modifications to the MRI system[40].

Active interventional detectors generally employ small tracking coils that are sensitive to the MR signal [6, 44]. The coil is connected to the MRI scanner via a thin coaxial cable and provides a robust signal, identifying the location of the instrument with high contrast. The available spatial coordinates of the device in 3-dimensions can be used to

update the imaging location in real-time, such that imaging is always performed at the catheter position [45-47].

Tracking coils provide only point-wise spatial information. When the number of tracking coil is limited, visualizing the curvature and the entire length of a catheter, say, is challenging. However, the curvature and the entire length of a catheter can be actively visualized using magnetically coupled coils[48, 49] or electrically coupled antennas [8, 50]. The loopless antenna[8] is an electrically coupled MRI antenna, that can provide homogeneous signal profile along a substantial length of the antenna lead. Signal sensitivity is such that the MR signal derives from tissue in close vicinity to the antenna. MRI signal acquired from the loopless antenna can be overlaid with a different color on a body coil image to visualize the device location. In addition to superior device visualization, the loopless antenna can be used to acquire MRI signal to produce high-resolution images of tissues nearby[7, 51, 52]. It can also be used to provide MRI excitation[53].

Active visualization methods require dedicated hardware, electronics and MR software modifications to take advantage of their capabilities. Detuning/decoupling of the active devices during external RF excitation is important to ensure their safety[40, 54]. Tuning/matching of them during MR signal reception is also required to achieve the optimal performance[8].

## 1.2. RF Safety

MRI is not considered a significant risk for health and has a significant safety record, however it is not totally hazard-free. In MRI, the magnetic field component of the RF field ($B_1$) at the Larmor frequency excites the spins to generate the MRI signal. The electric field ($E_1$) associated with this RF excitation induces RF (high-frequency) eddy currents in the conducting tissue[55] and may cause temperature elevations. The RF power exposure is quantified by the specific absorption rate (SAR). The SAR is the mass normalized rate at which RF power is coupled to the biologic tissue[56], measured in W/kg.

**Table 1.1.** International Electrotechnical Comission (IEC) in Europe and the U.S. Food and Drug Administration (FDA) guidelines on SAR and heating in human MRI studies are listed.

| **IEC limits (6 min average)** | **Whole body average** | **Head average** | **Head, torso local SAR** | **Extremities Local SAR** |
|---|---|---|---|---|
| **Normal (all patients)** | 2 W/kg (0.5°C) | 3.2 W/kg | 10 W/kg | 20 W/kg |
| **First level (supervised)** | 4 W/kg (1°C) | 3.2 W/kg | 10 W/kg | 20 W/kg |
| **Second level (IRB approval)** | 4 W/kg (>1°C) | >3.2 W/kg | >10 W/kg | >20 W/kg |
| **Localized heating limit** | 39°C in 10g | 38°C in 10g | | 40°C in 10g |
| **FDA limits** | 4 W/kg for 15 min | 3 W/kg for 10 min | 8 W/kg in 1g for 10min | 12W/kg in 1g for 5 min |

The safety of RF exposure during clinical MRI is regulated via government and industry guidelines [57, 58]. RF exposure limits published by the International

Electrotechnical Commission (IEC) in Europe and the U.S. Food and Drug Administration (FDA) are summarized in Table 1.1. RF exposure settings under MRI in research studies may exceed the clinically approved exposure limits pending an approval from an instituitional review board (IRB).

The power absorption pattern inside a biological sample depends on both parameters intrinsic to the sample such as its size and electrical properties, and also the RF excitation coil, Larmor (MRI) frequency, the presence and positioning of any conductor and/or internal detector inside the sample and excitation coil. The SAR distribution inside the sample cannot easily be measured directly, however it can be modeled using accurate numerical analysis methods[59-61], and estimated based on the whole body average input power or SAR. Clinical scanners monitor both the average and local SAR based on individual patient data entries, and/or factory-determined properties of transmit coils and estimates of the delivered power[62, 63]. Although rare, RF heating related injuries occur every year. Examples of reported RF burn injuries can be found in the FDA Manufacturer and User Facility Device Experience (MAUDE) database [64].

The presence of a highly conductive metallic device inside the body will typically alter the distribution of $E_1$. Potential capacitive coupling between the device and the surrounding tissue can exacerbate RF safety risks[65, 66]. Because the conductivity of a metallic device is significantly higher than the surrounding tissue, the current in the device can be much higher than in the surrounding tissue. At the entrance (and exit) points of a metallic device inside the body, the local current density in the tissue may be

high enough for burns to occur[40]. The exact current densities and heat production are difficult to predict because they not only depend on the metallic device but also on the RF excitation coil, surrounding tissue electrical properties as well as the exact location of the device inside the body and in the coil. Device testing using a setup according to ASTM standard F2182[67] does not necessarily ensure a 'worst case situation', and testing in typical clinical settings also may not provide proof of safety under all circumstances. It is desirable to have an independent way of monitoring the local heating around an interventional device in order to monitor safe operation.

## 1.3. Outline of the Thesis

The purpose of this thesis is to characterize the performance of active interventional loopless antenna detectors at ultra high field strengths (UHF, $B_0 \geq 3T$), and develop methods to enable their use at UHF. First, the SNR performance and RF safety of the loopless antenna at UHF is investigated. Then, to overcome the challenges with RF excitation at UHF, the loopless antenna is used for both transmitting the RF field with a spatially selective $B_1$-insensitive RF pulse, and for receiving the MRI signal at 7T. This transmit/receive approach with the interventional loopless antenna helps to eliminate some system complexities at 7T. In the last part of the thesis, the loopless antenna is used as an RF radiometer to measure the local temperature rise around the device. A loopless antenna RF radiometer may be used to monitor the safety of interventional procedures in the future.

In the first chapter, background information on interventional MRI and RF safety are discussed. The second chapter explores the fundamentals of MR physics and MR image reconstruction, potentials and challenges of UHF imaging, and the advanced MRI methods used throughout the work. The latter include sensitivity encoding (SENSE)[68], chemical selective imaging[69] and temperature mapping with MR thermometry[70]. MRI RF coils are briefly discussed. The design and implementation of an interventional loopless antenna upon which this thesis is based is introduced.

In Chapter 3, we introduce an MRI de-noising method based on the subtraction of the noise power from the acquired signal in the spatial frequency domain. The proposed method is tested on various single coil images as well as on multi-channel coil images reconstructed using SENSE algorithm.

In Chapter 4, the SNR performance and RF safety of the loopless antenna is investigated at 7T and the results are compared with 3T. High-resolution images (in-plane voxel size: < 100μm) of diseased human artery specimens are acquired.

In Chapter 5, methods for chemically-selective intravascular imaging of atherosclerotic plaques are discussed. Chemically-selective water/fat MRI methods using three-point Dixon method[69] and spectrally selective modified $B_1$-insensitive rotation (BIR4) pulses[71] are demonstrated.

In Chapter 6, brain specimens with and without Alzheimer's disease pathology are scanned at high-resolution (60x60x200$\mu m^3$) using the loopless antenna at 7T. Amyloid plaque-like signal hypointensities are detected from specimens with the

disease pathology.

In Chapter 7, MRI excitation is provided solely with the loopless antenna, using spatially-selective $B_1$-insensitive RF pulses[72] at 7T. A single-device approach without any RF coils/detectors other than the interventional loopless antenna is successfully introduced, removing the need of external coils and reducing the system complexity.

In Chapter 8, an RF radiometer tuned to 3T MRI Larmor frequency (128MHz) is built and connected to the loopless antenna to monitor local temperature around the device. The proposed method is tested experimentally inside bio-analogous uniform phantoms and numerically using full-wave electromagnetic (EM) and thermal simulations.

In Chapter 9, major achievements are summarized chapter by chapter and future work is explained.

# Chapter 2.

# Background

## 2.1 NMR Physics

### 2.1.1. Main Magnetic Field ($B_0$)

Atoms with an odd number of nucleons posses magnetic moment, and when placed in a static magnetic field ($B_0$), the net spin magnetization (M) preferentially aligns in the direction of $B_0$ [73] (Figure 2.1.a, traditionally assigned to Z-direction). The nuclear spins resonate at the Larmor frequency (f), which is directly proportional to the $B_0$:

$$f = \frac{\gamma}{2\pi} B_0 \qquad \textbf{[2.1]}$$

where γ is the gyromagnetic ratio which is a known unique constant for each atom, i.e. isotope. The phenomenon is called nuclear magnetic resonance (NMR). In biological specimens, hydrogen ($^1$H) is the most abundant atom, that gives rise to the largest signal and therefore is the most studied by MRI. The gyromagnetic ratio of hydrogen ($\gamma/2\pi$) is 42.58MHz/Tesla. For a clinical 3T system, the Larmor frequency is about 128MHz; and it increases to 298MHz for 7T systems used in pre-clinical research.

### 2.1.2. Radiofrequency Field ($B_1$)

To obtain an NMR signal, a radiofrequency (RF) magnetic pulse ($B_1$) tuned to the Larmor frequency is applied in the transverse (xy) plane. This RF pulse excites spins away

from equilibrium and tilting them, for example, towards the xy-plane (Figure 2.1.b). The angle of rotation (FA: flip angle) is a function of the amplitude, frequency and duration of the applied RF pulse[74]. The transverse magnetization ($M_T$=$M_{xy}$) precesses at the Larmor frequency and gives rise to the NMR signal (Figure 2.1.c), and the NMR signal is picked up using NMR receiver coils tuned to the Larmor frequency.

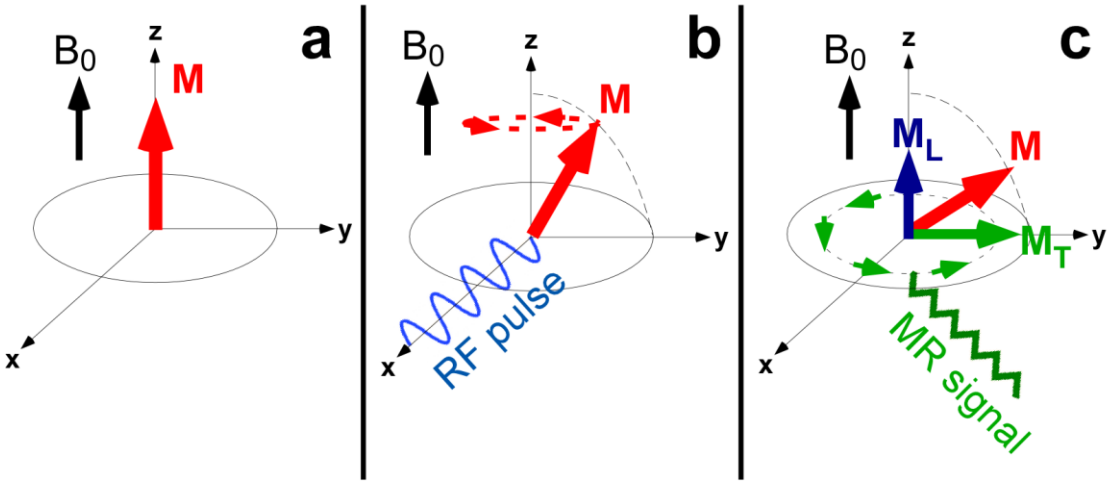


**Figure 2.1.** (a) The net magnetization aligns with the $B_0$ (z-direction). (b) An RF pulse applied along the transverse plane (xy-axis) at the Larmor frequency tilts the magnetization towards the transverse plane. (c) The transverse component of the magnetization ($M_T$) precesses at the Larmor frequency and it is the source of the NMR signal.

## 2.1.3. Bloch Equation

The behavior of the spin magnetization in the presence of an externally applied magnetic field is governed by the Bloch equation [75]:

$$\frac{d\vec{M}}{dt} = \vec{M} \times \gamma \vec{B} - \frac{(M_z - M_0)\vec{z}}{T_1} - \frac{M_x \vec{x} + M_y \vec{y}}{T_2} \qquad \textbf{[2.2]}$$

where $\vec{M}$ is the spin magnetization; $M_0$ is the equilibrium magnetization arising from

$B_0$; $\vec{B}$ is the applied magnetic field; $T_1$ and $T_2$ are the relaxation time constants in the longitudinal (z-dimension) and transverse planes respectively.

## 2.1.4. Relaxation

When the applied RF field is removed, spin magnetization returns to the equilibrium magnetization ($M_0$). The $T_1$ and $T_2$ relaxation times define the characteristic time at which the longitudinal magnetization reaches $M_0$, and the transverse magnetization decays to zero, respectively. For magnetization tipped into the transverse plane at time t=0, the relaxation processes can be written:

$$M_z = M_0(1 - e^{-t/T_1}) \quad \textbf{[2.3]}$$

$$M_T = M_0 e^{-t/T_2} \quad \textbf{[2.4]}$$

The $T_1$ and $T_2$ relaxation times are properties of the tissue, and the differences in the relaxation constants are generally responsible for the contrast between different tissues seen in MRI.

## 2.1.5. Signal Acquisition

The NMR signal is detected by an NMR coil which may be are sensitive to the entire imaging volume or to local regions of interest. The NMR signal is induced in the coil V(t) according to Faraday's law of induction:

$$V(t) = -\frac{\partial}{\partial t} \int_{subject} \vec{B}_{coil}(r) \bullet \vec{M}(r,t) dr \quad \textbf{[2.5]}$$

where $\vec{B}_{coil}(r)$ is the magnetic field produced at a location $r$ by unit current flowing inside the receiver coil based on the principle of reciprocity. The NMR signal induced in the coil is a weighted summation of all the spin magnetization over the region to which of the RF coil is sensitive.

### 2.1.6. Linear Gradient Fields

If the net applied magnetic field is $B_0$, then all the spins inside the imaging volume precess at the same frequency, and it would not be possible to resolve the spatial origin of the induced signal. Linear gradient magnetic fields (G) are used for spatial localization in MRI. The linear gradient fields are applied in the z-direction, therefore the net magnetic field points in the same direction. However, the strength of the linear gradient fields vary in position and spins at different locations precess at different frequencies:

$$\omega(x, y, z) = \gamma(B_0 + G_x x + G_y y + G_z z) \quad \textbf{[2.6]}$$

where $G_x$, $G_y$ and $G_z$ are the amplitudes of the linear gradient fields in the x, y and z directions respectively.

## 2.2. MR Image Encoding and Reconstruction

### 2.2.1. Spin Warp MRI

In a simple 2D imaging sequence, the imaging slice is excited by applying an RF pulse together with the slice selection gradient ($G_s$). Only the spins precessing at

frequencies within the bandwidth of the applied RF pulse will be excited. The thickness and shape of the selected slice is a function of the amplitude of the applied gradient field; and the amplitude, center frequency and the bandwidth of the RF pulse.

After a slice is selected, the linear gradients in the other two directions ($G_p$: phase-encoding gradient, $G_f$: frequency-encoding gradient) are used to spatially encode the sample in the other two dimensions (2D). The RF and gradient waveforms for the 2D spin warp imaging sequence is shown in Figure 2.2 [76]. The MRI signal voltage induced in the coil for a slice selected in the z-direction, ignoring relaxation and field inhomogeneity effects, is given by:

$$M_{xy}(t) \propto \int_x \int_y M_0(x,y) e^{-i2\pi(k_x+k_y)} dydx \qquad \textbf{[2.7]}$$

where $k_x = \frac{\gamma G_x t}{2\pi}, k_y = \frac{\gamma G_y t}{2\pi}$ denote the spatial frequencies.

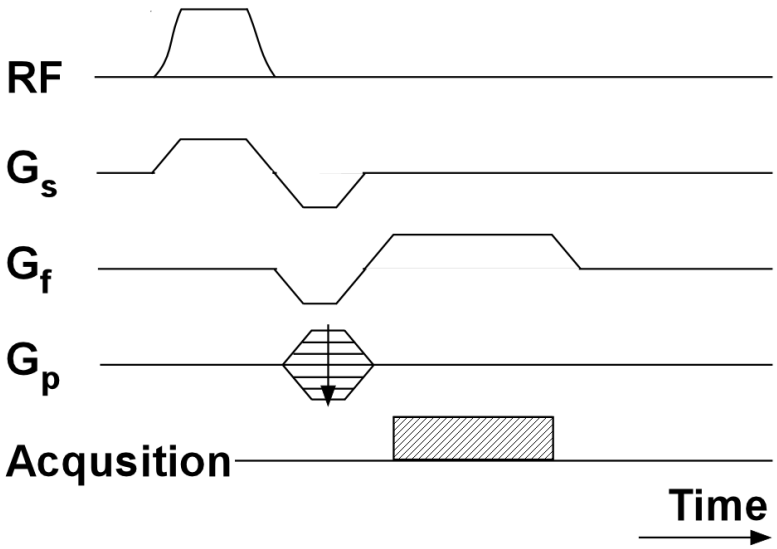


**Figure 2.2.** 2D Spin warp imaging sequence is displayed.

Repeating the spin warp sequence with different phase encoding gradient amplitudes fills up the spatial frequency domain (k-space) of the image (Figure 2.3.a). Eq. [2.7] indicates a Fourier transform (FT) relationship between the acquired MRI signal and the MRI. Therefore, taking the 2D FT of the acquired samples (Figure 2.3.b) yields the 2D MRI (Figure 2.3.c).

The image resolution and field-of-view (FOV) depend on the acquisition parameters:

$$\delta_p = \frac{1}{2k_{p,\max}}, \delta_f = \frac{1}{2k_{f,\max}} \quad \textbf{[2.8]}$$

where $\delta_p, \delta_f$ are the spatial resolution in the phase and frequency encoding directions respectively. The imaging FOV is related to the step-size between each k-space sample:

$$FOV_p = \frac{1}{\Delta k_p}, FOV_f = \frac{1}{\Delta k_f} \quad \textbf{[2.9]}$$

where $FOV_p, FOV_f$ are imaging FOV; and $\Delta k_p, \Delta k_f$ are the distance between the adjacent k-space samples in the phase and frequency encoding direction, respectively.

## 2.2.2. Gradient Echo (GRE) Pulse Sequence

Gradient echo (GRE) pulse sequences are primarily used for fast scanning[77], and in applications requiring acquisition speed such as vascular or cardiac imaging[78]. GRE has three main parameters: 1. RF excitation flip angle (FA); 2. echo time (TE); 3. sequence repetition time (TR). The common features of GRE sequence are shown in Figure 2.4.

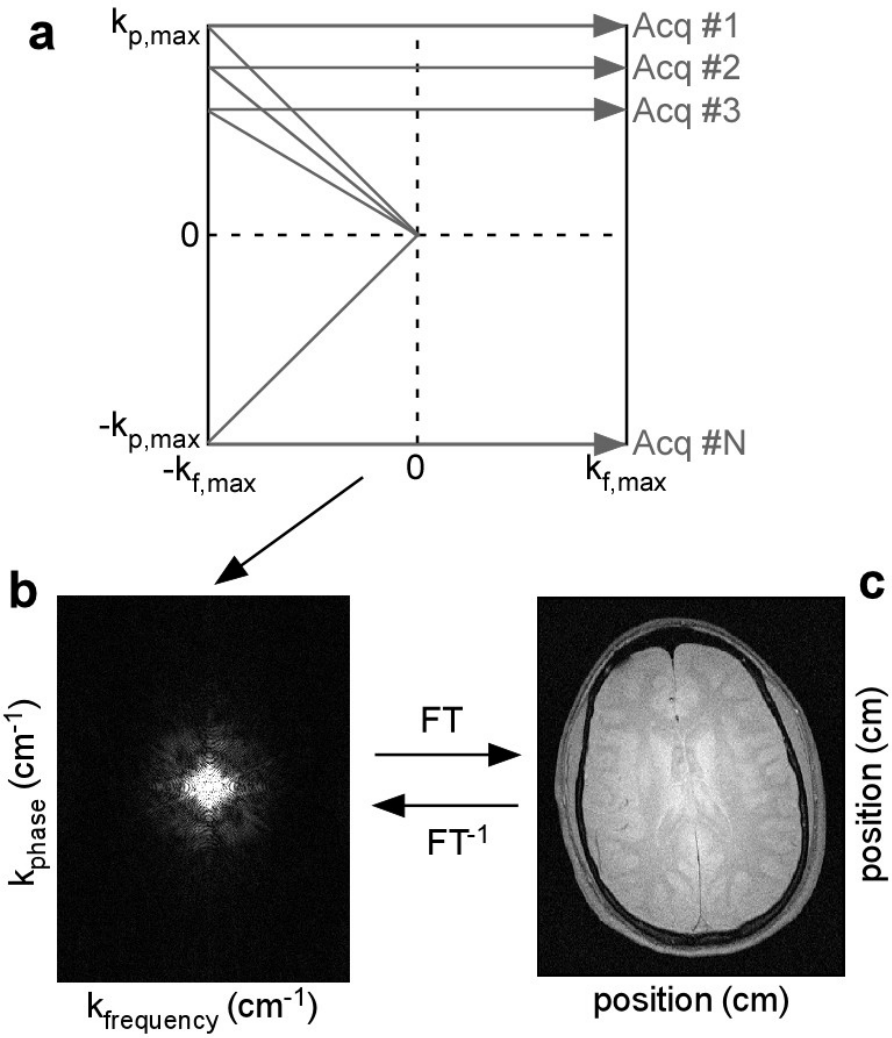


**Figure 2.3.** (a) The structure of k-space with respect to the phase and frequency encoding gradients are shown. (b) After the k-space is filled with MR signal samples, taking the 2D Fourier transform yields the (c) MR image.

GRE acquisitions can be fast because the excitation FA is typically less than 90°, therefore some of the longitudinal component of the magnetization can be used in the next TR and no lengthy period of time is required for $T_1$ recovery. TR of GRE sequences are generally less than 200ms. The $T_1$ contrast of the image can be adjusted by changing FA and TR.

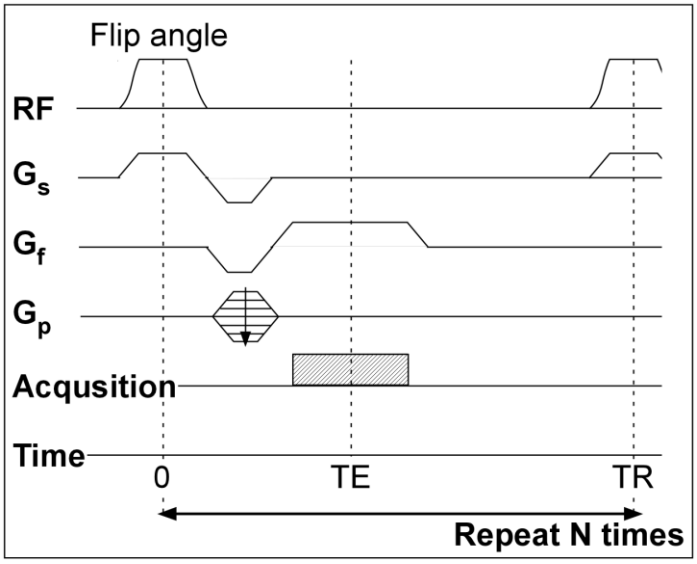


**Figure 2.4.** Timing and placement of the RF and gradient fields for a simple GRE sequence are depicted. Repeating this sequence N times with different phase encoding gradient value will fill up the k-space.

GRE sequences are weighted with $T_2$* (apparent $T_2$), which is related to the spin-spin relaxation time ($T_2$) by:

$$\frac{1}{T_2^*} = \frac{1}{T_2} + \frac{1}{T_2'} \qquad \textbf{[2.10]}$$

where $T_2$' is inversely proportional to the magnetic field inhomogeneity inside each voxel. $T_2$' depends on external factors such as susceptibility variations within the patient and prescribed imaging voxel size, however $T_2$ is an intrinsic tissue property.

Steady state signal equation for a spoiled GRE sequence in which the residual transverse magnetization is crushed at the end of each TR is given by:

$$S_{GRE} \propto \sin(FA) \cdot e^{-TE/T_2^*} \cdot \frac{1 - e^{-TR/T_1}}{1 - \cos(FA) \cdot e^{-TR/T_1}} \qquad \textbf{[2.11]}$$

showing that GRE signal depends on the choice of TR, TE and FA; as well as the tissue $T_1$

and $T_2$ values.

Another important feature of GRE is that, the resultant images contain phase information, which can be utilized in MRI methods such as susceptibility weighted imaging[79, 80], temperature mapping[70, 81], and chemically-selective imaging[82, 83].

## 2.2.3. Parallel Image Reconstruction

In spin wrap imaging, the pulse sequence must be repeated N times to fill up image k-space, however this can be time consuming. In order to reduce the scan time, phased-array coils[84] can be used with parallel imaging algorithms such as simultaneous acquisition of spatial harmonics (SMASH)[85], sensitivity encoding (SENSE)[68] and generalized auto calibrating partially parallel acquisition (GRAPPA)[86].

"Parallel" refers to the fact that each coil in the RF coil array receives the MR signal at the same time. In a parallel imaging experiment, a certain number of phase encoding steps are intentionally skipped. Taking the FT of the incomplete dataset results in image wrapping (Figure 2.5). Parallel imaging methods works by knowing the local sensitivity of each coil element in the receiver array and incorporating the coil sensitivity information with the incomplete dataset acquired from all of the elements.

The GRAPPA method works by filling the missing k-space lines using an automatic calibration kernel. For an acceleration factor of 2, every other k-space line is skipped, however a few additional lines are acquired at the center of the k-space to generate the calibration kernel. Then using this kernel, the remaining missing k-space lines are filled and final image is reconstructed by taking the FT.

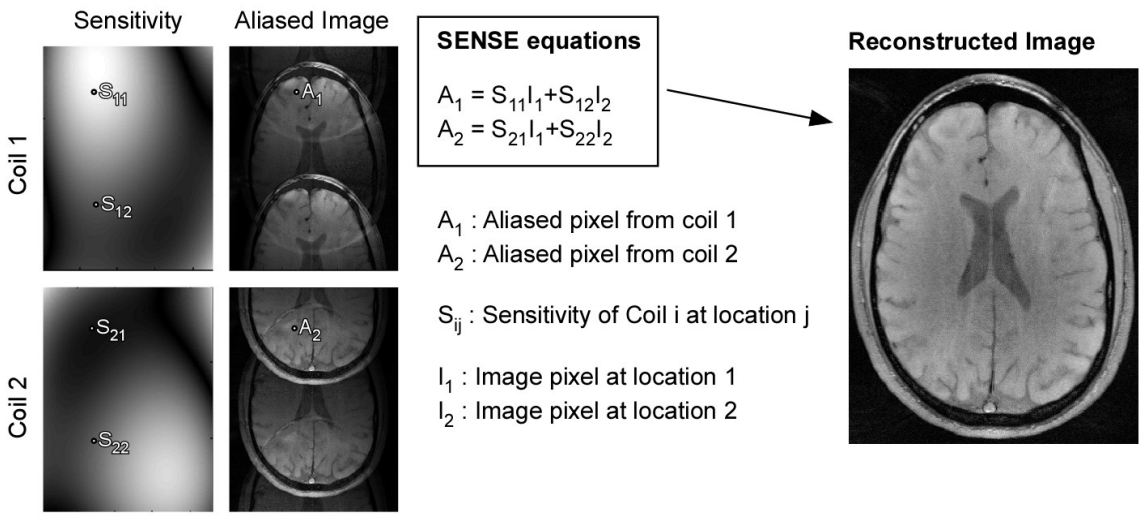


**Figure 2.5.** The SENSE reconstruction algorithm is explained.

The SENSE method operates on the image domain and needs an additional pre-scan to measure the sensitivity of the coils. If an acceleration factor of 2 is used, then every pixel in the aliased image come from two locations at a distance of exactly 1/2 FOV apart. It is also known that the pixels are weighted by the sensitivity of the coil. By knowing the aliasing pattern and the spatial sensitivities of different coil elements, a linear equation can be solved to retrieve values of these two pixels. The SENSE reconstruction method is illustrated with a reduction factor of 2 along with the linear SENSE reconstruction equations in Figure 2.5.

## 2.3. Ultra-high Field MRI ($B_0$>3T)

In the absence of an external magnetic field, spin magnetic moments in water in biological tissue are generally randomly distributed from a macroscopic perspective. Therefore, the net magnetization is 0. In the presence of a static magnetic field ($B_0$), the

net magnetic moment tends to align in the direction of $B_0$, counteracted by the thermal energy which ensures that some spins are not aligned with $B_0$. In the quantum mechanical descriptions in a spin-1/2 nucleus can be aligned with and against $B_0$, with a distribution at thermal equilibrium governed by Boltzmann statistics[87]:

$$N_{\uparrow} = N_{\downarrow} e^{(\gamma \hbar B_0)/(k_B T)} \quad \textbf{[2.12]}$$

where $N_{\uparrow}$, $N_{\downarrow}$ are the number of parallel and anti-parallel spins in a given volume, $\gamma$ is the gyromagnetic ratio of the nucleon, $\hbar$ is Planck's constant, $T$ is the absolute temperature. Since the argument of the exponential term in Eq. [2.12] is much smaller than 1 (generally on the order of $10^{-6}$), it can be approximated using a linear term in the Taylor series expansion. The net magnetization is proportional to the difference between the number of parallel and anti-parallel spins in a given volume, and it is also proportional to $B_0$:

$$M \propto \left[N_{\uparrow} - N_{\downarrow}\right] = \frac{\gamma \hbar B_0}{k_B T} \quad \textbf{[2.13]}$$

In other words, moving to higher $B_0$ linearly increases the available longitudinal magnetization and potentially increase the SNR of MRI. Higher available NMR signal is the main reason of the effort in moving to higher $B_0$. In present, 3T is the highest approved field strength for clinical imaging. However, there are more than fifty 7T MRI scanners either installed or planned worldwide[88]. A 10.5T human MRI scanner is planned to become operational in 2014, that would make it the whole-body human scanner with the highest $B_0$[89].

Moving to higher $B_0$ is challenging due to RF penetration problems[90], increased RF power requirements[91-94], increased susceptibility effects[95, 96] and dielectric resonances[97, 98]. The required RF power increases approximately quadratically with $B_0$ for fixed FA and pulse length from 1.5 to 4T[91, 94, 99, 100] and is expected to increase linearly from 4T to 7T[101, 102]. At higher field strengths ($B_0$>3T), conventional RF management strategies usually become inadequate and novel methods are being developed to overcome these challenges.

RF field inhomogeneities due to dielectric resonances[103] and penetration effects may be tackled using phased-array coils[104, 105]. Static and dynamic $B_1$ shimming methods[106-113] have also been developed for imaging different parts of the body. Uniform field excitation and SAR reduction are the main goals of RF management strategies which are application-dependent and remain an active area of research [114-118].

## 2.4. MRI RF Hardware

### 2.4.1. MR Coil SNR vs Field Strength ($B_0$)

The NMR signal voltage ($V_s$) generated in an RF coil is calculated using[8]:

$$V_s = \omega B_1 M_0 \qquad \textbf{[2.14]}$$

where $M_0$ is the amplitude of the equilibrium magnetization. The MRI Larmor frequency is proportional to the $B_0$, and $M_0$ increases linearly with $B_0$, therefore the signal voltage induced in the RF coil increases quadratically with $B_0$, assuming equivalent coils at every field strength:

$$V_s \propto \omega^2 B_1 \quad \textbf{[2.15]}$$

The RMS noise voltage, $V_N$ in the coil is calculated as:[8]

$$V_N = \sqrt{4k_B \cdot T \cdot R \cdot BW} \quad \textbf{[2.16]}$$

where $k_B$ is Boltzmann constant, T is the absolute sample temperature, R is the net measured resistance of the coil with the sample in it, and BW is the bandwidth of the signal receiver. Using equations [2.15] and [2.16], the SNR of the coil can be expressed as:

$$SNR = \frac{V_s}{V_N} \propto \frac{\omega^2}{\sqrt{R}} \quad \textbf{[2.17]}$$

The noise voltage can be divided into two components; the coil noise, and the sample noise. The coil noise is proportional to $\alpha\omega^{\frac{1}{2}}$, where α is a coil dependent parameter[90]. The sample noise stems from dielectric (electric) and inductive (magnetic) losses. In large coils, dielectric losses can be alleviated by distributing the capacitors. The inductive loss for a spherical sample volume is proportional to $\beta\omega^2$, where β is a coil and sample dependent parameter. Therefore, the field dependence of the coil SNR can be written as:

$$SNR \propto \frac{\omega^2}{\sqrt{\alpha\omega^{\frac{1}{2}} + \beta\omega^2}} = \frac{{B_0}^2}{\sqrt{\alpha {B_0}^{\frac{1}{2}} + \beta {B_0}^2}} \quad \textbf{[2.18]}$$

The porportionality [2.18] shows that if the coil losses are minimized and the sample noise dominates, then SNR increases linearly with $B_0$. On the other hand, if the

coil conductive losses dominate, then $SNR \propto B_0^{\frac{7}{4}}$ [119]. For larger coils, generally sample noises dominates and therefore SNR varies linearly with $B_0$. For small loop coils, coil conductive losses can dominate and the SNR increases more-than-linearly with $B_0$[119].

## 2.4.2. Interventional Loopless Antenna

The "loopless antenna"[8] is an interventional MRI detector that can be manufactured in sub millimeter dimensions[120]. It is built by extending the inner conductor of a coaxial cable to form a resonating structure (whip) inside the medium at the MRI frequency. The antenna's sensitivity may be improved by dielectric insulation[121] and tapering the insulation on the whip[122].

The signal level of the loopless antenna is the lowest at the tip of the whip where the current is minimized, and it is maximum at the cable-whip junction where the inner conductor extends out of the coaxial cable structure.

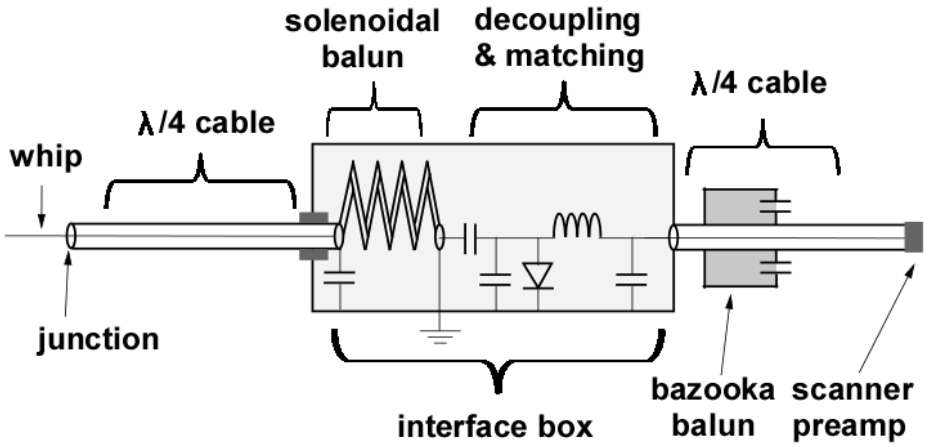


**Figure 2.6.** Circuit diagram of a receive-only loopless antenna and matching & decoupling circuitry is shown.

A circuit diagram of a receive-only loopless antenna is shown in Figure 2.6. A coaxial cable having a length of an odd multiple of the quarter wavelengths is connected to the interface box. The interface box generally contains a solenoidal balun to suppress the common mode currents in order to reduce unwanted coupling to the external conductive structures such as the external MRI coil. The decoupling circuitry includes a diode that can be activated during RF transmission so that the whip encounters a large impedance and the currents induced on the antenna due to external RF fields are minimized. The matching circuitry is used to maximize the signal transmission efficiency to the MRI receiver electronics. The whip and cable of a nitinol biocompatible loopless antenna is shown in Figure 2.7.

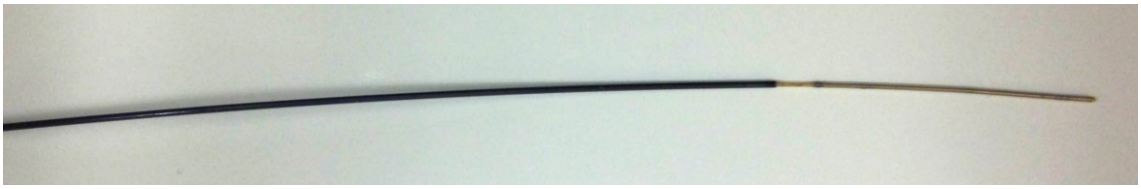

**Figure 2.7.** Whip and cable of a biocompatible loopless antenna made out of nitinol hypertube and an insulated gold-plated nitinol center conductor. Antenna diameter is 0.86mm.

## 2.4.3. Baluns

Baluns are used to suppress common mode currents (CMC) on the outer shield of coaxial cables that connect coils and different hardware components of the MRI RF transmit/receive chain. CMC can cause: a reduction in SNR[78], unwanted coupling between receive coil elements in receive arrays[77, 78], and increased interactions between the cable and the RF transmit field, that may exacerbate RF safety risks. Proper design

and placement of baluns along RF coaxial cables is crucial for optimum RF hardware performance.

In this thesis, numerous bazooka baluns tuned to 3 and 7 Tesla MRI frequencies are used. A cross-sectional view of a bazooka balun along with its representative circuit diagram is shown in Figure 2.8 [123].

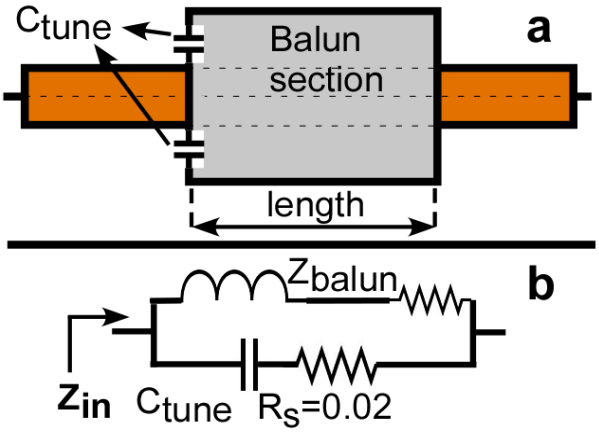


**Figure 2.8.** (a) Schematic and (b) circuit diagram of a bazooka balun.

**Figure 2.9.** A bazooka balun implemented on a semi-rigid coaxial cable is shown. Left end of the balun structure is soldered to the outer conductor of the coaxial cable. Balun is tuned to the operating frequency using the capacitors placed between the right end of the balun structure and the outer conductor of the coaxial cable.

Bazooka baluns (Figure 2.9) generally have a narrow band and are highly effective common-mode suppressors. The common mode suppression efficiency of a bazooka balun can be improved by increasing the inductance of the balun. For a given

coaxial cable, a longer and or thicker inductive balun section will generally provide a higher common mode impedance when it is tuned to the operating frequency Figure 2.10[123].

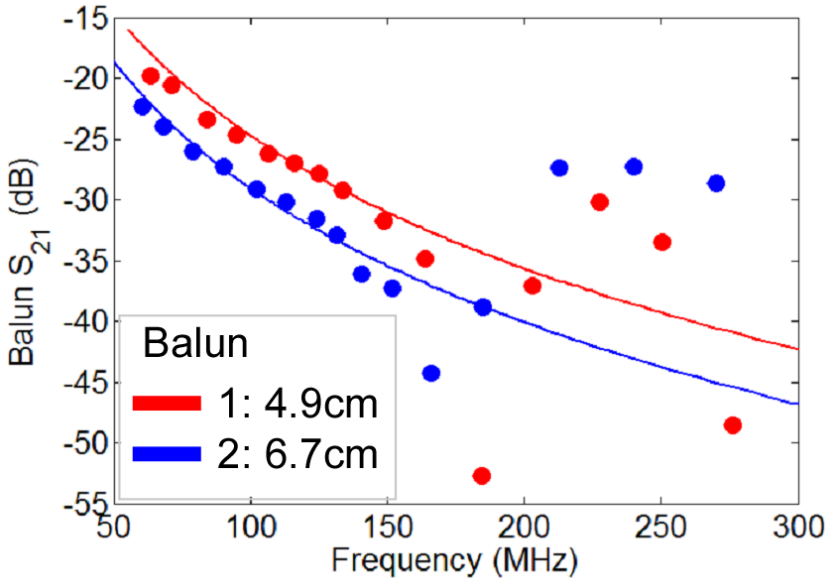


**Figure 2.10.** Common-mode impedances of two bazooka baluns with lengths of 4.9cm (red) and 6.7cm (blue) are plotted with dotted lines at different tuning frequencies. The solid lines show the analytically calculated impedance values at respective tuning frequencies.

## 2.5. Advanced MRI Methods

In this section, some of the advanced MRI methods that are used throughout the thesis are introduced. First, chemically-selective imaging using the three-point "Dixon method" [69] to distinguish water and fat content is explained. In the second part, temperature mapping using proton-resonance frequency (PRF) shift method[70] is discussed.

## 2.5.1. Chemically Selective Imaging

Water and lipid protons resonate at NMR frequencies 3.4ppm (parts per million; 435Hz at 3T amd 1015Hz at 7T) apart from each other, for a given applied magnetic field. This difference between their precession frequencies can be utilized to distinguish the water and fat content of the subject.

One approach, proposed by Dixon, is to acquire a series of images at different echo times and to reconstruct water- and fat-only images using the phase information[82]. In the three-point Dixon method, three images are acquired at different TEs but otherwise identical sequence parameters [69]:

$$\begin{aligned} S_1 &= (water + fat)e^{\phi}e^{-\phi_0} \\ S_2 &= (water + fat)e^{\phi} \\ S_3 &= (water + fat)e^{\phi}e^{\phi_0} \end{aligned} \quad \textbf{[2.19]}$$

where $S_i$ denotes the image acquired at $i^{\text{th}}$ TE; $water$ and $fat$ denote the water and fat content in the image, respectively; ϕ represents the combined phase accumulation due to the pulse sequence, coil and sample configuration; and $\phi_0$ denotes the phase accumulation due to inhomogeneities in the main magnetic field ($\Delta B_0$). After calibrating each acquisition against the systematic phase accumulation:

$$\overset{\Delta}{S}_i = S_i e^{-\phi} \quad \textbf{[2.20]}$$

water- and fat-only images are calculated using:

$$water = \overset{\Delta}{S}_2 + \sqrt{\overset{\Delta}{S}_1 \overset{\Delta}{S}_3}$$
$$fat = \overset{\Delta}{S}_2 - \sqrt{\overset{\Delta}{S}_1 \overset{\Delta}{S}_3} \qquad \textbf{[2.21]}$$

where $\overset{\Delta}{S}_i$ are the phase normalized images according to Eq. [2.5].

## 2.5.2. MR Thermometry

The resonance frequency of $^1$H in water molecules decreases slightly as the temperature increases, due to the molecular screening of water molecules giving rise to a temperature dependent decrease in local magnetic field. The temperature dependence of the molecular screening constant for pure water is α=-0.01 ppm/°C [81].

Although the shift is tiny, magnetic field inhomogeneities and/or drifts are measurable using the phase of gradient-echo MRI. By repeating the same pulse sequence, the temperature difference between two acquisitions can be derived from the phase differences. This is using the proton resonance frequency (PRF) shift method of MRI thermometry [124]. The temperature change is given by:

$$\Delta T_i = \frac{\phi_i - \phi_0}{\gamma \alpha B_0 TE} \qquad \textbf{[2.22]}$$

where $\Delta T_i$ is the calculated temperature difference map and $\phi_i$ is the phase image at the i$^{th}$ time frame, $\phi_0$ is the reference phase image, $\gamma$ is the gyro-magnetic ratio of $^1$H, $\alpha$ is the temperature coefficient of the PRF change, and $B_0$ is the main magnetic field strength.

The sensitivity of the MR thermometry method is improved at higher $B_0$, because the effect is proportional to field or frequency in ppm, and the measurements are in Hz. The effect is also optimized by setting (TE=T2*) [125]. If the phase difference between two images is greater than $\pi$, temperature measurements may become corrupted due to phase wraps or aliasing. This can be solved using post-processing methods, by assuming that the temperature distribution is slowly varying.

# Chapter 3.

# De-Noising MRI Using Spectral Subtraction

## 3.1. Introduction

Improving signal-to-noise ratio (SNR) in MRI without sacrificing spatial resolution, contrast or scan-time could improve diagnostic value. While time averaging increases SNR, with SNR $\propto \sqrt{}$(scan-time), extending the scan-time is expensive, prone to motion artifacts, and unacceptable in many clinical MRI applications. Indeed, parallel imaging techniques such as sensitivity encoding (SENSE) [68] and generalized auto-calibrating partially parallel acquisitions (GRAPPA) [86], are commonly used to shorten scan-times. Images reconstructed with these techniques exhibit spatially-varying noise statistics, which limit the applicability of conventional de-noising techniques.

Several de-noising methods have been proposed to enhance the SNR of images acquired using parallel MRI techniques. One method, anisotropic diffusion filtering (ADF) [126], effectively improves SNR while preserving edges by averaging the pixels in the direction orthogonal to the local image signal gradient. ADF can potentially remove small features and alter the image statistics, although adaptively accounting for MRI's spatially-varying noise characteristics can offer improvements, this is challenged in practice by the lack of availability of the image noise matrix [127]. Wavelet-based filters have also been applied to MRI [128-131]. These are prone to produce edge and blurring artifacts [132].

Recently, de-noising methods employing non-local means (NLM) [133] were applied to increase the MRI SNR by reducing variations among pixels in the image with close similarity indices [134]. The robustness of the determination of pixel similarity is enhanced by comparing small image regions centered at each pixel, rather than by pixel-by-pixel comparisons. While adaptive NLM de-noising (involving the estimation and incorporation of spatial variations in the noise power) offers improved performance [135], NLM can still affect image statistics [136] and its computational burden is significantly high compared to other approaches.

In this chapter we introduce a new, time efficient, image de-noising method by applying spectral subtraction directly to MRI acquisitions in k-space. Spectral subtraction is well-established for the suppression of additive Gaussian noise (AGN) [137] and is commonly used in speech processing [138]. It has been applied to the time-course of functional MRI (fMRI) data to facilitate event detection [139], but not the SNR enhancement of routine MRIs *per se*. We test spectral subtraction de-noising (SSD) on both numerical simulations, as well as experimental MRI data including parallel SENSE image reconstruction [68], and compare its performance with ADF.

## 3.2. Theory

For Cartesian MRI, the acquired complex signal fills k-space matrix. Each k-space row can be modeled as an underlying true signal plus Gaussian noise:

$$x_r(t) + ix_i(t) = s_r(t) + n_r(t) + i\left[s_i(t) + n_i(t)\right] \quad \textbf{[3.1]}$$

where $x(t)$ is the observed k-space signal, $s(t)$ is the true underlying noiseless k-space signal, $n(t)$ is the AGN, and subscripts $r$ and $i$ denote real and imaginary components, respectively. For convenience, equations for de-noising the real part of any k-space line should be interpreted hereinafter as applying also to the imaginary part. Assuming that signal and noise are uncorrelated (which is the case in MRI), the power spectral density (PSD) obtained from a one-dimensional Fourier Transform (FT) of a k-space line is given by:

$$\left|X_r(f)\right|^2 = \left|S_r(f)\right|^2 + \left|N_r(f)\right|^2 \quad \textbf{[3.2]}$$

where $\left|S_r(f)\right|^2$ is the PSD of the noiseless signal and $\left|N_r(f)\right|^2$ is the PSD of the noise and $f$ is the conjugate variable of $t$. Because the PSD of the AGN is constant, we can subtract the root-mean-square (RMS) noise power, $\left|\overline{N(f)}\right|^2$, from the PSD of the acquired signal to get an estimate of $\left|S_r(f)\right|^2$. This reduces the noise bias on the acquired signal, which becomes:

$$\left|Y_r(f)\right|^2 = \left|X_r(f)\right|^2 - W(f)\left|\overline{N(f)}\right|^2 \quad \textbf{[3.3]}$$

where $W(f)$ is a pre-defined weighting function of $f$ with real values in the interval [0, 1], and $Y_r(f)$ is the $f$-spectrum of the de-noised signal and estimator of $S_r(f)$. Because the PSD cannot be negative, subtractions that result in negative values are replaced by the original PSD at the corresponding $f$-frequency, according to:

$$|Y_r(f)|^2 = a|X_r(f)|^2 \quad \textbf{[3.4]}$$

where $a$ is a real, single-valued regulation parameter in the interval [0, 1] [137]. The de-noised signal, $Y_r(f)$, is computed from the square root of its PSD, with the phase information retrieved from the *f*-spectrum, $X_r(f)$, of the acquired signal:

$$Y_r(f) = |Y_r(f)|e^{iPhase(X_r(f))} \quad \textbf{[3.5]}$$

Phase information is kept the same as in the original *f*-spectrum. Taking the inverse FT of $Y_r(f)$ yields the real part of the de-noised k-space line. To reduce directional filtering effects the same algorithm is applied on the columns of the k-space and the average of both de-noised images are taken.

After applying the same algorithm to the real and imaginary parts of all the k-space lines, a de-noised k-space set, $y_r(t) + i \cdot y_i(t)$, is produced, from which a conventional 2D FT image reconstruction yields the de-noised MRI.

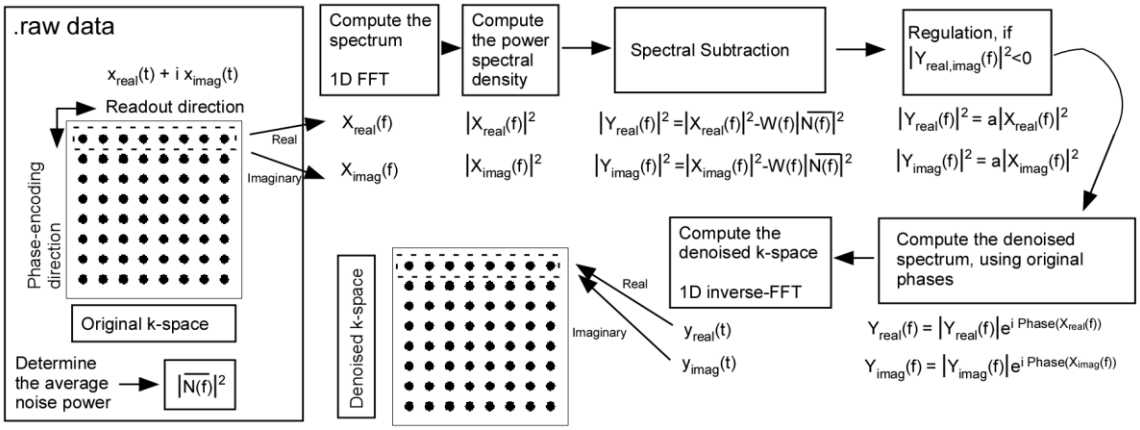


**Figure 3.1.** Flowchart of the spectral subtraction algorithm along the row direction of k-space.

## 3.3. Methods

### 3.3.1. SSD and ADF Application

The algorithm for performing SSD of MRI uses Matlab (Mathworks, Inc., Natick, MA) software on a laptop computer with 2GHz processor and 8GB of memory. The algorithm is separately applied to each k-space row and column, as depicted in Figure 3.1, and the two de-noised k-space results averaged. The regulation parameter, $a$, was set to 0.2 and the windowing function $W(f)$ set to 1 for all frequencies to avoid introducing any extra spatial filtering effects.

ADF is chosen for comparison as it was previously used for de-noising MRI, and shown to overcome the problem of blurring of object boundaries while providing a time-efficient implementation [126, 140]. The Matlab script, 'anisodiff2D' (available from Matlab Central File Exchange [141]) is applied on magnitude images scaled to a range of [0,1] (input parameters: 15 iterations; integration constant: 1/7; gradient modulus= 0.02).

### 3.3.2. Computer Simulations

Numerical simulations are performed using a 1024x1024 pixel Shepp-Logan phantom and a reference 256x256 pixel high-SNR brain MRI which was considered noise-free [142]. Gaussian noise of the same amplitude is added to the real and imaginary parts of the 2D FT (k-space) of the images. SSD is applied to the complex k-space data, while the ADF is applied to the magnitude image.

Numerical simulations for SENSE [68] images are based on the 256x256 high-SNR brain image. Eight complex coil sensitivity maps corresponding to the sensitivity profiles of an 8-channel head coil are simulated [143], and the individual coil data generated by multiplying the simulated sensitivity profiles with the original image. Gaussian noise is then added to the real and imaginary parts of the 2D FT of each of the 8 images. Simulated noisy k-space data generated by 2D FFT of the individual coil images are sub-sampled with a reduction factor, R. The SSD method is separately applied to the complex k-space data from the 8 coils. Sub-sampled and unprocessed k-space data and spectral subtraction method applied k-space data are then fed into a SENSE reconstruction employing the simulated coil profiles. For comparison, the ADF is applied to the SENSE magnitude image generated from unprocessed k-space data. The brain image, simulated sensitivity profiles, and SENSE reconstruction code is publicly available and was downloaded from Ref. [142].

The average noise power $\left|\overline{N(f)}\right|^2$ used for de-noising the simulated images is determined by scaling the variance of the added noise, with the dimension, $X$, of the 1D FT (to account for the FT scaling):

$$\left|\overline{N(f)}\right|^2 = \sigma_N^2 \cdot X \qquad \textbf{[3.6]}$$

where, $\sigma_N^2$ is the average noise power added to k-space to corrupt the image.

Computer simulations are iterated 100 times for each input SNR level and reduction factor. Pixel-wise SNR values are extracted from the signal mean and standard

deviation (SD) using:

$$SNR(x,y) = \frac{mean\left[I_i(x,y)\right]_i}{SD\left[I_i(x,y)\right]_i} \quad \textbf{[3.7]}$$

where $I_i(x,y)$ is the magnitude of the pixel at location $(x,y)$ in the image at the $i^{th}$ iteration. The root-mean-squared error (RMSE), and structural similarity indices (SSIM) [144] of noisy and de-noised images are quantified by comparing them to the original noiseless image. The SSIM is computed using:

$$SSIM(x,y) = \frac{4\mu_x\mu_y\sigma_{xy}}{(\mu_x^2+\mu_y^2)(\sigma_x^2+\sigma_y^2)} \quad \textbf{[3.8]}$$

where $x$ and $y$ are the images that are compared, $\mu$ is the mean of the pixel intensities. $\sigma_{xy}$ is the cross-correlation between the two images and $\sigma_x$ is the standard deviation of pixel intensities in image $x$.

The reported SNR and RMSE for images reconstructed in computer simulations, are pixel-wise averages over each entire image, excluding the background.

### 3.3.3. MRI Experiments

Imaging experiments are performed on a mineral oil phantom, and on healthy volunteers in studies approved by our Institutional Review Board (IRB). Experiments are conducted on a 3T Philips Achieva scanner (Philips Medical Systems, Cleveland, OH), and the raw data is exported for processing. $T_1$-weighted multi-slice (24 slices) fast field echo (FFE) sequences with flip angle =80° are used for both phantom and brain studies. Single coil phantom images are acquired with the Philips body coil. The FFE sequence is used in

phantom experiments with a repetition period TR=30ms, and echo time TE=4.6 ms.

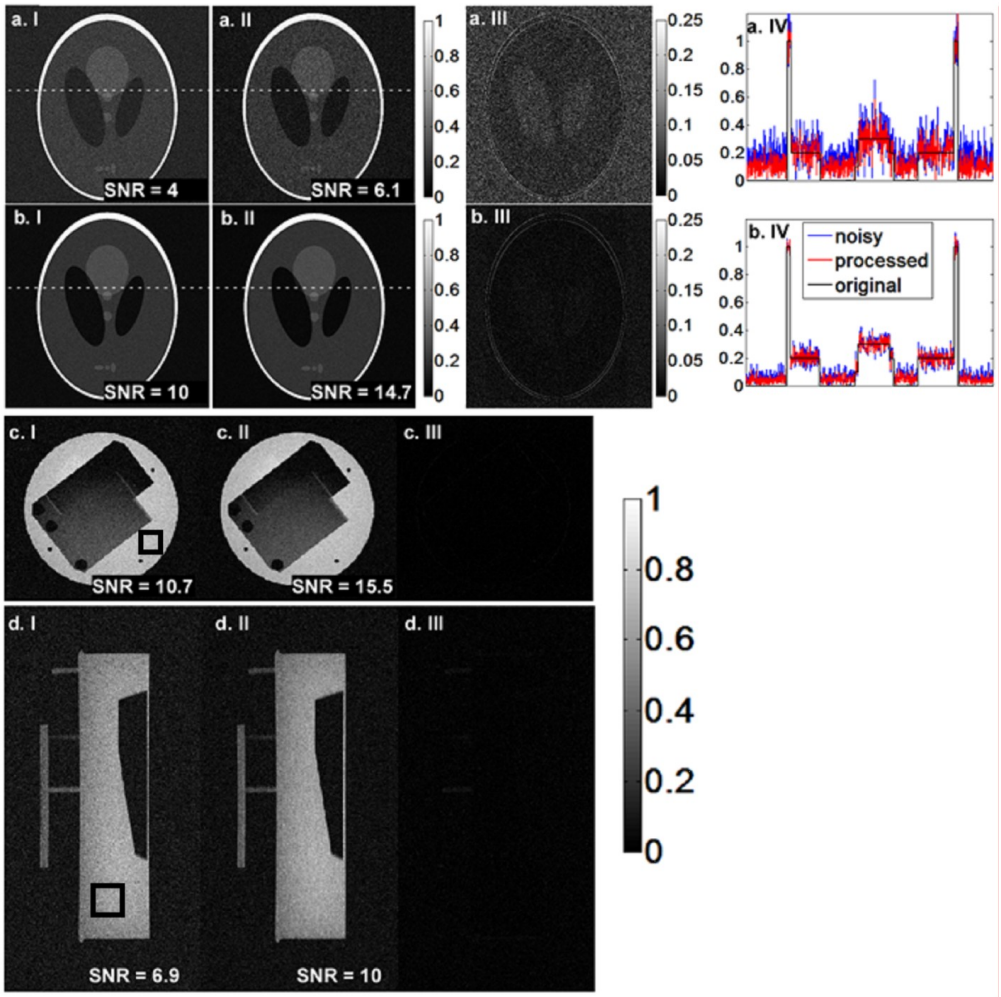


**Figure 3.2.** Simulated Shepp-Logan phantom (rows a-b) and MRI phantom magnitude images (rows c-d) are shown. Original noisy images (column I), processed images (column II) and the residuals (column III) are displayed. Profile of the image along the dotted lines in Fig. a-b.I-II are plotted in Fig. a-b.IV respectively. SNR improvement of ~40% is observed. Noise level is calculated from the background and signal intensity is calculated by averaging the pixels in a uniform region as indicated by the square box.

Parallel MRI data from the brain is acquired using a Philips 8-channel 3T head coil with TR/TE = 385/9.2 ms and a 576x575 matrix size (with no reduction factor). A 6-channel Philips cardiac coil is used for cardiac cine MRI, which is performed with two SNRs realized by varying the bandwidth per pixel from 1.63 to 0.86 kHz. The change in

bandwidth affects the sequence timing slightly: we use single breath-hold, ECG-triggered 2D turbo field echo sequences (turbo factor, 8; TR/TE = 2.7/1.35, 3.2/1.53ms; cardiac phases: 30, 25; matrix size: 256x256) for cardiac studies.

The average noise power in the MRI experiments is accurately determined from data acquired during the preparation phase of the scanner with both RF power and gradients turned off. The receiver bandwidth and gain is identical for each set of experiments. Samples for each coil element are stored (as ".raw" files) and exported from the scanner. This does not affect exam time because the information is already acquired by the scanner, but the noise could also be estimated from the image data by other statistical and/or spectral analyses [145, 146]. We observed that the noise power of the highest noise-contributing coil element was 90% higher than the coil element with the lowest noise contribution. The MRI signal from each coil element is de-noised separately using their corresponding additive noise level estimates determined from the ".raw" data. $\left|\overline{N(f)}\right|^2$ is calculated using Eq. [3.6], where $\sigma_N^2$ is the variance of the acquired noise samples.

The sensitivity profile for the SENSE reconstruction is separately estimated for each coil by polynomial fitting of the complete acquired dataset [147]. The effect of de-noising on parallel imaging was tested with SENSE reconstruction reduction factors of R=1.5-3. The SNR reported for brain images was taken as the average of pixel-wise SNR values computed using given by Eq. [3.7], including all the image pixels and CSF, except the background.

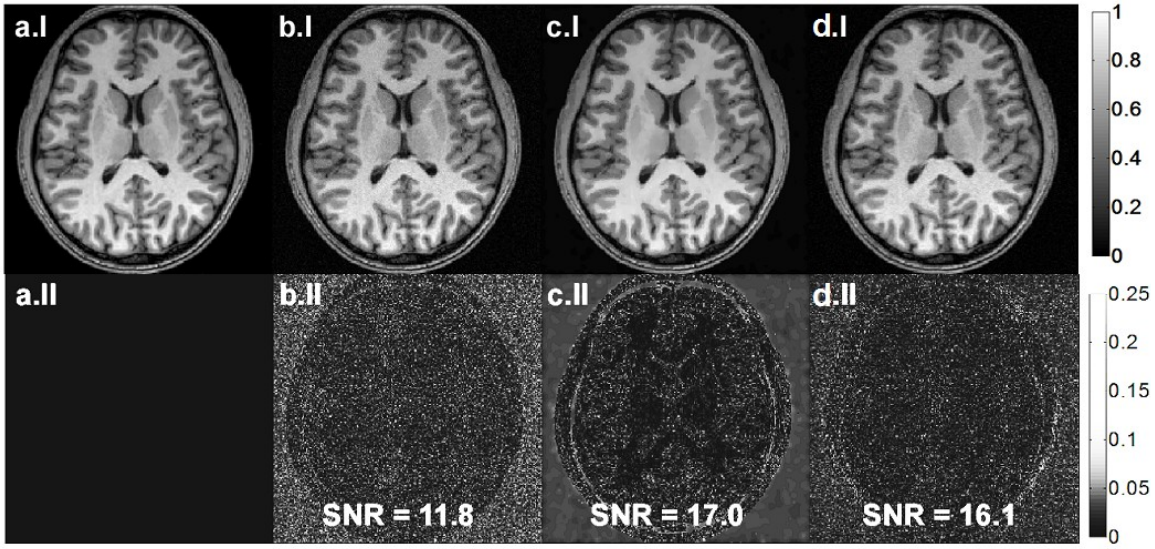


**Figure 3.3.** (a.I) Original noiseless image, (b.I) noise added image with SNR = 11.8, (c.I) ADF and (d.I) SSD method applied images are shown on top row. Residual images with respect to (a.I) are displayed on row II.

## 3.4. Results

### 3.4.1. Single-channel De-noising

Simulation results of the Shepp-Logan phantom with different SNR values are shown in Figure 3.2 (a, b). The magnitude images reconstructed from the original, and the de-noised k-space data are shown in columns I and II respectively. Column III shows the absolute difference between the images of columns I and II (residual), while column IV plots the noiseless, noisy, and SSD signal across a horizontal line through the phantom. SSD provides an SNR improvement vs. the noisy image of 50% without any artifacts apparent.

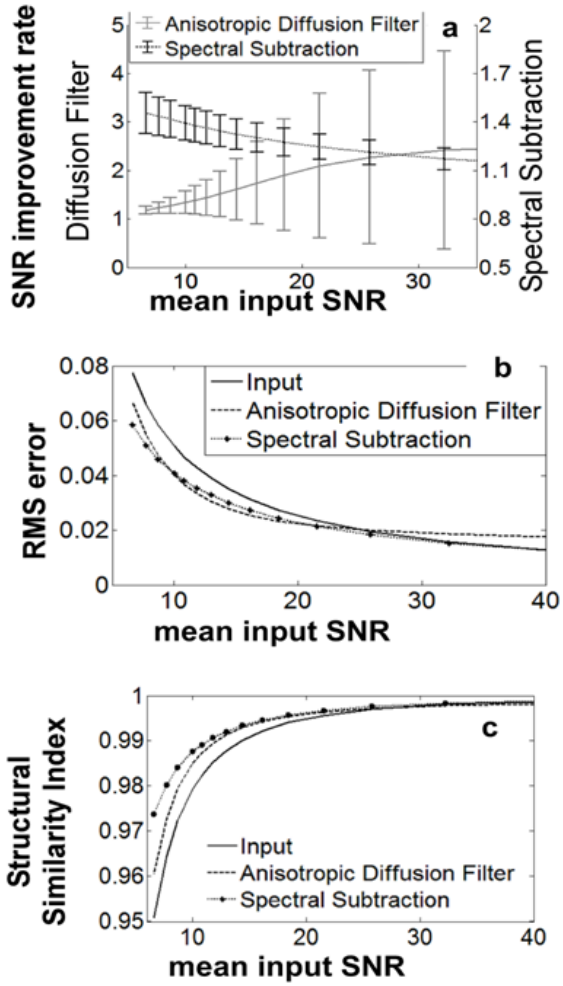


**Figure 3.4.** (a) SNR improvement, (b) RMSE and (c) structural similarity index are plotted against input image SNR for computer simulation results where; dotted curves are anisotropic diffusion filter results while dashed ones represent the spectral subtraction method.

Experimental MRI results from a phantom imaged with the body coil and using the background to calculate noise power, are shown in Figure 3.2.c, d. Column I shows the original images, column II are the processed images, and column III are the residuals. Here, SSD results in a mean pixel SNR improvement of 45%.

A high-SNR brain image polluted with AGN, and then filtered with ADF or SSD, are displayed in Figure 3.3, row I. The differences between the processed and the

original image (Figure 3.3.aI) are shown in row II. Both de-noising methods effectively increase SNR by about 40% without removing high spatial-frequency information, as evidenced by the artifact-free residual images.

The results from filtering and de-noising as a function of noise level, are plotted in Figure 3.4. As suggested by the slightly higher SNR for ADF in Figure 3.4c, ADF can provide a greater SNR gain at high SNR. However, the ADF and SSD gains are comparable at low SNR (Figure 3.4a), and SSD has a much more homogeneous SNR improvement in the presence of varying signal SNR, than ADF (Figure 3.4a). This means that it is much better at preserving the original contrast between signals that vary in intensity, spatially, especially at higher SNR values. The SNR gain for SSD approaches unity as the SNR of the acquisition improves and the noise has a diminishing affect on the signal. This is not the case for ADF. The accuracy or RMSE of the two approaches, as compared to the original image, is plotted in Figure 3.4b. Both methods show a comparable improvement in accuracy at low SNR compared to the noise image. However at higher SNR (>25), the accuracy of ADF is inferior to not using any filter, while the performance of the SSD method tracks the accuracy of the input image. Figure 3.4.c shows the structural similarity index (SSIM) [144]. This illustrates that the SSD method is superior to ADF in preserving the structural information of the image.

## 3.4.2. SENSE Reconstruction De-noising

Figure 3.5 depicts a reconstructed 8-channel SENSE image with a reduction factor (R) of 1.5 and an unfiltered mean image SNR of 16.3, zoomed-in to reveal fine

detail without filtering (Figure 3.5a), with ADF, (Figure 3.5b) and with SSD (Figure 3.5c) applied. Figure 3.5d is the pixel-wise SNR improvement map provided by the ADF method. For ADF, the spatial performance is inhomogeneous, with a salt-and-pepper type noise pattern that is also evident in Figure 3.5b. Conversely, because the SSD method operates in the frequency domain of the acquired data, its pixel-wise SNR improvement map in Figure 3.5e, is uniform throughout the signal-bearing regions of the image, demonstrating that the acquisition statistics are preserved. This is further evidenced by histograms of the pixel intensities of the two SNR improvement maps (from Figs 5d and e) in Figure 3.5f, which are sharply clustered for SSD, but not ADF. RMSE, SSIM and SNR improvement, are plotted as a function of reduction factor and input SNR in Figure 3.6 for both filtering methods. The SSD method's performance is comparable to ADF up to a reduction factor of ~2, and better than ADF at higher reduction factors. The SNR improvement for SSD is inversely related to the input SNR.

SENSE reconstructed, ADF, and SSD-processed images from acquired parallel imaging data with reduction factor of 2 are shown in row I of Figure 3.7, with their corresponding zoomed-in views in row II. The ADF performance is spatially heterogeneous, with best results in high SNR regions and pixilation effects in the middle of the image with low SNR. On the other hand, the SSD method is unaffected by local noise variations and acts homogeneously on the image. Figure 3.7cII shows better delineation of the superior sagittal sinus compared to the original and ADF applied images.

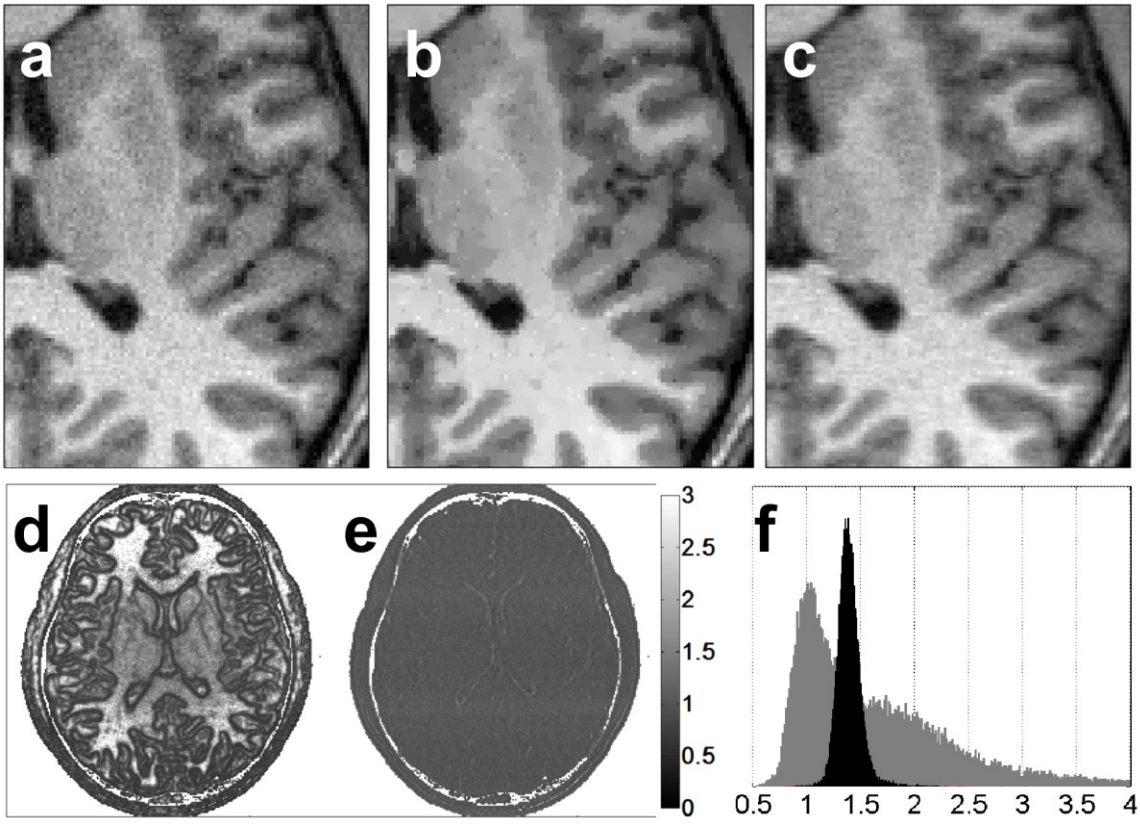


**Figure 3.5.** (a) SENSE reconstruction from noise added data with reduction factor of 1.5 and SNR of each coil image equal to 12, (b) anisotropic diffusion filtered image, and (c) spectral subtraction method applied image are zoomed in. (d) Pixel-wise SNR improvement rate of anisotropic diffusion filter, and (e) spectral subtraction method are displayed along with their histograms (f, gray: anisotropic diffusion filter, black: spectral subtraction method). Background of the image is not used in SNR calculations. Despite the higher SNR improvement of ADF, pixilation effects are visible in the image.

SENSE cardiac images reconstructed with R=1.5 and two different acquisition bandwidths are shown in Figure 3.8a,c. Five cardiac phases are depicted, four of which are zoomed in. To assess the SNR improvement realized by SSD in the septum, the mean signal intensity is divided by the noise level in the square volumes marked in Figure 3.8. The apparent SNR in the septum is 3.06±0.4 and 8.25±1.0 for the unfiltered images

acquired with 1.63 and 0.86 kHz bandwidth per pixel respectively (Figure 3.8a,c). SSD provides average SNR improvements of 40±3 and 42±3% calculated and averaged over the 30 and 25 cardiac phases of each scan respectively (Figure 3.8b,d), consistent with the numerical results. No significant blurring effects are noticed in comparing the filtered and unfiltered cardiac cine images acquired at the two different SNR levels (Figure 3.8).

SSD using Matlab took 0.4s for a 512x512 image, compared to 1.3 seconds for ADF on the 2GHz computer.

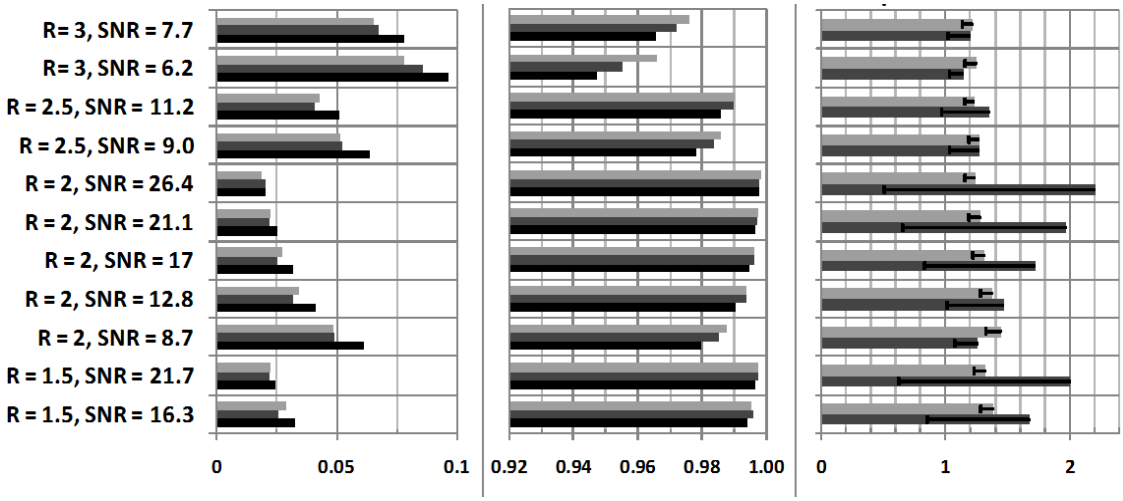


**Figure 3.6.** (a) RMSE, (b) SSIM and (c) SNR improvement rates on SENSE images with different reduction factors and input SNRs (light gray: SSD, dark gray: ADF, black: original reconstruction). It is noted that the SSD outperforms both the original SENSE reconstruction and ADF in terms of the SSIM.

## 3.5. Discussion

Spectral subtraction methods are commonly used in automated speech recognition [138] to improve the estimation efficiency, and in many other applications

including the temporal de-noising of functional MRI data streams for event detection [139]. However, at least to our knowledge, they have not been used in standard MRI for the spatial de-noising of individual images. SSD methods work on data corrupted by additive Gaussian noise that is uncorrelated with the underlying data and has a constant power spectrum. Noise in the complex data acquired from each coil element in an NMR experiment generally satisfies these assumptions, but is not immune from non-Gaussian events such as physiologic motion or noise spikes, for example. The computational load for de-noising an NxN image using SSD is of the order $O\left(N^2 \log(N)\right)$ [137], much less than that of de-noising by non-local means, $O\left(N^4\right)$ [148].

The SSD method can be likened to a Wiener filter. An optimum Wiener filter modifies each component in the power spectrum of the input according to the noise power at the corresponding frequency, which may not be constant throughout the spectrum. However, the SSD method de-noises the data using the mean of the power spectrum to provide an unbiased estimate of the signal and a variance depending on the signal and noise characteristics [137, 139]. SSD does not account for the variations in the phase caused by the additive noise. The phase of the complex Gaussian noise is uniformly distributed in the interval [-π, π] which cannot be estimated statistically in either the image or its transformed domains. However, the power spectrum of finite samples of complex Gaussian noise is scattered at a constant level, enabling its estimation and subtraction from the power spectrum of the complex received signal.

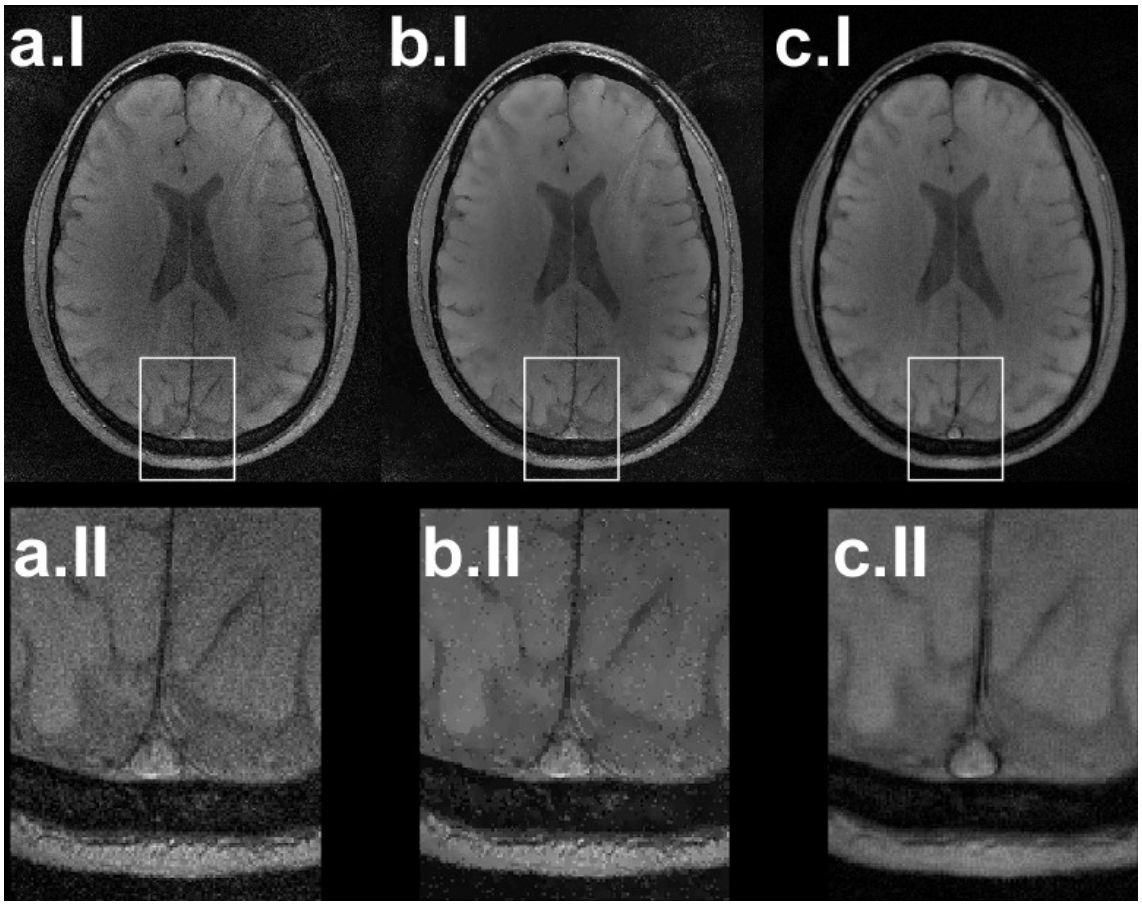


**Figure 3.7.** (a.I) Brain MR image of a healthy volunteer reconstructed from an 8-channel coil using SENSE reconstruction with a reduction factor of 2, (b.I) de-noised image using ADF, and (c.I) SSD. (row II) The superior sagittal sinus surrounded by white boxes in images in row I are zoomed in to show the image quality improvement.

The response of the SSD filter depends on the input signal. It is an SNR-dependent filter wherein lower-SNR components are attenuated more than higher-SNR components, which may introduce subtle image blurring for low-level signals. Any de-noising method applied to parallel MRI data, is challenged by the spatially varying noise statistics that result from the coils' sensitivity profiles and reconstruction algorithm. The SSD method is immune to such effects when the data acquired from each coil element is

separately de-noised using its measured average noise power spectrum, which can vary significantly between elements. The present results also suggest that SSD can be applied in situations where there is inherent physiological noise and motion such as in the heart (Figure 3.8).

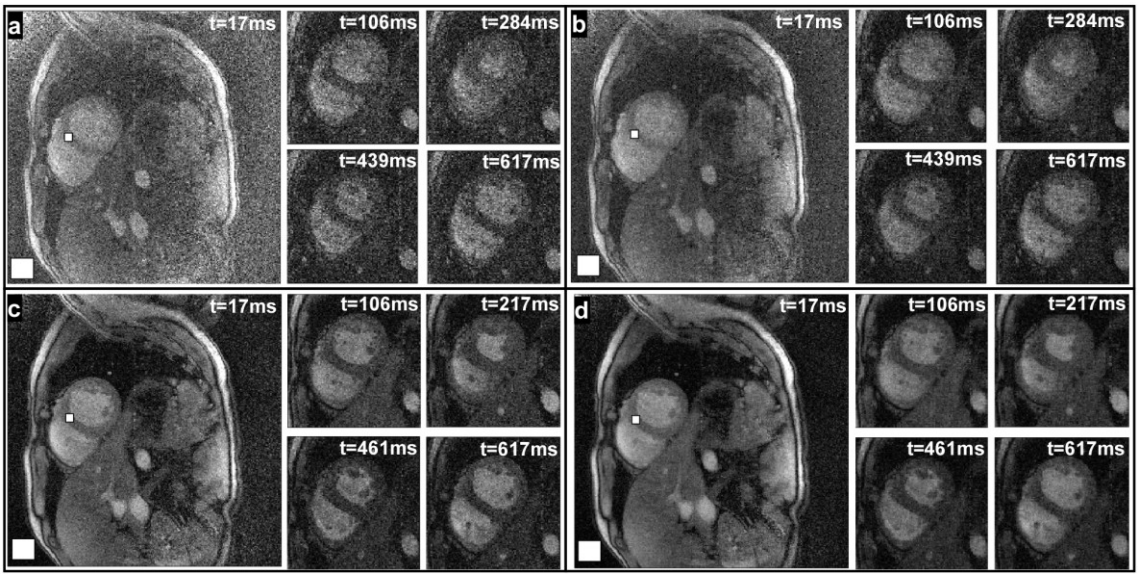


**Figure 3.8.** Displayed in panels (a, c) are SENSE (R=1.5) reconstructed short-axis cardiac images acquired at different cardiac phases, and the corresponding SSD images are shown in panels (b, d). SNR calculations from septum and background (white boxes) show an average improvement of 40±3% and 42±3% (b and d respectively).

In conclusion we have shown SNR improvements of up to 45% for MRI using SSD in both single and array coils reconstruction while preserving image details, in simulations and in practice in phantoms and multi-channel brain and cardiac MRI. The SSD method performs comparably to ADF in terms of SNR improvement, and superior to ADF with respect to accuracy and the retention of structural detail, at a reduced computational load.

# Chapter 4.

# The Interventional Loopless Antenna at 7 Tesla

## 4.1. Introduction

Interventional MRI combines the multi-functionality and inherently high soft-tissue contrast of MRI, for targeting therapy and monitoring response without using ionizing radiation. The increasing availability of ultra high-field (UHF) whole-body MRI systems ($B_0$>3T) that promise higher SNR [149, 150], raises the question of whether interventional UHF MRI is advantageous, feasible, or even safe in these systems. Indeed, because the wavelength of the transverse radio frequency (RF) field is comparable to the body size, the problems of sample resonances, inhomogeneous excitation fields [103], highly localized specific absorption rates (SAR) and heating [59, 151, 152], are exacerbated when interventional devices are introduced. At 7T, the feasibility and safety of prostate imaging with receive-only [116] and transmit/receive endo-rectal loop coils modified from commercial 3T endo-rectal coils was only recently demonstrated *in vivo* in humans [116, 153, 154], and the relative SNR advantages compared to lower-field devices remain to be seen. Even so, with a 3.5 cm diameter these internal coils are not suitable for intravascular or interstitial use.

The “loopless antenna” MRI detector can be fabricated with sub-millimeter diameters, and therefore is suitable for intravascular use as a guidewire, catheter [120], or for incorporation into a biopsy or therapy-delivery needle [155]. It consists of a thin coaxial

cable with an inner conductor extended to form a resonant whip at the MRI frequency. It has a high sensitivity in the near-field, which may be improved by modifying the insulation [121, 122], and which decreases with the inverse of radial distance (ρ) from the device [8]. In the past, loopless antenna detectors working at $B_0 \leq 1.5T$ have been used in angioplasty procedures [156-158], for atherosclerotic plaque characterization [159] and for tumor detection [160]. Because the signal strength increases with $B_0^2$ while the noise for miniaturized coils is dominated by the direct electric (E-)field which for the loopless antenna does not vary significantly with $B_0$, the SNR of the loopless antenna increases approximately as $B_0^2$ [161]. This has been experimentally verified up to $B_0=4.7T$ [161]. If this SNR response were sustained up to $B_0=7T$, an SNR advantage of approximately 5.4-fold would accrue relative to 3T. Moreover, compared to the prior 1.5T work, a 7T SNR advantage of over 20-fold would be anticipated.

Here, the feasibility of performing MRI with the interventional loopless antenna detector at UHF is investigated at 7T and compared with the performance at 3T. Its theoretical SNR is determined by numerical electromagnetic (EM) method-of-moments (MoM) analysis at 7T and at 3T, and by direct experimental measurements on devices fabricated with the same geometry in an electrically bio-analogous phantom. Safety at 7T is investigated with numerical three-dimensional (3D) full-wave EM computations of the local specific absorption rate (SAR), and by direct temperature measurements in an RF shielded room with the transmit volume MRI coil driven from a directly monitored source. Finally, we present high-resolution (40-80μm) 7T and 3T images of human

carotid artery specimens loaded in a saline phantom, for SNR comparison. At these voxel sizes, the spatial resolution is about 10-fold higher than previous 3T intravascular MRI [161-163].

## 4.2. Methods

### 4.2.1. Theoretical SNR computation

Numerical EM analysis of SNR and SAR were performed using a 3D full-wave EM MoM simulator (FEKO EM analysis software, Stellenbosch, South Africa) similar to previous studies[55, 164]. The loopless antenna was modeled as a quarter wave-length ($\lambda_c/4$; 17cm at 7T, 40cm at 3T) coaxial cable terminating with its inner conductor extended to form a 33mm (7T) or 39mm (3T) resonant whip. The antenna was excited by a unit amplitude current source applied to the whip-cable junction at a frequency of 298MHz (7T) or 128MHz (3T). Conducting surfaces were modeled as perfect electric conductor (PEC). Saline was modeled as an infinite medium with conductivity σ=0.6S/m and dielectric constant ε=80, which are comparable to human muscle at 298 and 128 MHz. The RF magnetic field distribution was computed at 0.2mm intervals up to 10cm from the whip-cable junction in the axial plane, and 20cm along the long axis extending 8cm distally from the junction. The absolute SNR in $ml^{-1}Hz^{1/2}$, $\Psi_s$, under fully relaxed conditions was determined from:

$$\psi_s = \frac{\omega M_0 \left| B^+ \right|}{\sqrt{2KTR_{load}}} \quad \textbf{[4.1]}$$

where $M_0$=3.2692x10$^{-9}$ $B_0JT^{-1}ml^{-1}$ is the equilibrium nuclear magnetization per unit volume for water at 22°C, $|B^+|$ is the magnitude of circularly polarized transverse magnetic field generated by the unit current applied to the antenna, *K* is Boltzmann's constant, T is the temperature at the whip in Kelvin. With the antenna aligned parallel to $B_0$, $\left|B^+\right| = B_\theta / \sqrt{2}$ where $B_\theta$ is the cylindrical polar RF field component. $R_{load}$, is the computed load resistance at the junction. At 7T, a cable loss of 0.32dB/m for the experimental UT-85C cable was added.

## 4.2.2. SAR analysis

The SAR distribution in a 20-cm long by 20-cm diameter cylindrical head-sized phantom filled with homogenous saline (σ=0.63 S/m, ε=80), was determined from the induced electric fields with the sample at iso-center of a quadrature cylindrical 7T head transmit coil of the same geometry as a Nova Medical, Inc, (Wilmington, MA) head coil. The coil was modeled with twelve 25 cm-long equally spaced struts connected to two circular 29cm-diameter PEC end rings, and excited by unit current applied with 30° phase shifts to each adjacent strut to create the rotating field at the 7T MRI frequency. A reference SAR simulation was performed at 7T with the antenna removed to determine the locations of maximum SAR exposure (Figure 4.1.a-b) for subsequent antenna placement. Accordingly the antenna was positioned with long axis 3 cm above

and parallel to the phantom's cylindrical axis and the z-axis of the scanner (Geometry 1; Figure 4.1), at insertion depths of 35 and 100 mm. A second trans-axial configuration with the lead intersecting two high SAR regions was also investigated (Geometry 2; Figure 4.1). In Geometry 2, the lead was parallel to the x-axis, 3cm off-center, at an insertion depth 100mm. The phantom in this case was 2cm off iso-center to accommodate the proximal end of the device. For the SAR calculations, the loopless antenna was modeled the same as for the SNR computations, but with the current source removed from the junction and with the proximal end of the coaxial cable electrically shorted to simulate the effect of decoupling circuitry.

For the numerical analysis, the triangular mesh size was 0.5mm in a 6-cm rectangular prism centered on the antenna. This was gradually coarsened away from the antenna to a maximum of 12mm near the edge of the phantom to conserve computation time. All mesh lengths were shorter than the maximum of λ/12 suggested by FEKO. Reference SAR simulations were performed at 7T and 3T with the antenna absent, using identical grid locations and the same power applied to the coil. The 3D volume E-field data was imported to MatLab and the SAR distribution at each point (x,y,z) calculated as:

$$SAR(x,y,z) = \frac{\sigma(E^2_{X(x,y,z)} + E^2_{Y(x,y,z)} + E^2_{Z(x,y,z)})}{2\rho} \quad \textbf{[4.2]}$$

where $\rho$ (in kg/m$^3$) is the density of the saline, and $E_X$, $E_Y$, and $E_Z$ (in V/m), are the electric field components at (x,y,z). The sampling resolution or point size corresponds to

$1.25x10^{-4}$g of saline. The 1g average SAR distribution was obtained by averaging all pixels within a $1x1x1cm^3$ cube centered at (x,y,z). The result was divided pixel-by-pixel with the reference simulation to obtain an SAR amplification factor. This was multiplied by 4 to provide a local SAR map at an applied SAR exposure of 4 W/kg.

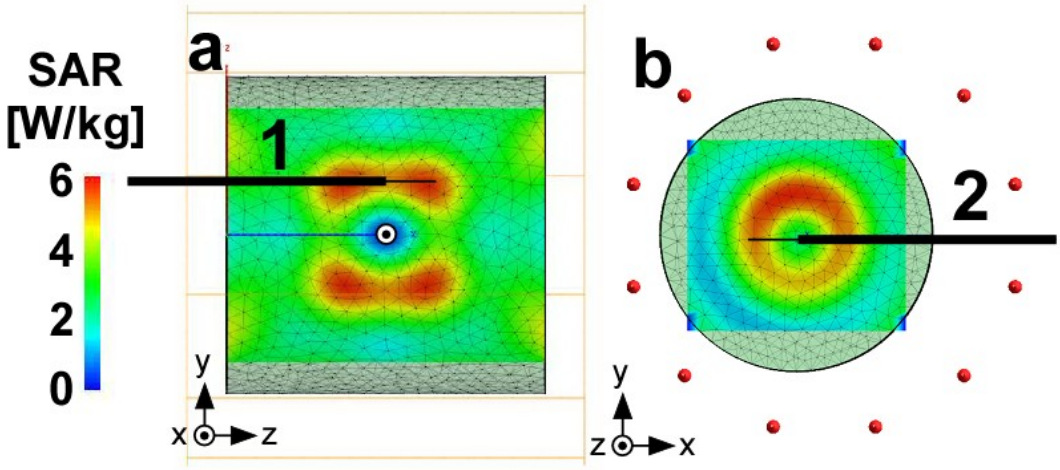


**Figure 4.1.** (a) SAR distribution in a saline cylindrical phantom in sagittal (x=0cm), and (b) axial (z=3cm) plane with the horizontal solid line showing the placement of the device for safety testing in Geometries 1 and 2 respectively. The origin is the iso-center of the phantom.

## 4.2.3. Experimental Devices

Experimental 3T and 7T loopless antennae were fabricated from UT-85C semi-rigid coaxial cable (Micro-coax, Inc., Pottstown, PA) with a resonant whip length and $\lambda_c/4$ cable optimized in saline with a spectrum analyzer[161]. At 7T, the cable length was 17cm and the whip length was 32mm, in agreement with the simulations. The end of the $\lambda_c/4$ cable was connected to a solenoidal balun to block common-mode signals[165], and an interface box for decoupling and matching. The decoupling circuit (Figure 2.6)

employs a diode shorted during RF transmission by a decoupling bias applied by the scanner to isolate the antenna from the receiver chain. During signal reception the bias is turned-off, and the MRI signal from the whip is conducted to the MRI scanner via an additional bazooka balun and λ/4 cable to further minimize currents on the outer conductor (Figure 4.2.b). Antennae were matched to 50Ω in saline. The combined measured isolation of the common mode achieved by the baluns was 37dB at 7T and 43dB at 3T.

## 4.2.4. Experimental SNR

A 20cm long by 20cm external diameter cylindrical saline phantom (wall thickness, 3.2mm) was prepared for SNR measurements using 3.35g/l salt and 0.5g/l $CuS0_4$ to achieve the requisite electrical properties comparable to biological tissue (σ =0.63 S/m; ε =80) [166]. The $CuS0_4$ reduced the spin-lattice relaxation time to ~0.5s at both field strengths. 7T SNR measurements were done on a Philips Achieva 7T MRI scanner (Philips Medical Systems, Cleveland, OH), using the Nova Medical head coil for RF transmission and with the antenna connected to one of the 32 receiver channels and the other 31 channels terminated with 50Ω. The device was inserted in the saline phantom oriented parallel to the main magnetic field, and axial MRI performed at the antenna junction using a fully-relaxed gradient-echo sequence (echo-time, TE=11.5ms; repetition period, TR=2s; bandwidth, BW=125.4kHz; excitations per frame, NEX=1; field-of-view, FOV=20cm; slice thickness=3mm; acquisition matrix $N_x$x$N_y$=1000x1000; scan duration=33.3min). A “Spredrex” RF sinc-pulse with a high time-bandwidth product

truncated after the main lobe was used to reduce errors in the calculated $B_1$ map [167], and the scan repeated with different excitation flip angles ($\alpha$) to permit correction for RF field inhomogeneity. The 3T antenna was tested in the same saline phantom and orientation as at 7T, in a Philips 3T XMR Achieva system. The same location at the antenna junction was scanned with an equivalent gradient-echo sequence using the Philips 3T body coil for transmission.

The fully-relaxed gradient-echo signal from a pixel at location (x,y) in the plane of the junction was given by:

$$F_{(x,y)} = S_{(x,y)} \sin[\alpha R_{B(x,y)}] \quad \textbf{[4.3]}$$

where $S_{(x,y)}$ is the sensitivity of the antenna at (x,y), $R_{B\ (x,y)}$ is ratio of the RF field distribution at (x,y) to the nominal RF field applied by the scanner ($B_1$) and $\alpha$ is the applied flip angle. The root-mean-square noise was measured from images acquired at 7T and 3T with the RF transmitter and MRI gradients turned-off. $S_{(x,y)}$ and $R_{B\ (x,y)}$ were determined at every pixel from the images acquired with different flip-angles using a least-squares fit. The absolute measured SNR in $ml^{-1}Hz^{1/2}$ was computed using [161]:

$$\Psi_{ms(x,y)} = \frac{S_{(x,y)}\sqrt{BW}}{V_{pixel}\sqrt{N_x N_y}} 10^{NF/20} \quad \textbf{[4.4]}$$

where $V_{pixel}$ is the pixel volume in ml and $NF$ is the noise figure of the RF receiver chain measured by the cold 50Ω resistor method [168] in both systems (0.97dB @7T, 0.94dB @3T).

## 4.2.5. RF safety testing

The RF power provided by the 7T scanner failed to produce a sufficient temperature increase under either control or antenna-loaded conditions to enable reliable documentation of device safety. Therefore heat testing was performed inside an RF shielded room with the 7T Nova Medical quadrature transmit head coil driven by a continuous wave (CW) RF power amplifier (Tomco Inc, BT00250, Stepney SA, Australia) connected to a 298MHz frequency synthesizer. The experimental setup is shown in Figure 4.3. The RF power was continuously monitored during experiments with a commercial RF power meter (LadyBug Technologies, Santa Rosa, CA). This bench setup allowed heat testing at higher RF power levels than provided by the scanner, and better experimental control and monitoring of input power, without occupying valuable scanner time for a non-imaging study.


**Figure 4.2.** (a) Pictures of the 7T loopless antenna, and (b) the quarter-wave length cable with balun.

Heat testing was performed on the 20cm cylindrical phantom filled with saline possessing similar electrical properties as in the SAR computations, but with gel added

to limit convection (15g/l polyacrylic acid, 0.8g/l salt), forming a "slush". Device heating in the same configurations (Geometries 1, 2; Figure 4.1) as simulated, was measured with four fiber-optic temperature sensors (Neoptix, Inc, Quebec, Canada) placed next to the antenna inside the phantom. These were accessed via 8 holes on the face of the phantom (Figure 4.3.c-d). Decoupling bias was provided via a DC power supply. The temperature was sampled at 1Hz for 31min: (i) with the RF power turned-off for the first minute, as baseline; (ii) with the RF turned-on for 15min at 30W; and (iii) with the RF turned-off for 15min during cool-down. Temperatures recorded at the 8 sensor locations in the absence of the antenna were used as a reference to define the local SAR exposure, assuming:

$$SAR = C_{saline}\frac{\Delta T}{\Delta t} \qquad \textbf{[4.5]}$$

which neglects the effects of perfusion and diffusion. Here, $C_{saline}$=4180 J/kg/°C is the heat capacity of the saline, and $\Delta T$ (°C) is the temperature rise during $\Delta t$ (sec).

We report reference ΔT, ΔT with the antenna present at both insertion depths, the reference local SAR from Eq. [4.5], and the local temperature in the presence of the antenna normalized for a 4W/kg exposure scaled using the reference SAR measurement. Unlike the reference SAR distribution, local SAR in the vicinity of conducting leads can potentially be highly non-uniform [55, 164]. Because the precise spatial sensitivity of the thermal probes is uncertain, for purposes of comparing experimental thermally derived local SAR with the computed 1g-averaged local SAR,

values are reported within a spatial ±0.5cm error cube.

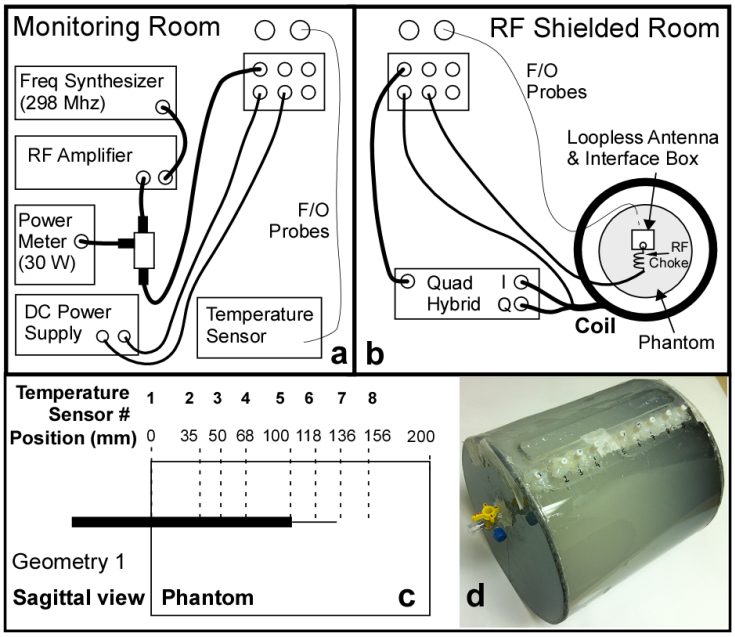


**Figure 4.3.** Schematic of the heat testing setup at 7T. (a) RF components and temperature recording devices are placed in the monitoring room. (b) The coil, the experimental phantom with the loopless antenna and fiber-optic temperature probes, and the transmit coil are located inside the RF shielded room. (c) Schematic of the heating phantom showing the locations of the thermal probes (dotted lines). Insertion depth of 100mm in Geometry 1 is shown. (d) Picture of the actual phantom.

## 4.2.6. Imaging vascular specimens

To compare the imaging performance of 7T and 3T loopless antennae, high resolution axial MRI was performed on human carotid artery specimens harvested from decedents in a study approved by this institution's Office of Human Subject Research Institutional Review Board. Specimens and detectors were positioned at the center of a 6cm diameter 12cm long phantom, and immersed in 0.35g/l saline. Comparable 10-slice 3D high-resolution (80x80µm$^2$x1mm) balanced steady-state free-precession (b-SSFP) pulse sequences were applied at both $B_0$ values (7T: TR/TE=34/17ms, FOV=70x70 mm,

scan duration=13.3min; 3T: TR/TE=38/19ms, FOV=30x30mm, scan duration=13.1min). $T_2$-weighted MRI was performed with turbo spin-echo (TSE) sequences. For SNR comparisons, TSE images with 80x80μm$^2$x1mm voxel sizes were acquired at 7T and 3T (1mm slices, TR/TE=1500/32ms, echo train length ETL=12, FOV=60x60 mm, BW=69.9 and 65.6Hz respectively). Higher resolution (40 and 53μm in-plane) TSE images were also acquired at 7T (1mm slices, TR=1.5s, TE=32 and 40 ms, FOV=60x60mm$^2$, ETL = 14 and 12, BW = 66.7 and 88.3 kHz for 40 and 53μm resolution, respectively). For display, images are scaled by the radial distance ρ from the antenna, to compensate for the sensitivity of the device [8].

## 4.3. Results

### 4.3.1. Computed SNR and SAR

The computed SNR is represented by the solid black contours in Figure 4.4(a-d). In the axial plane at the junction, the diameter of the 50,000 ml$^{-1}$Hz$^{1/2}$ SNR contour at 7T is 3.2-times larger than the same contour at 3T, representing a 10-fold increase in effective FOV area of the device. Along the long axis, the area enclosed by the 50,000 ml$^{-1}$Hz$^{1/2}$ contour is 4-times higher at 7T vs 3T, leading to a 13-fold increase in the total effective FOV volume. The new SNR calculations at 1cm from the junction are combined with prior data from lower fields [161] and plotted as a function of $B_0$ in Figure 4.5. The new data demonstrate that the quadratic $B_0$ dependence of SNR observed at lower fields for the loopless antenna [161], extend to 7T.

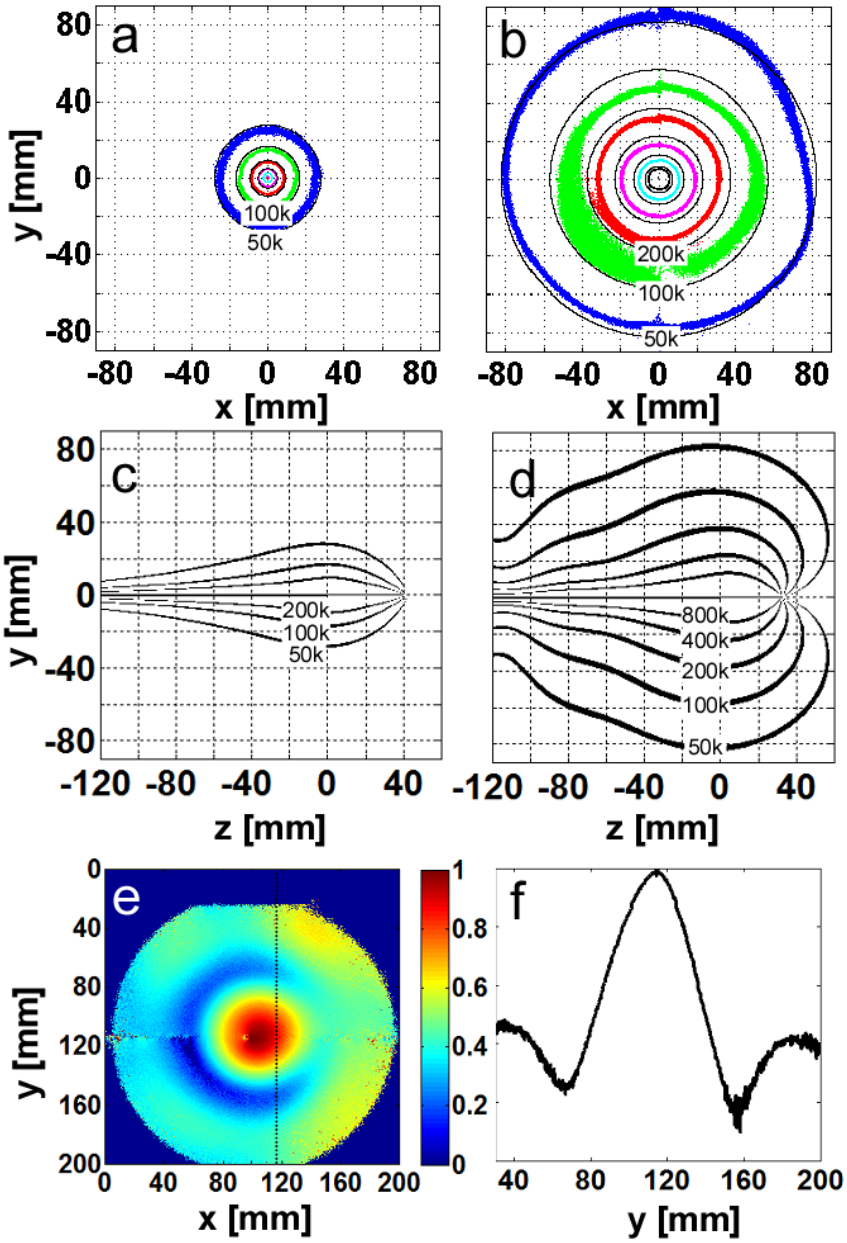


**Figure 4.4.** (a) Theoretical (solid, black) and experimental (colored) absolute SNR [$ml^{-1}$ $Hz^{1/2}$] on the axial whip junction plane of the λ/4 length loopless antennae in 3.5% saline at 3T, and (b) 7T. The experimental data plotted have a 10% tolerance. (blue, 50,000; green 100,000; red, 200,000; purple, 400,000; cyan, 800,000 $ml^{-1}$ $Hz^{1/2}$). Theroretical absolute SNR [$ml^{-1}$ $Hz^{1/2}$] along the long axis of the antenna is plotted in (c, 3T) and (d, 7T). (e) Axial $B_1^+$ map at the whip junction, and (f) $B_1^+$ profile along the dotted line in (e) at 7T. $B_1^+$ varies by ~80%.

Figure 4.6 shows the 1g averaged SAR at 7T for the two geometries (Figure 4.6a-c), and at 3T in Geometry 1 (Figure 4.6d), normalized to a uniform 4W/kg applied RF exposure. The analysis predicts maximum local heating along the cable that, for Geometry 1, is at least no greater than 3T. The computed 1g averaged SAR at the same locations along the antenna where the temperature measurements were made, are plotted in Figure 4.7. The maximum 1g averaged SAR is less than 12W/kg at 7T in all configurations.

## 4.3.2. Experimental SNR and safety testing

As shown in Figure 4.4.e-f, the observed applied $B_1$ at 7T varies by ~80% resulting in a 70% variation in measured signal over a ~16cm diameter cylinder that approximates the effective FOV surrounding the antenna. This reduced the sensitivity of measurements at low $B_1$ locations, even though images were acquired using 9 different flip-angles to compensate for the non-uniform $B_1$ via Eq. [4.3]. At 3T, the $B_1$ field variation was only ~10% (~1% variation in measured signal) over a 5cm diameter cylinder approximating this antenna's smaller FOV and imaging with multiple flip-angles did not compromise the sensitivity of the $B_1$ field measurements.

The $B_1$ corrected experimental SNR data in the axial plane at the junction are plotted in Figure 4.4(a,b). They overlap the theoretical contours. The effective antenna FOV defined by the area of the contours circumscribing the same SNR or higher in the axial plane, increases by a factor of 11.5 from 3T to 7T for regions with SNR>$10^5$ $ml^{-1}$ $Hz^{1/2}$ (green contours, Figure 4.4a, b). The SNR improvement at 7T compared to 3T is

5.7±1.5 over the range 5 ≤ ρ ≤100 mm in the plane of the antenna junction, consistent with the quadratic (5.4-fold) SNR gain with $B_0$ predicted by the EM calculations. Scatter and deviations evident in the SNR data (Figure 4.4b) are attributable to flip-angle variations that are not perfectly accounted for. The experimental SNR measurements at ρ=1cm for 3T and 7T are included in Figure 4.5. These data are both consistent with, and extend empirically the prior SNR measurements at 1.5T, 3T and 4.7T that demonstrate a $B_0^2$ dependence of SNR for the loopless antenna detector.

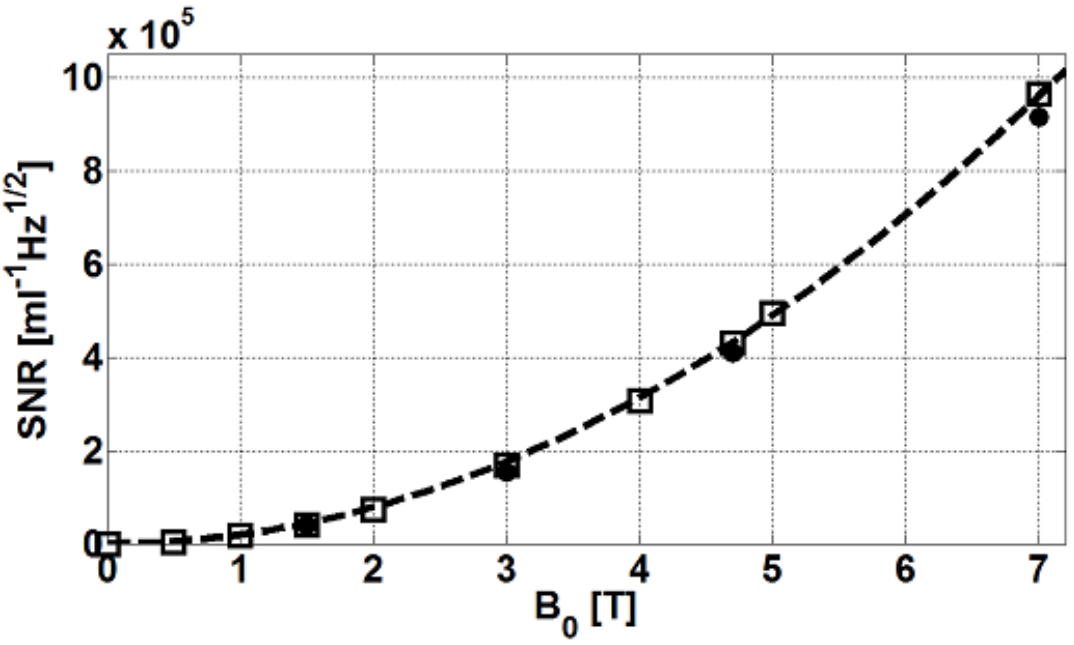


**Figure 4.5.** Absolute SNR (ml-1Hz1/2) computed by EM MoM (square points) at ρ=1cm from the junction of antennae made with λc/4 cable portions tuned at 0.5, 1, 1.5, 2, 3, 4 ,4.7, 5 and 7T in 0.35% saline. Experimental values measured previously (1) at 1.5, 3 and 4.7 as well as our current 7T measurements are overlaid (solid circles). The data are fit to a quadratic curve (dotted line). Experimental data are corrected for system NF but include cable losses.

The raw experimental temperature measurements, and temperature change normalized for 4W/kg exposure are listed in Table 4.1. The observed temperature changes are all below 1°C, as recorded during the 15min RF exposure at an actual reference applied local SAR of 1.4-3.7W/kg. Normalization of the temperature change for a 4W/kg applied RF exposure, increases the projected temperature change to a maximum of 1.9°C at the insertion point. The experimental local 1g averaged SAR determined from the temperature measurements is included in Figure 4.7 for all configurations studied. The experimental and computed SAR are in reasonable agreement.

**Table 4.1.** Measured temperature increases (top), and temperature change normalized to 4W/kg local SAR exposure (bottom).

| Temperature Sensor Number | 1 | 2 | 3 | 4 | 5 | 6 | 7 | 8 |
|---|---|---|---|---|---|---|---|---|
| **Temperature change (°C) during 15 min of RF exposure (raw measurements)** | | | | | | | | |
| Geometry 1, no probe | 0.2 | 0.6 | 0.7 | 0.7 | 0.5 | 0.7 | 0.5 | 0.4 |
| Geom. 1, 35 mm insertion | 0.5 | 0.6 | 0.7 | 0.7 | | | | |
| Geom. 1, 100 mm insertion | 0.2 | 0.5 | 0.6 | 0.6 | 0.5 | 0.5 | 0.5 | 0.4 |
| Geometry 2, no probe | 0.3 | 0.3 | 0.2 | 0.2 | 0.5 | 0.3 | 0.4 | 0.4 |
| Geom. 2, 100 mm insertion | 0.3 | 0.5 | 0.5 | 0.3 | 0.3 | 0.1 | 0.1 | 0.4 |
| **Temperature change (°C) in 15 min normalized to 4 W/kg reference ($\Delta$T=0.86°C)** | | | | | | | | |
| Geom. 1, 35 mm insertion | 1.9 | 0.8 | 0.8 | 0.9 | | | | |
| Geom. 1, 100 mm insertion | 0.8 | 0.8 | 0.7 | 0.7 | 0.9 | 0.6 | 0.8 | 0.9 |
| Geom. 2, 100 mm insertion | 1.1 | 1.6 | 1.6 | 1.2 | 0.4 | 0.3 | 0.2 | 0.9 |

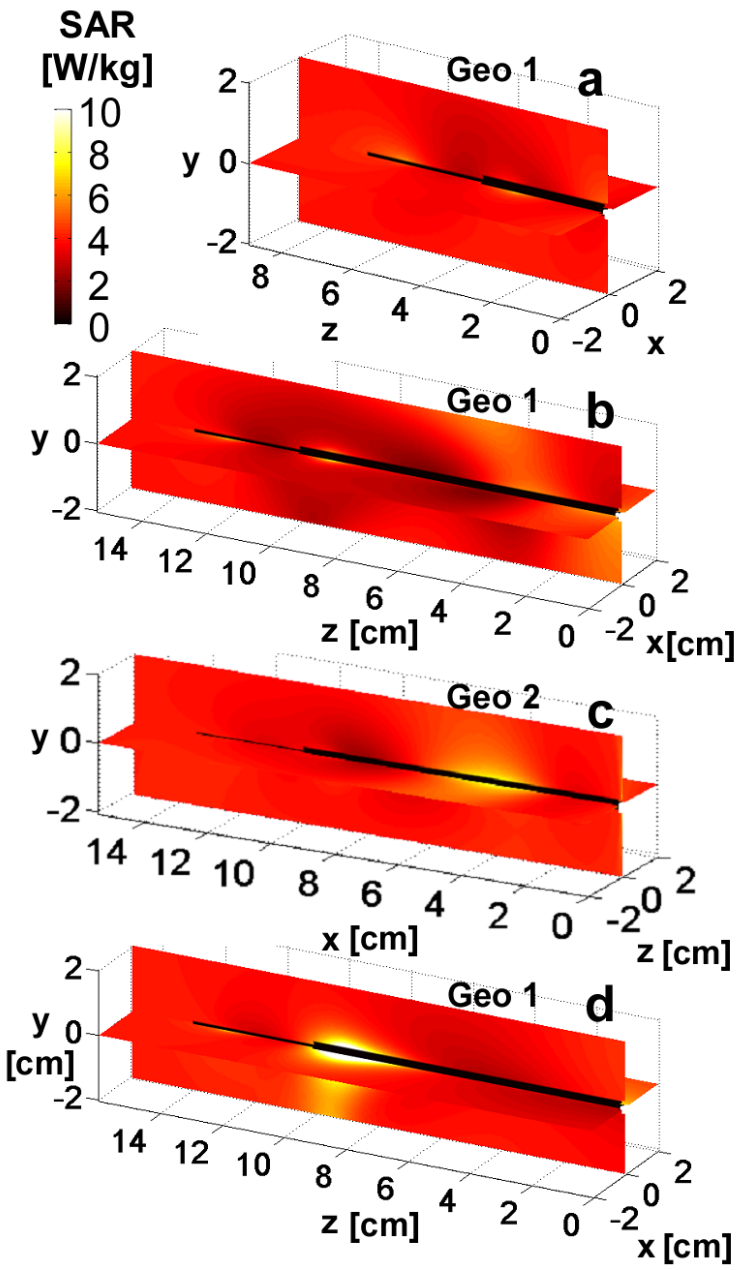


**Figure 4.6.** The computed 1g averaged SAR normalized to 4W/kg applied local SAR is shown on the coronal and sagittal antenna planes at 7T for insertion depths of (a) 35mm, and (b,c) 100mm. Part (d) shows the SAR computation for 3T with a 100mm insertion depth. Part (c) is the distribution in geometry 2 and parts (a,b,d) are in geometry 1. Axes on (a-d) denote position in [cm].

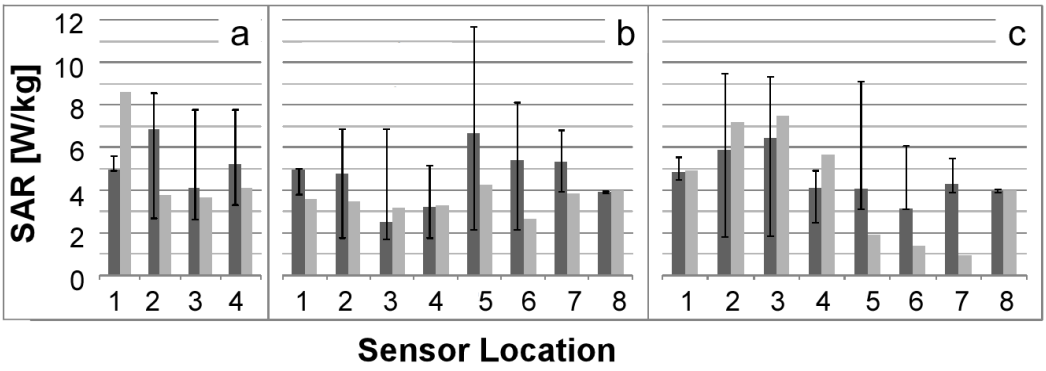


**Figure 4.7.** Computed (dark gray) and measured (light gray) local 1g averaged SAR at 7T for geometry 1 at 35 (a), 100 (b) mm insertion depths, and for geometry 2 at 100mm insertion depth (c). Data are normalized to 4W/kg local reference SAR, with error bars denoting minimum and maximum within a ±0.5cm placement error cube.

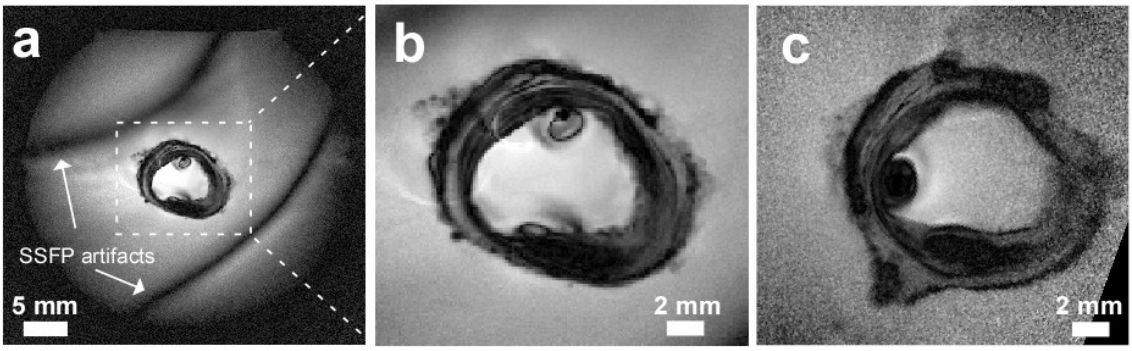


**Figure 4.8.** (a) Full FOV, high-resolution SSFP image of a human carotid artery acquired at 7T with 80 µm in-plane resolution. (b) Same image with the central region expanded (dashed lines in Fig. 6.a) for comparison with (c), a 3T 80µm image from the same specimen using comparable acquisition parameters (position slightly shifted).

## 4.3.3. High-resolution MRI

SSFP images of human carotid arteries are displayed in Figure 4.8. Fine tissue structure is seen in both 3T and 7T images, but the superior SNR at 7T is evidenced by the lack of noise at the periphery. Banding artifacts due to $B_0$ and $B_1$ inhomogenity

(Figure 4.8.a) limited the realization of better resolution at 7T using b-SSFP. This was not the case for TSE, where, as shown in Figure 4.9, resolution was increased further to 40µm. Vessel wall, fibrous cap and calcifications confirmed by histology (Figure 4.9.e), are seen in all images. In Figure 4.9, the mean SNR advantage at 7T vs 3T for the 80µm images is 5.9 in the square annotated regions, and 5.0 at a radius of 1cm from the antenna junction, consistent with the theoretical and experimental analysis from the saline phantoms. The circular structures next to the antenna are bubbles in the media. Compared to the other 7T images, the contrast at 40µm resolution was limited by the longer TE of 40ms, the shortest allowed at this resolution by the scanner's maximum achievable gradient strength.

## 4.4. Discussion

We have for the first time, analyzed, built, safety-tested and demonstrated high-resolution MRI, from an interventional loopless MRI detector operating with a standard commercial 7T human MRI scanner. We have provided both analytical and experimental evaluations of its performance relative to an equivalent device at 3T, and moreover shown, both experimentally and theoretically, that its SNR performance increases quadratically up to 7T. This extends prior work showing a $B_0^2$ dependence of SNR under optimal conditions on a 3T human scanner and a 4.7T animal system [161]. This behavior is attributable to direct E-field losses which, unlike conventional head and body MRI, do not vary significantly with operating frequency [161]. Thus, the noise level stays almost the

same while the signal power increases as $B_0^2$. The increase in SNR at 7T is accompanied by an approximately 10-fold gain in useful FOV area, defined here as the ratio of areas subtended by equal SNR contours at 7T and 3T. The SNR gain enabled–for the first time in a human-capable MRI system–the imaging of human vascular specimens at 40-50µm in-plane resolution. SSFP MRI sequences provided good contrast and high SNR at 3T, but at 7T, resolution below 80µm was compromised by banding artifacts. These may be ameliorated by increasing RF power–which in the present studies was well below regulatory guidelines–and bandwidth. Resolution with TSE is ultimately limited by the available gradient strength: about 40µm with TE=40ms in the present studies.

Comparisons of the experimental SNR performance of MRI detectors at different field strengths are often fraught with concerns of whether one is comparing best prototypes of a given design. This is addressed in conventional MRI with the concept of the "intrinsic SNR" (ISNR) which excludes E-field losses in the MRI coils [169]. For the loopless antenna, the primary E-field losses are not in the conductor. This is evidenced by the agreement between the computed SNR which assumes that the antenna conductor has infinite conductivity, and the actual antenna which does not (Figs. 4,5). Instead, the E-field losses are primarily from conduction currents in the sample that extend between the whip and cable which effectively completes a "loop" circuit for the loopless antenna, and not those currents directly induced in the sample by the antenna's $B_1$. Except for the fact that the numerical computed SNR accounts fully for all of the E-field losses including these conduction losses in the sample, this theoretical SNR

could be considered the ISNR because it is the maximum SNR that can be achieved for this specific antenna geometry and sample. To avoid confusion, we apply the term "design SNR" for this maximum computed SNR. The agreement between our experimental SNR measurements and the computed design SNR at both field strengths (Figs. 4, 5), supports the view that the quadratic SNR dependence is the best that can be done for this design, and moreover, that such performance is realizable.

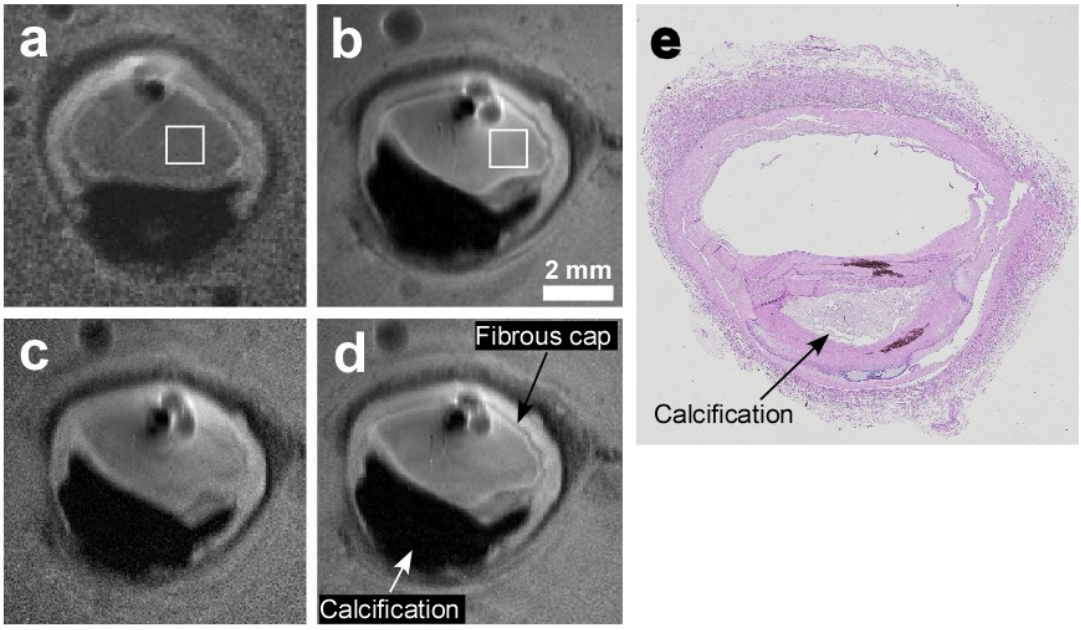


**Figure 4.9.** High resolution TSE images of human carotid artery specimens in saline at 3T (a) and 7T (b-d). Slice thickness is 1 mm, in-plane resolution is 80 µm (a, b), 40 µm (c) and 53 µm (d). Histology result for the samples used at 7T images is shown in (e). 3T (a) and 7T(b) images are acquired with the same pulse sequence parameters except for a 6.5% increase in bandwidth at 7T due to system constraints. The mean SNR improvement inside the annotated squares in (b) is 5.85 compared to (a).

With the higher SNR, our results suggest that the useful FOV of the loopless antenna can extend to ~20 cm at 7T, which could potentially eliminate the need for additional coils for guiding or targeting the antenna, or indeed for performing MRI in

general. Although the whip of the antenna is shorter at 7T, sensitivity of the antenna extends up to ~1cm beyond the tip (Figure 4.4d) and there is no reduction in the FOV area along the longitudinal direction of the antenna due to the shortened whip length, as compared to 3T. While the sensitivity of the antenna is inversely proportional to the radial distance (ρ) from the device and is therefore very nonuniform, $B_1$-inhomogeneity at 298MHz is a problem now shared by virtually all MRI detector designs [151] (Figure 4.4e,f). For the loopless antenna, the profile does remain relatively immune to sample heterogeneity over a range of tissue electrical properties at 298 MHz. Use of the device for both transmit and receive would remove interactions between the transmitter and receiver, and any effect they might have on the SAR distribution. Recently, nonuniformity in the excitation field of internal transmit/receive prostate coils at 7T was successfully addressed using adiabatic pulses [154], and we have used adiabatic pulses with loopless antennae for MRI endoscopy at 3T using only a few Watts of power[162, 163].

According to U.S. FDA safety guidelines, whole body average exposure of ≤4W/kg for 15min, and/or local 1g averaged SAR ≤12W/kg are not considered a significant risk [170]. We analyzed the RF safety of the 7T device both theoretically and experimentally and found that local 1g averaged SAR≤12W/kg at an applied RF exposure of 4W/kg (Figure 4.6-7, Table 4.1). Moreover, heating did not exceed 1.9°C after 15min exposure normalized to this SAR level in the configurations tested, suggesting that the device could potentially be safely operated at 7T.

The presence of local “hot spots” could pose additional risks, however, to the

safety of internal devices at 7T. Here we theoretically determined the location of the maximum local SAR, by EM analysis in the absence of the antenna, then performed safety testing of the device at this location. In the absence of the antenna, peak local 1g averaged SAR was about 3-times the average SAR at 7T. The numerical SAR analysis indicates that the effect on the 1g averaged SAR distribution of introducing the device remains relatively local. Compared to having no antenna present, neither the total power applied to the transmit coil to achieve unit current, nor the whole sample average SAR changed when the antenna was introduced in all of the configurations studied. By conservation of energy, this means that the antenna does not represent a significant increase in load or power loss to the head coil, and that any local increases in SAR with the antenna present, must be offset by reductions elsewhere, as is also evident in the experimental data (Table 4.1: readings with $\Delta T<0.8°C$ vs reference exposure of 0.86°C). In situations where the antenna is not at a local SAR hot spot, the antenna's presence should not pose significant additional risks, assuming that it is properly decoupled. If, on the other hand, the antenna is located at an SAR hot-spot, the presence of the antenna could result in a local SAR that exceeds the FDA guideline, although this did not occur in the present studies. Note also that an inadequately decoupled device will have induced currents which, via Lenz's law, will counter the field near the antenna, deleteriously affecting performance by generating "decoupling artifacts". These are absent from the images in Figure 4.8 and Figure 4.9.

Insertion depth did not much affect the computed 1g averaged SAR or the

measured heating, although both were slightly higher at the shallower (35mm) depth where the entry point is essentially at the antenna junction. The heating of unprotected wire leads can be exacerbated when insertion lengths approach λ/4 in the medium [55, 164], and in the present case the whip is in fact tuned to λ/4. Thus, the data in Table 4.1 illustrate the efficacy of the decoupling circuitry as a potential solution to the problem of heating of ~λ/4 leads. The antenna length from both simulations and experiments at 7T was only about 17cm. While the lengths and insertion depths investigated may not be suitable for whole-body interventional studies, they are appropriate for this commercial 7T brain MRI scanner, with potential applications that could include intra-cranial MRI-guided remote targeting of diseased structures in the brain, or the remote placement of electrodes for deep brain stimulation[31, 171, 172].

In conclusion, these new results from interventional loopless antennae demonstrate a quadratic SNR improvement with $B_0$ that extends to 7T to provide an over 20-fold SNR improvement and 100-fold increase in FOV area compared to the equivalent device at 1.5T. These advances can translate to ~50μm in-plane resolution and new opportunities for potentially safe, high-resolution MRI in humans at 7T, but additional work is needed.

# Chapter 5.

# Fat/Water Imaging

## 5.1. Introduction

Atherosclerosis is a leading cause of heart attacks, strokes, and peripheral vascular disease worldwide. The American Heart Association (AHA) classifies 5 clinically relevant phases of disease progression, including an early phase involving small lesions of foam cells and lipid droplets progressing to muscle cells, fibrils and lipid deposits; and an advanced phase of lesions with lots of extracellular lipids and fibrous caps that are prone to rupture when lipid content is high and caps are thin[173]. Plaque lipids cannot be unambiguously detected by any existing clinical vascular imaging modality. Thus, intravascular (IV) MRI employing chemical-shift lipid selection has the potential for providing unique information about a plaque component that could prove central to disease characterization. In this chapter, we use the three-point Dixon method[69] and design spectrally selective $B_1$-insenstive RF pulses[71] to distinguish fat and water content of the images. The spectrally selective $B_1$-insenstive RF pulses are tested on phantoms using an intravascular loop coil[162] at 3 Tesla (T). Human iliac artery specimens are scanned *in vitro* with the Dixon method using intravascular loopless antennae[54] at 3 and 7T as a prelude to *in vivo* studies.

## 5.2. Theory

### 5.2.1. Spectrally Selective BIR4 Pulses

The $B_1$-insensitive rotation (BIR4) pulse [174] consists of three segments: 1. a reverse adiabatic half passage (rAHP) segment; 2. an adiabatic full passage (AFP) segment; and 3. an AHP segment[174-176]. An arbitrary flip angle (FA) can be achieved using the BIR4 pulse by introducing a phase step of +[180°+FA/2] followed by -[180°+FA/2] at the start and end of the middle (AFP) segment, respectively. Long and short 0° BIR4 pulses have been used for measuring $T_2$ [177]. A modified version of the BIR4 pulse wherein symmetrical and asymmetrical pause durations are added before and after the middle segment has been used for T2 preparation[178] and solvent suppression, respectively[179]. In this work, we add a pause duration either before or after AFP segment to suppress fat or water components of the signal[71].

A modified 0° BIR4 pulse with a pause after the AFP segment is shown in Figure 5.1. During the first segment, an rAHP flips the magnetization into the transverse plane. In the second segment, an AHP pulse with the same amplitude and frequency modulation functions as the first rAHP pulse, is applied. During this pulse, the transverse magnetization remains in the transverse plane and accumulates more phase dispersion due to chemical shift differences in the constituent signals. The longitudinal magnetization is inverted during the AFP segment. During the delay after the AFP segment, the transverse magnetization acquires additional phase depending on the

resonance frequencies of the different moieties of, say water ($H_2O$) and fat ($-CH_2^-$) signals, and the duration of the delay. In a conventional BIR4 without any pauses between the segments, phase acquired during rAHP and the first half of the AFP pulses is exactly compensated by the second half of the AFP pulse and the AHP pulse. However, since the modified BIR4 pulse is not symmetric, a residual phase is accumulated during the pause after the AFP segment ($\phi = \Delta\omega \cdot \tau$), where Δω is the off-resonance frequency of the magnetization and τ is the duration of the delay. If the residual phase accumulated by the magnetization is equal to 90° for a certain Δω, then that frequency component will be orthogonal to the applied RF field and will be returned to the transverse plane after the AHP pulse. However the component of the magnetization that does not experience any frequency offset will be tilted to the longitudinal plane[71]. By this means, spectral selection will be achieved. The time delay (τ) after the AFP segment determines the off-resonance frequency (Δω) to be flipped into the transverse plane. By changing the center frequency of the pulse, Δω that is excited can be moved to any arbitrary resonance frequency and chemical selection is achieved.

## 5.3. Methods

### 5.3.1. Designing Spectrally Selective BIR4 Pulses

Spectrally selective BIR4 pulses[71] were designed using Matlab. The Bloch equation was solved numerically to simulate the performance of the designed pulses for

an off-resonance frequency range of ($\Delta B_0$: [-600, 600] Hz) with 10Hz steps and for $B_1$ amplitudes ranging from 0-40μT with steps of 1μT.

The resultant spectrally selective BIR4 pulses were used as RF excitation pulse in GRE based sequences. The pulses were calibrated and their performances first tested using a quadrature T/R head coil inside the Philips 3T Achieva MR scanner. A cylindrical water-filled phantom and a small tube containing vegetable oil were placed inside the head coil. Water- and fat-suppressed images are acquired using GRE sequences with TR/TE = 307/4ms.

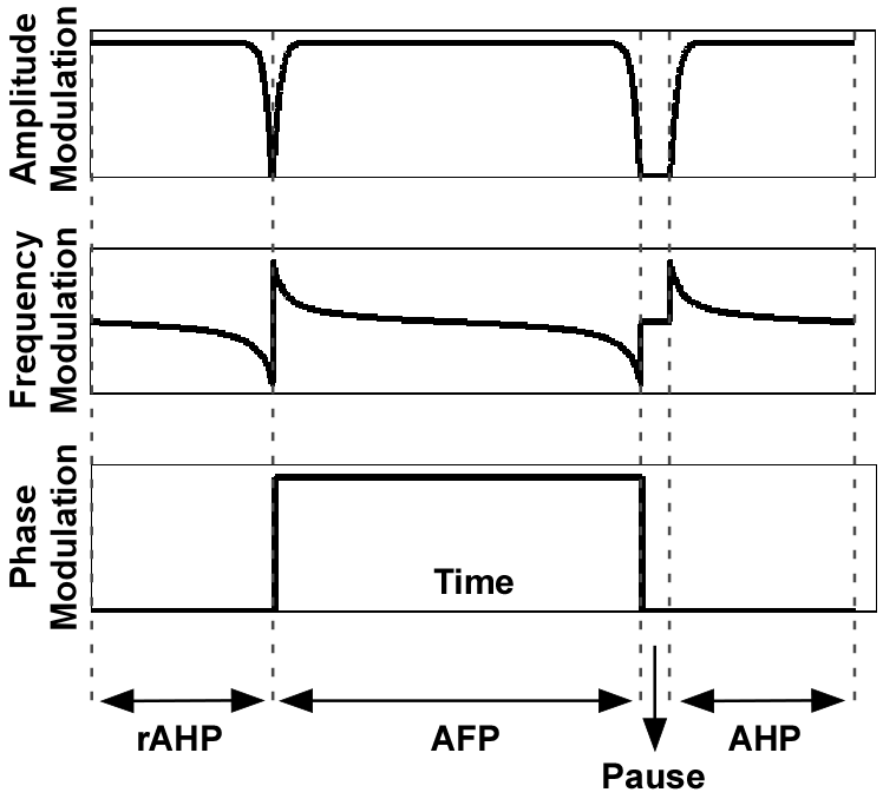


**Figure 5.1.** Amplitude, frequency and phase modulation waveforms of a modified BIR4 pulse are plotted. If the pause duration is set to '0', then these waveforms represent a conventional BIR4 pulse. The BIR4 starts with a rAHP segment followed by an AFP pulse and ends with an AHP pulse. All pulses are modulated using same shapes and amplitudes.

Next, an intravascular solenoidal loop coil[162] was immersed inside a water bath. The vial containing vegetable oil was also placed inside the water bath next to the intravascular coil. GRE sequences with the RF excitation pulses replaced by the spectrally selective BIR4 pulses were used (TR/TE = 200/6ms) in the Philips scanner.

## 5.3.2. Three-point Dixon Method

MRI experiments were conducted on 3T and 7T Philips Achieva MR systems using 2.2mm outer-diameter receive-only loopless antennae[51] tuned to 3 and 7T MRI frequencies. Autopsied human iliac artery specimens are placed inside a phantom filled with 3.5 $gL^{-1}$ saline to mimic the body's RF electrical properties. The loopless antenna was inserted inside the lumen and MRI was excited by the Philips body coil and Nova Medical head coil at 3T and 7T, respectively.

The three-point Dixon method was used to acquire fat and water images from three-acquisitions with varying echo times[69]. Fat/water axial and coronal images were reconstructed offline in Matlab. More details on the water- and fat-only image reconstruction can be found in Section 2.5.1 [69]. T1-weighted gradient echo (T1-w GRE) sequences with TE=7.9, 8.4 and 8.9ms were used at 7T. Coronal images were obtained from 3D data sets (repetition time, TR=0.15s; flip angle, FA=50°; voxel size= 50x100x500$\mu m^3$; field-of-view, FOV=60x60x2.5$mm^3$; scan-time=237s). Axial images have 200μm resolution (TR=0.5s; FA=75°; FOV=60x60$mm^2$; scan-time=452s). At 3T, axial 3D T1-w FFE images were acquired with 200μm in-plane resolution (TR=0.2s; TE=4.6, 5.76, 6.91ms; FA=50°; FOV: 60x60x8 $mm^3$; scan-time=792s). To provide uniform contrast,

axial images were corrected for the ~1/r dependence of the receiver's sensitivity.

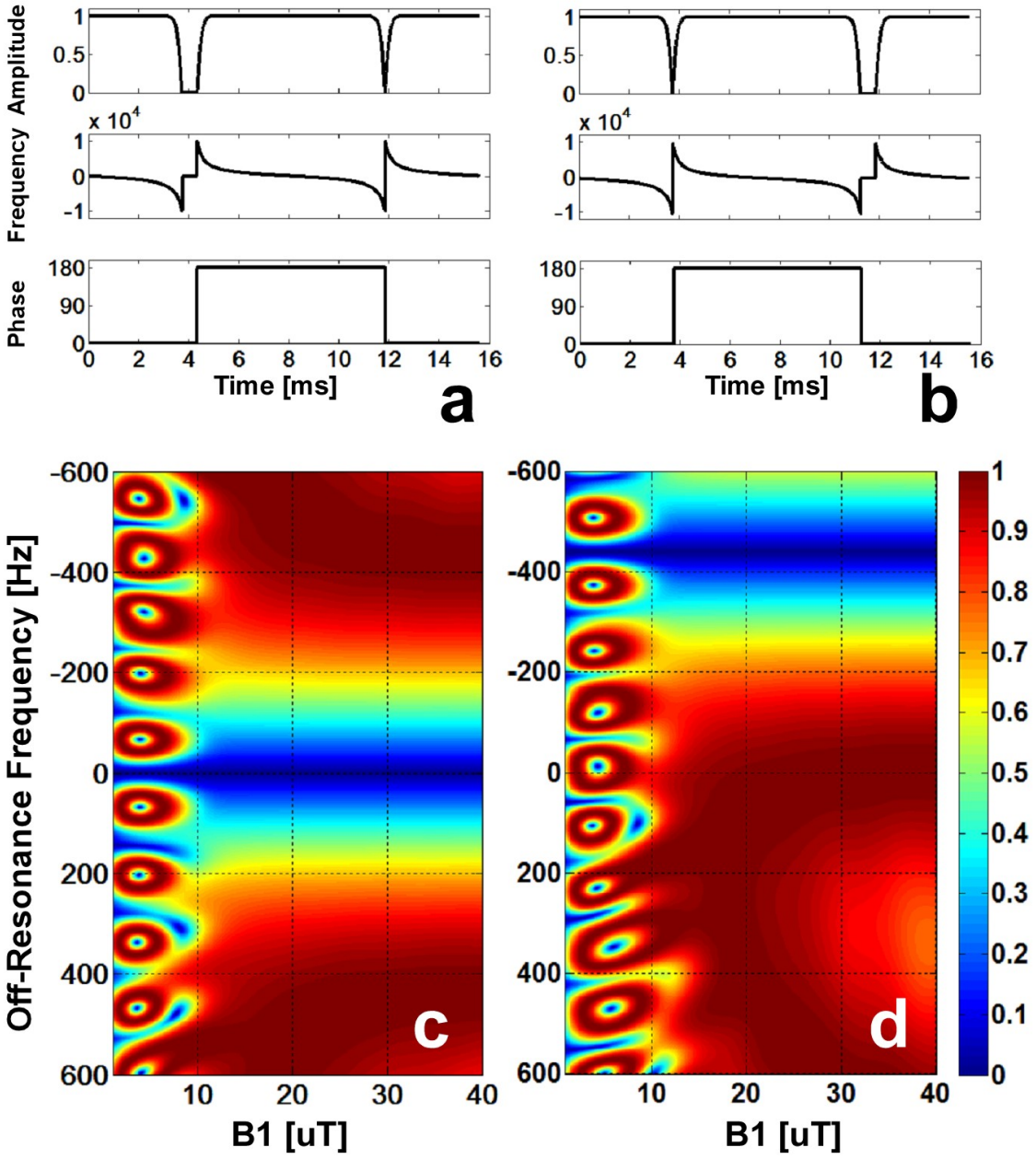


**Figure 5.2.** Amplitude, frequency and phase modulation waveforms of (a) the water- and (b) the fat-suppression BIR4 pulses are plotted. Ratio of the transverse magnetization to the longitudinal magnetization at the end of the water- and fat-suppression pulses are shown in (c) and (d) respectively.

## 5.4. Results

### 5.4.1. Spectrally Selective BIR4 Pulses

15.6ms long modified BIR4 pulses were designed for water-suppression with a 600μs pause before the AFP segment (Figure 5.2.a). A 600μs pause was placed after the AFP segment in the fat-suppression pulse (Figure 5.2.b). The amplitude, frequency and phase modulation waveforms of the water- and fat-suppression pulses are shown in Figure 5.2.a and b, respectively. The center frequency ($f_0$) of the fat-suppression pulse was moved to -440Hz in order to suppress the fat frequencies.

The BIR4 suppression pulses were able to suppress water or fat resonance frequencies provided that the applied $B_1$ was higher than 10μT. Below this threshold, the adiabatic properties of pulses start to fail.

### 5.4.2. MRI Using Modified BIR4 Pulses

Non-selective images acquired at 3T with the quadrature head coil using the water- and fat-suppression pulses are shown in Figure 5.3.a and b, respectively. The residual signal coming from the water phantom in part (a) is attributable to $B_1$ amplitudes lower than the 10μT adiabatic threshold. In the regions where the applied $B_1$ is lower than 10μT, the water signal may not be perfectly suppressed, resulting in residual MR signal appearing in the reconstructed image. In part (b), the signal from the oil phantom is suppressed using the fat-suppression pulse.

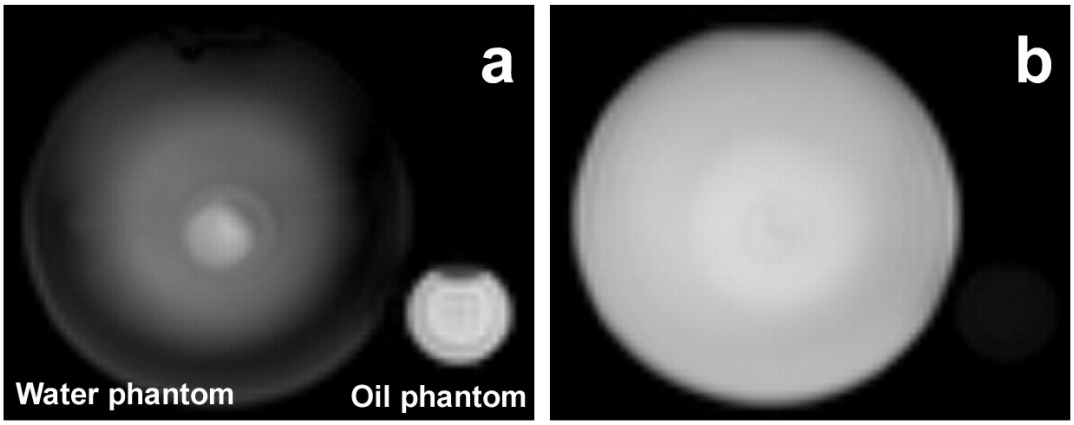


**Figure 5.3.** Head-coil GRE images acquired using (a) the water-suppression, and (b) fat-suppression BIR4 pulses are shown.

Images from the experiment employing the intravascular loop coil are shown in Figure 5.4.a. The vial containing vegetable oil is on the left side of the IV coil, which is positioned in the water bath. MR images are acquired using the IV coil for both transmitting the RF pulses and receiving the MR signal. Water- and fat-suppressed images are shown in Figure 5.4.b and c respectively. Part (b) demonstrates water suppression. In part (c), the residual signal coming from the oil phantom is attributable to other chemical compounds present in the vegetable oil resonating at different frequencies from the primary ($-CH_2^-$) resonance at -440Hz relative to water ($H_2O$).

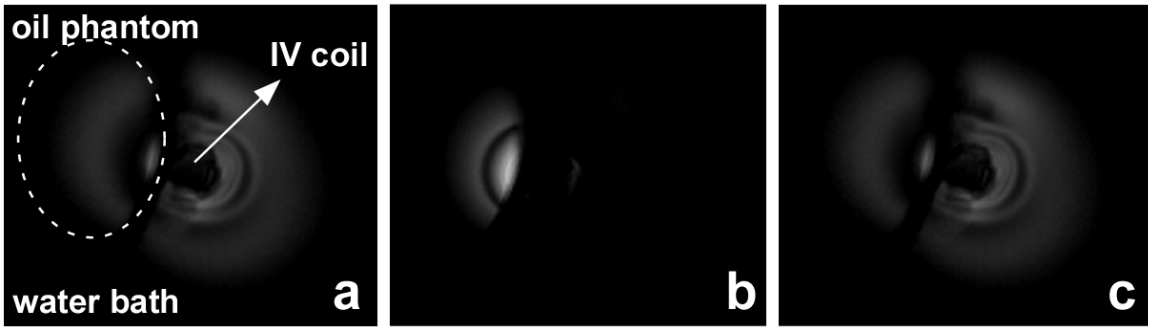


**Figure 5.4.** (a) A vial containing vegetable is placed inside a water bath next to the interventional (IV) loop coil. FFE sequences using the IV coil in T/R mode are acquired with the 15.6ms-long (b) water-suppression, and (c) fat-suppression pulses.

## 5.4.3. Images Acquired Using the Dixon Method

7T images acquired using the interventional loopless antenna are displayed in Figure 5.5, with the top row (a, c) and bottom row (b, d) showing the water- and fat-only images, respectively. Hyper-intense regions in coronal lipid images (Figure 5.5.b) are used to determine subsequent axial scanning locations. Fat is evident in the periphery of the vessel wall (Figure 5.5.d). Calcified plaque regions are also evidenced by signal voids.

In Figure 5.6, 3T water images from a 5-slice 3D stack at the iliac bifurcation are shown with fat-rich regions overlaid in cyan, and a complex (type VI) lesion. Lipidiferous tissue is detected at the bifurcation and adjacent to the vessel wall.

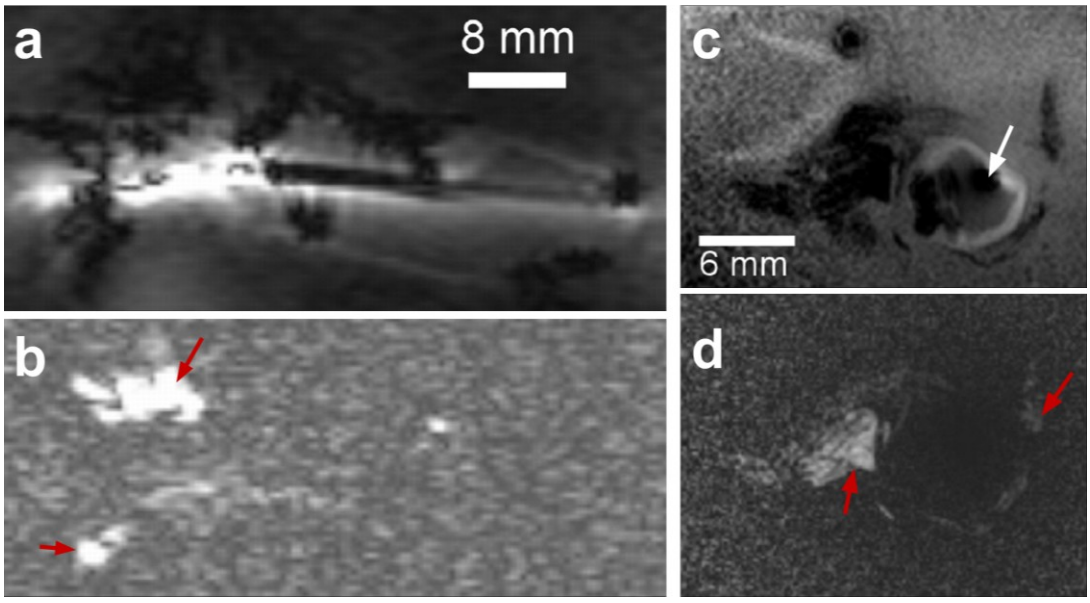


**Figure 5.5.** (a) Coronal water, (b) fat, and (c) axial water, (d) fat images acquired at 7T. Red arrows show the lipid-rich regions adjacent to vessel wall. White arrows point to the intravascular MR detector in both figures.

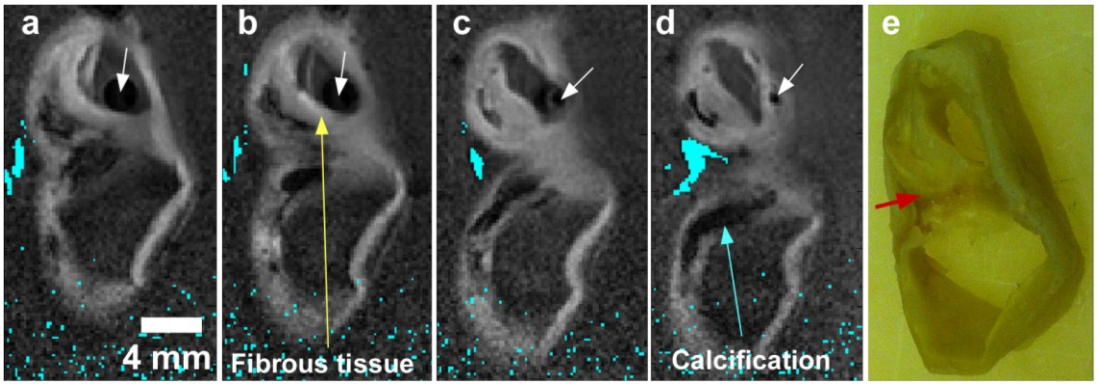


**Figure 5.6.** (a-d) Images from a 5-slice axial 3D scan at 3T. Fat images are intensity thresholded and overlaid on the grayscale water image with cyan, showing the lipid-rich regions next to the vessel wall. Scattered cyan points at the bottom of the images are due to errors in thresholding in low SNR regions. **(e)** Image of the specimen with red arrow indicating lipid-rich area.

## 5.5. Discussion and Conclusion

Modified BIR4 pulses can provide effective water- or fat-suppression. The $B_1$ threshold of the adiabatic pulses depends on their total durations. For instance, reducing the BIR4 pulse length to 6.6ms increased the $B_1$ threshold of 20μT. In order to extend our imaging FOV, we chose longer BIR4 pulses (15.6ms) with the lower $B_1$ threshold (10μT).

IV MRI using loop coils and/or loopless detectors at higher field strengths of 3T and 7T compared with 1.5T can detect fat and lipid deposits adjacent to the vessel wall at high resolution. The ability of chemical-selective IVMRI to unambiguously detect lipid deposits, combined with its ability to measure fibrous cap thickness (FCT) shown earlier[52] offers high potential as a new imaging modality that could uniquely detect all

plaque components–calcification, lipids, and FCT–critical in the characterization of human atherosclerosis[173], and its response to treatments such as lifestyle changes and cholesterol reduction medications.

## 5.6. Future Work

In the future, we plan to image diseased artery specimens with the spectrally-selective BIR4 pulses and intravascular coils. The performance of water- and fat-suppression using modified BIR4 pulses will be compared with the multi-echo Dixon method in a larger number of specimens to enable assessment of the intravascular water/fat imaging.

# Chapter 6.

# Towards Imaging Alzheimer's Dementia

## 6.1. Introduction

Dementia is usually defined as an acquired condition involving multiple cognitive impairments that are severe enough to impair a person's ability to perform everyday activities. Alzheimer's disease (AD) is the most common form of dementia, accounting for 60 to 80 percent of cases. AD gradually worsens over time and has no known cure, but treatments for symptoms are available. Vascular dementia (VaD), which can be associated with stroke, is the second most common dementia type.

Many of the diseases causing dementia have a progressive course and diagnosis is made usually after 5-10 years of onset of the disease. In addition, dementias often have a prolonged end stage period where the patient's independence and ability for self-care is lost, placing a tremendous burden on the patient, family and caregivers. In 2010, AD was cited as the 6$^{th}$ leading cause of death in the United States, and the 5$^{th}$ for those aged 65 or older[180]. Deaths attributed to AD have increased by 68% between 2000 and 2010 while deaths from many other major diseases has decreased [180]. 1 in 9 Americans over 65 and 1 in 3 over 85 years of age has AD [180], therefore as the general population is ageing, the burden of AD on the society is increasing and is expected to increase rapidly over the coming decades. AD not only occurs at later ages, but up to 5% of people with the disease have early onset Alzheimer's disease which appears in those

aged in their 40s and 50s.

AD neuropathology includes amyloid plaques, neurofibrillary tangles and neuronal cell loss[181]. Amyloid plaques are formed by aggregated beta amyloid protein (Aβ) deposits. Aβ is believed to interfere with neuronal activity, resulting in oxidative stress and neuronal cell death [182]. Amyloid plaques generally have a diameter of 20-60μm. Neurofibrillary tangles are paired helical filaments composed of tau protein, which in normal cells is essential for axonal growth and development. However, when hyperphosphorylated, the tau protein forms tangles that are deposited within neurons leading to cell death [182]. Areas of neuronal cell death and synapse loss are found throughout a distribution pattern similar to that of the neurofibrillary tangles, affecting memory and cognitive functions leading to dementia. Neuropathology of AD is depicted in Figure 6.1. AD pathological progresses start 10-20 years before the onset of clinical symptoms.

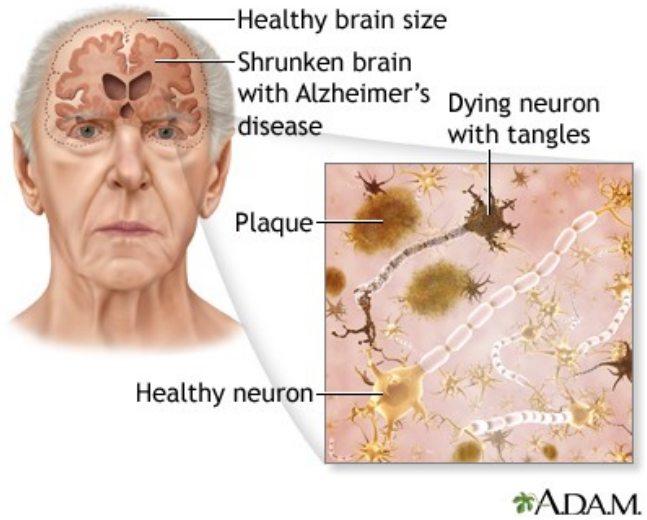


**Figure 6.1.** Neuropathology of Alzheimer's disease is shown. (Adapted from A.D.A.M. Medical Encyclopedia Ref. [1])

VaD is the second most common type of dementia after AD. VaD is caused by inadequate blood flow, which can damage and eventually kill neuronal cells. VaD may occur suddenly following strokes that block major blood vessels, or slowly and gradually as a result of cerebrovascular, multifocal and/or diffuse disease [2].

Cortical microinfarcts, microbleeds, lacunar infarcts and white matter hyperintensities are expressions of VaD. AD and VaD pathologies may also occur simultaneously leading to mixed dementia. In cerebral amyloid angiopathy (CAA), which may cause mixed dementia, amyloid deposition in the vessel walls causes thickening of fibrous tissue and vessel wall thickening, causing hemorrhages and microbleeds.

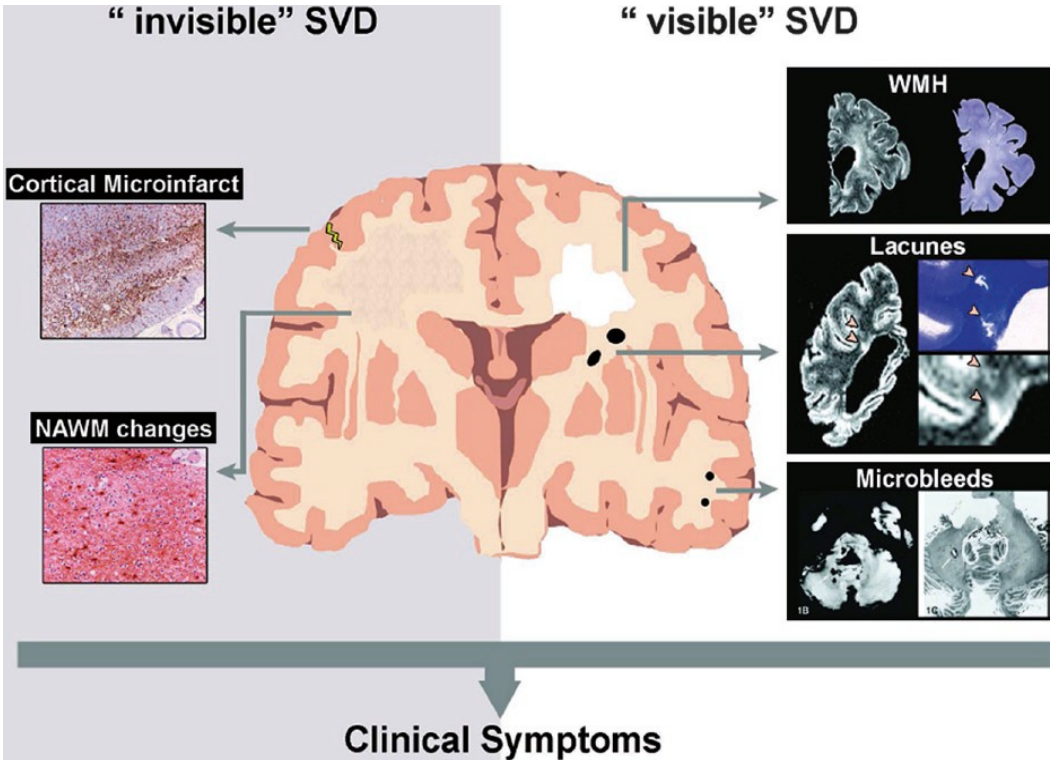


**Figure 6.2.** Different expressions of small vessel disease (SVD) are shown, including postmortem fluid-attenuated inversion recovery (FLAIR) magnetic resonance images and histological sections. Cortical microinfarcts and normal-appearing white matter changes are only histopathologically depicted. (Adapted from Ref. [2])

Current clinical imaging modalities are generally used to rule out causes of dementia other than AD. The formation of amyloid plaques can be detected with a PET scan using Pittsburgh compound-B [183]. While amyloid plaques are present in AD patients, cognitively normal healthy people may also have significant amyloid plaque deposition [181]. As new treatment methods become available and target specific molecular abnormalities, differentiating the primary cause of dementias early on is essential [184]. The development of new imaging techniques may revolutionize the diagnosis of dementia to permit an expanded molecular, structural and metabolic characterization. Such an imaging capability could be used to improve diagnosis, stage each patient, and follow disease progression and its response to treatment.

The MRI characteristics of amyloid plaques have been investigated in transgenic mice inside small bore animal systems using $T_2$ and $T_2$*-weighted sequences [185-187]. However, detecting amyloid plaques in humans are much harder because the size of the amyloid plaques in mouse models (up to 100μm) are larger than human plaques (20-60μm) [188-190], and the smaller brain size of the mice makes high-resolution imaging easier using UHF MRI systems compared to humans[187].

In this chapter, we investigate whether ultra-high resolution MRI can detect pathology associated with Alzheimer's dementia. The improved SNR of interventional loopless antenna at 7T is utilized to acquire images at resolution of <100μm from human brain specimens with AD pathology *in vitro* inside a whole-body human scanner.

## 6.2. Methods

### 6.2.1. Experimental Setup

A receive-only interventional loopless antenna tuned to 298MHz was built. Details on the experimental device can be found in Section 4.2.3. A cylindrical imaging phantom with 15cm diameter and 15cm length was filled with 3.5g/l saline.

Two tissue specimens from the frontal lobe of the brain with and without AD pathology were obtained from the Department of Pathology in accordance with our institution's internal regulations. The specimens were previously fixed and stored in 10% formalin solution (Sigma-Aldrich, St. Louis, MO).

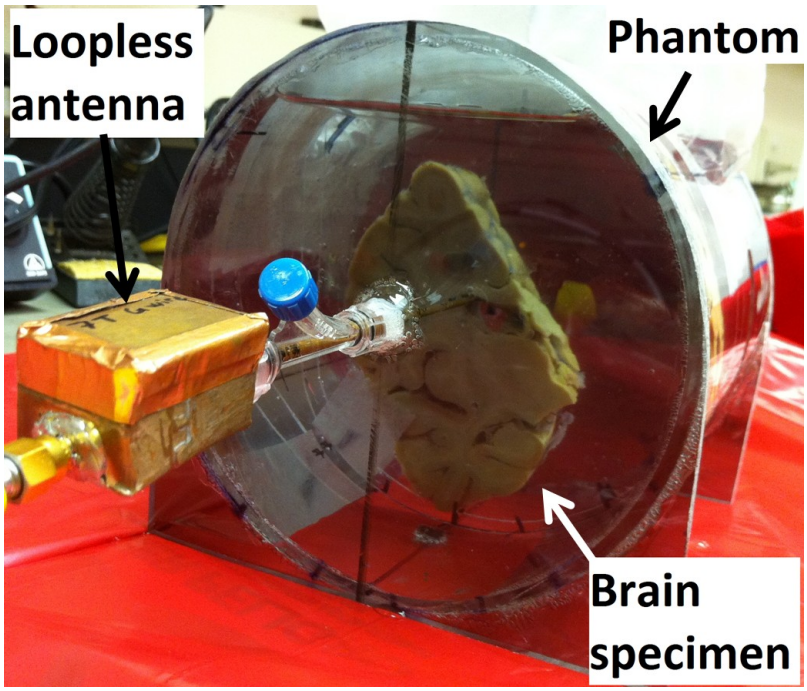


**Figure 6.3.** The experimental setup for studying brain specimens at 7T. The phantom is filled with saline to electrically load the loopless antenna. The brain specimen is placed vertically inside the phantom and the loopless antenna is placed therein.

For imaging experiments, the brain specimens were placed vertically inside the imaging phantom filled with saline. The loopless antenna was inserted such that the cable-whip junction of the device was situated inside the specimen (Figure 6.3).

Imaging experiments are conducted on a whole-body Philips Achieva 7T MRI scanner (Philips Medical Systems, Cleveland, OH). RF excitation was provided by the Nova Medical head coil. The loopless antenna was connected to a 16-channel receive-only interface box, and the remaining 15 channels were terminated with 50Ω.

### 6.2.2. Pulse Sequences

3D single acquisition multi-echo GRE sequences were used. A first set of images were acquired with TR/TEs = 600/15,23,31,39ms; FOV = 60x60x1mm$^3$; and voxel size = 100x100x200µm$^3$. The scan duration was 16min 26s. A second set of images were acquired with TR/TEs = 600/12,22.4,32.8,41.2ms; at the same image FOV as the first set but with voxel size = 60x60x200µm$^3$. Each acquisition was averaged twice and the total scan duration was 54min. In both sets of scans, individual frames reconstructed from 4 different TEs were averaged to generate the final image. The final images are corrected for the ~1/r dependence of the receiver's sensitivity to provide uniform contrast.

## 6.3. Results

MRI of brain specimens without and with AD pathology, at 100µm in-plane resolution with a slice thickness of 200µm are shown in Figure 6.4.a and b, respectively. Localized hypointense micro-lesions were detected in gray matter (Figure 6.4.b) from

the specimen with AD pathology. Images from the same specimens at a different location acquired at a voxel size of 60x60x200µm$^3$ are shown in Figure 6.5. MRI of a specimen with AD pathology is zoomed in Figure 6.5.c; the white arrows point to suspected AD plaque pathology. In the specimen without AD pathology, no noticeable gray matter hypointensities were present Figure 6.5.a.

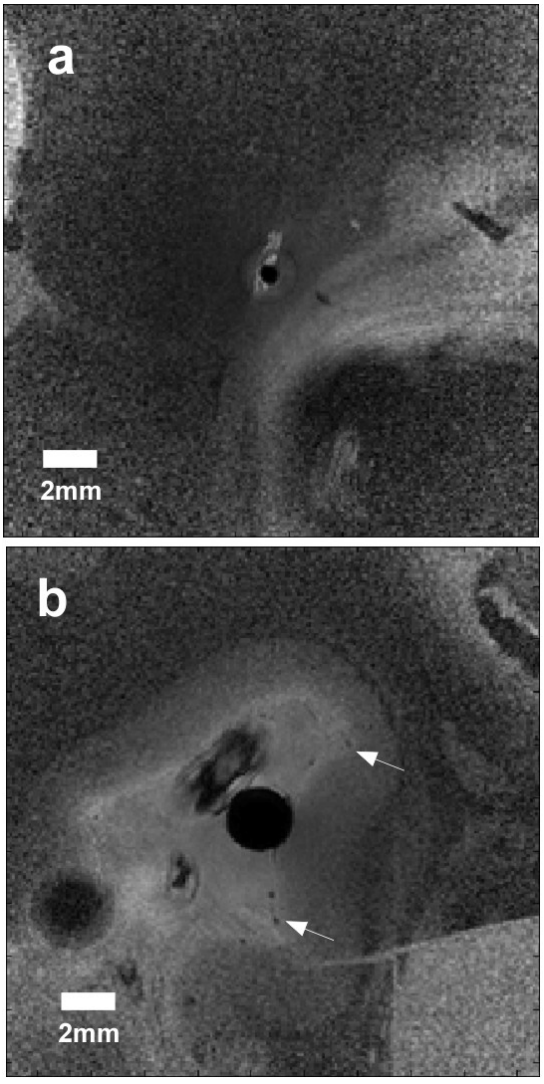


**Figure 6.4.** MRI of brain specimens (a) without and (b) with Alzheimer's disease (AD) pathology at 100µm in-plane resolution. The white arrows point to signal hypointensities that are suspected to be senile plaques.

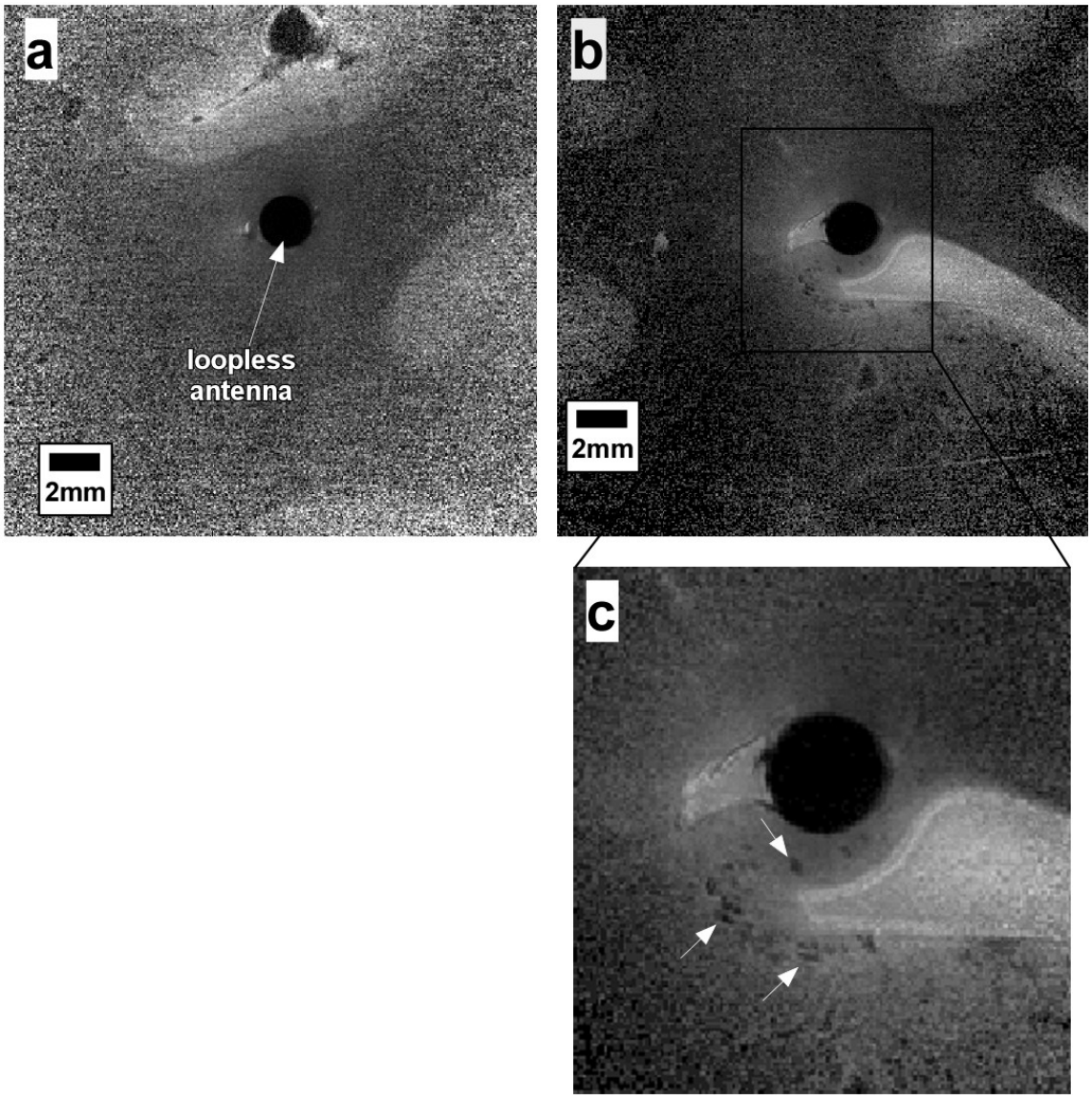


**Figure 6.5.** MRI of age-matched brain specimens (a) without and (b) with Alzheimer's disease (AD) pathology at 60µm in-plane resolution. (c) MRI of the brain with AD pathology is zoomed, and the arrows point to signal hypointensities that can potentially be senile plaques. The 2.2mm diameter loopless antenna appears as a dark circle inside the images.

## 6.4. Discussion

In this work, we investigated the performance of high-resolution imaging using a loopless antenna on brain specimens with and without AD pathology. Tiny, hypointense lesions were visible in the brain with AD pathology that were consistent with senile plaques, and such variations were not present in the MRIs of the specimen without the disease pathology. However, the MRI results must be compared with histology to confirm these findings.

The high-resolution scans ranged from 15 minutes to 1 hour, which may not be clinically practical. However, by optimizing the MRI pulse sequences and employing FOV reduction techniques [53, 191-194], it is conceivable that scan durations could be shortened to a few minutes to improve clinical practicality.

# Chapter 7.

# 7 Tesla MRI with a Transmit/Receive Loopless Antenna and $B_1$-Insensitive Selective Excitation

## 7.1. Introduction

As previously shown in Chapter 4, the practical achievable SNR of an interventional loopless antenna[8] increases quadratically with the main field, $B_0$ [51, 54]. At 7T this results in about a 6-fold SNR gain compared to 3T, while the usable FOV defined as the area enclosed by an equivalent SNR contour, increases about 10-fold. The higher SNR enabled imaging of human artery specimens with in-plane resolution as small as 40μm at 7T using a receive-only device and external excitation, as shown in Chapter 4. Nevertheless, 7T imaging of tissues deep inside the body with tiny MRI detectors is challenging due to the availability of suitable external transmit coils and their accompanying problems of RF-field ($B_1$) inhomogeneity [101, 195] and penetration, the potential for high local RF power deposition[59, 103, 151], and transmit/receive coil interactions[51].

Some of these issues are addressed by advances in parallel multi-channel transmission, and static or dynamic $B_1$-shimming [107, 112, 116, 196, 197]. However, optimization of the external $B_1$ transmission field is time consuming, untested in the presence of internal conducting devices, and potentially impractical for dynamic interventional procedures that involve a transiting internal probe. Problems specific to

external excitation for internal MRI detectors could be eliminated by using the internal probe for both transmit and receive, as recently demonstrated for prostate coils at 7T [198], and the loopless antenna at 3T [162]. We posit that at 7T, the gain in SNR and FOV for a transmit/receive loopless antenna could be large enough to provide enough range to avoid the need for external MRI coils altogether for intravascular applications. If so, the loopless antenna would need to serve for both scout and high-resolution MRI, and safety and a reasonably uniform RF excitation field, would be key.

Here we demonstrate scout and high-resolution imaging with a 7T internal transmit/receive loopless antenna employing composite, spatially-selective, $B_1$-insensitive excitation pulses[72]. RF safety is tested experimentally using a gel phantom. Scout and high-resolution 7T images from fruit and diseased human arteries *in vitro*, and first *in vivo* intravascular results from a rabbit aorta are presented.

## 7.2. Methods

### 7.2.1. RF Pulse and EM Simulations

Spatially selective composite pulses were designed using a Matlab based optimization algorithm[72]. The transverse magnetization at the end of the RF pulse was numerically computed by solving the Bloch equations for a ±3mm range with 0.1mm increments, and $B_1$ over 0-30μT with 0.1μT increments[199]. Signal loss due to spin-spin relaxation($T_2$) during the RF pulse[177] was numerically calculated for $T_2$=30ms, comparable to that in vessels[200]. Composite pulses consisting of 5 and 11 Gaussian-

modulated sub-pulses with total durations of 5.4 and 11.8ms respectively, were evaluated with various $B_1$ amplitudes and resonance offsets ($\Delta B_0$), and compared with a single Gaussian pulse.

The electro-magnetic(EM) field of a transmitting loopless antenna inside a homogeneous medium with conductivity $\sigma$=0.63Sm$^{-1}$ and dielectric constant $\varepsilon$=80 (equivalent to 3.5gL$^{-1}$ saline) was numerically computed using FEKO analysis software (FEKO Inc., Stellenbosch, South Africa), as described previously[51]. The loopless antenna was modeled as a quarter wavelength ($\lambda$/4=17cm) 2.2mm diameter coaxial cable with the inner conductor extended by 33mm to form a resonant whip. The antenna was excited by a 298MHz, 1A current source placed at the cable-whip junction[51, 54]. Conducting surfaces were modeled as perfect electric conductors. The EM-field distribution was computed in coronal planes at 0.2mm intervals extending up to 20cm radially from the whip-cable junction, and 20cm parallel to the cable extending 8cm distal to the junction. The sampling resolution was 1.25x10$^{-4}$mL. The specific absorption rate (SAR) was computed at each point using:

$$SAR(x,y,z) = \frac{\sigma(E^2_{X(x,y,z)} + E^2_{Y(x,y,z)} + E^2_{Z(x,y,z)})}{2\rho} \quad \textbf{[7.1]}$$

where $\rho$ (kg.m$^{-3}$) is the density of the medium.

## 7.2.2. Experimental Devices

The experimental transmit/receive loopless antenna was fabricated from a $\lambda$/4=17cm UT-85C semi-rigid copper coaxial cable (Micro-coax, Inc., Pottstown, PA) with

a 33mm whip. Simulations showed that this geometry yielded results equivalent to a lossless cable[54]. The end of the cable was connected to an impedance matching circuit via a solenoidal balun to suppress common-mode currents on the cable shield, as in Figure 2.6 of Chapter 2, but with the diode and series capacitor removed. The tuned/matched antenna (loaded Q≈6) was interfaced to a Philips Achieva 7T MRI scanner (Philips Medical Systems, Cleveland, OH) using Philips' linear single-channel transmit/receive box.

A 7T biocompatible nitinol loopless antenna was fabricated for *in vivo* use from an obsolete 0.76mm diameter *Intercept* 1.5T guidewire (MRI Interventions Inc., Memphis, TN) by cutting the distal coaxial cable to 3λ/4 (54cm), and the whip to 6.1cm.

### 7.2.3. RF Safety Testing

RF safety was tested with the loopless antenna inside a 20-cm diameter, 20-cm long cylindrical saline phantom prepared with $15gL^{-1}$ polyacrylic acid to inhibit convection (higher viscosity but the same thermal conductivity as water). The electrical properties were matched to those simulated, by reducing the salt concentration to $0.8gL^{-1}$ to provide an antenna load equivalent to the $3.5gL^{-1}$ saline. A constant amplitude forward RF power of 300mW, at 298MHz and 100% duty cycle was applied to the device, and the temperature monitored with fiber-optic temperature sensors (Neoptix, Inc., Quebec, Canada) contacting the antenna at locations determined from the simulations to have the highest SAR (the cable-whip junction, tip, and insertion point). The temperature was sampled at 1Hz for at least 1min with the RF power turned-off,

and 15min with the RF power on.

### 7.2.4. MRI Performance

The performance of the 5-Gaussian composite pulse and a conventional selective excitation pulse at 7T were compared in the cylindrical phantom filled with 0.5g$L^{-1}$ $CuSO_4$-doped saline with the same loading as in the RF safety tests, and in a kiwi fruit. The RF power loss between the power amplifier and the coil interface was measured at 50%. Average power at the device was set to levels that ensured RF heating ≤2°C as determined from the RF safety experiments. Spin-lattice relaxation ($T_1$) weighted two-dimensional (2D) fast-field echo (FFE) sequences were used (repetition time, TR=200ms; echo time, TE=15ms; FOV=5x5$cm^2$; voxel-size=100x100$\mu m^2$; nominal slice thickness, 3.2mm). To verify slice selection, an 8-step phase-coding gradient was added to the slice selection gradient waveform with 0.8mm resolution (3D FFE; FOV=5x5x0.64$cm^3$). The applied forward power ($P_F$) was determined from the incident power($P_i$) at the proximal end of the antenna cable via:

$$P_f = P_i(1-\Gamma^2) \qquad \textbf{[7.2]}$$

where $\Gamma$ is the reflection coefficient measured using a network analyzer. A '20% useable' imaging FOV diameter was defined as that corresponding to 20% of the maximum received signal intensity outside the antenna. This was determined for forward peak pulse powers of 1-16W with all other imaging parameters held constant.

Large FOV MRI was tested with the antenna in a large pomelo fruit (multi-echo

$T_1$-weighted FFE; TR=200ms; TEs=7,17,27,37ms; FOV=12x12cm$^2$; voxel-size, 0.5x0.5mm$^2$; Peak $P_F$=58W; Average $P_F$=359mW; 2 averages; duration, 97s). An inhomogeneously-broadened $T_2$ ($T_2$*) image was calculated from the exponentially-fitted magnitude images acquired at the different TEs. Low- and high-resolution MRI was also performed on human iliac artery specimens obtained from our institution's autopsy service. Specimens were immersed in a (3.5gL$^{-1}$) saline bath, the loopless antenna inserted in the lumen, and $T_1$-weighted FFE sequences applied. Low-resolution coronal scout MRI (TR/TE=200/15ms; scan-time=49s; FOV=16x6cm$^2$, voxel-size=250x94µm$^2$; Average $P_F$, 99mW) was followed by rapid axial MRI of a region-of-interest (ROI; TR/TE=100/10; scan-time=10s; FOV=2x2cm$^2$; voxel-size=100x100µm$^2$; radial readout with 50% density; Average $P_F$=50mW), and/or high-resolution MRI (TR/TE=150/22ms; scan-time 151s; FOV=5x5cm$^2$; voxel-size=50x50µm$^2$; Average $P_F$=33mW). Nominal slice-thickness was 3.2mm.

*In vivo* studies approved by our Institutional Animal Care and Use Committee, were performed on healthy sedated New Zealand rabbits. The nitinol loopless antenna was inserted into the ascending aorta via the femoral artery and a 5-French introducer, under X-ray guidance. The animal was moved to the 7T scanner and coronal scout MRI performed using the transmit/receive antenna, followed by axial 2D FFE MRI with 8W applied forward peak power at the antenna input. Images were cardiac-gated with TR at the heart-rate (HR). Larger FOV axial MRI was performed (TR=0.2-0.3s; TE=6ms; FOV=6-9cm; voxel size=300-500µm; 3-4mm slices; scan duration=1-2min, $P_F$=8-32W), followed

by higher resolution 100-200µm MRI (TR=0.35-0.46s; TE=7-10ms; FOV=3cm; scan duration=140-152s; $P_F$=8W).

## 7.3. Results

### 7.3.1. Simulations

The computed amplitude, phase, and gradient waveforms of the 5-Gaussian composite pulse are shown in Figure 7.1.a. With a peak power of 4W, the $B_1$ amplitude falls from 8µT at 1cm to 2.0µT at 3cm. This pulse excites ≥50% of $M_0$ for $1.5 \leq B_1 \leq 32$ µT corresponding to a 6.2cm diameter excitation disk (Figure 7.1.e). By comparison, a single Gaussian-modulated pulse excites ≥50% of $M_0$ over $5.6 \leq B_1 \leq 27.0$µT, yielding only a 2.7cm diameter 50%-excitation disk (Figure 7.1.f). Increasing the applied power of the single Gaussian pulse does extend its FOV, but produces dark rings at multiples of 180° FA close to the antenna where receiver sensitivity is greatest. Thus, the lower $B_1$ excitation threshold of the composite pulse more than doubles the diameter (or quadruples the area) of the MRI excitation volume compared to applying a single pulse with the loopless antenna transmitter.

Signal loss with $T_2$=30ms at the end of the 5-Gaussian composite pulse is 10% (Figure 7.1.c) vs. 2% for the single Gaussian pulse (Figure 7.1.d). While an 11-Gaussian composite (not shown) excites more uniformly than the 5-Gaussian pulse, its $T_2$ losses increase to 19%. We therefore chose the 5.4ms-long 5-Gaussian pulse as an acceptable compromise between uniformity and $T_2$ loss. Its full-width half-maximum slice-thickness

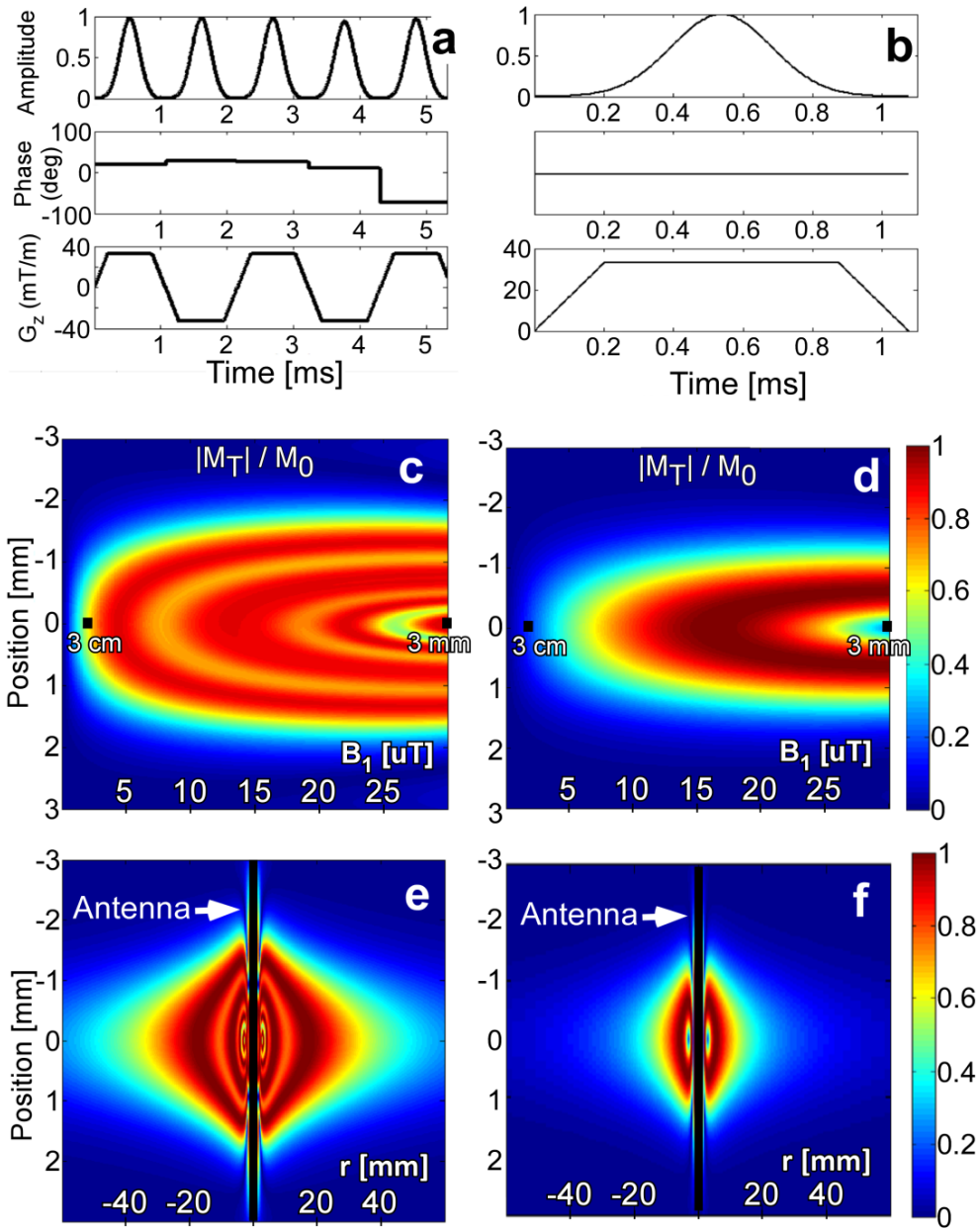


**Figure 7.1.** (a) Along the first row, B1 amplitude, B1 phase and gradient amplitude waveforms for the 5-Gaussian composite pulse, and (b) a conventional single-lobe Gaussian pulse are shown. The second row shows the transverse magnetization at the end of: (c) the 5-Gaussian composite, and (d) a single Gaussian pulse for 0≤B1≤30μT and T2=30ms. The B1 at 3mm and at 3cm from the antenna junction are annotated. The third row shows the transverse magnetization as a function of axial position (r) for the (e) 5-Gaussian (f) single-Gaussian pulses ±6cm from the antenna. The applied peak pulse power was 4W throughout.

is 3.2mm on-resonance at a radial distance r=7mm from the antenna, decreasing to 2.9mm and 2.0mm at r=1 and 3cm respectively. Off-resonance ($\Delta B_0$ =-200/+350Hz), slice-thickness is 2.3mm at r=1cm and 2mm at r=3cm. As usual, slice-thickness can be adjusted by changing the gradient amplitude or pulse length. Here, hardware constrained the maximum gradient strength to 33mT/m, but thinner slices (<3mm) could be obtained by increasing the length of sub-pulses.

### 7.3.2. RF Safety Testing

The numerically computed SAR distribution and temperature probe placements are shown in Figure 7.2.a. The temperature rise at an applied average $P_F$=300mW did not exceed 1°C during 15min of continuous RF excitation (Figure 7.2.b). The highest temperature rise occurred at the cable-whip junction with the tip and insertion points heating less, consistent with the EM simulations (Figure 7.2.a). Thus, operation with ≤1°C local temperature rise is achievable with average power levels of <300mW. This translates to minimum TRs of 8.2, 16.5 and 66ms with peak applied RF pulse $P_F$ levels of 2, 4 and 16W, respectively.

### 7.3.3. MRI Performance

Axial images from a kiwi fruit with the transmit/receive loopless antenna using a two-lobe conventional sinc-pulse, and the 5-Gaussian composite pulse, are shown in Figure 7.3. With the sinc-pulse, the image is degraded by dark ring artifacts at 180° FA multiples (Figure 7.3.a) that are not present in the image acquired with the 5-Gaussian

pulse (Figure 7.3.b). The coronal image in Figure 7.3.c is annotated to show the location of axial 0.8mm slices of the 3D FFE experiment to demonstrate the spatial selectivity of the composite pulse. As shown in Figure 7.3.d, only the middle 4 slices of the 3D set exhibit signal, consistent with the nominal 3.2mm slice thickness.

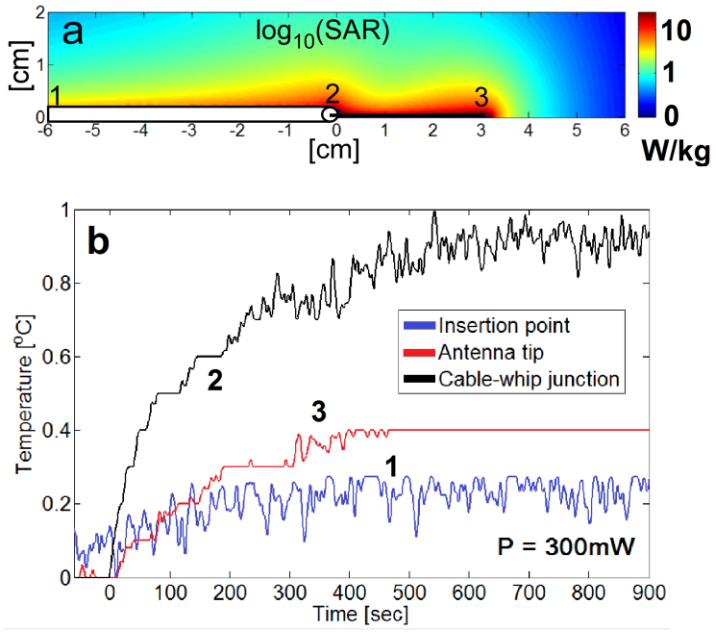


**Figure 7.2.** (a) Computed relative SAR (logarithmic scale) annotated to show temperature probe placement in the safety studies. (b) Temperature rise during a 15 min RF exposure at a continuous input power of 300 mW, as measured at the insertion point (blue, 1), cable-whip junction (black, 2), and tip (red, 3).

Without a global view provided by an external coil, to select an image plane one must first find the antenna in a large FOV scan. Figure 7.4.a shows '20% useable' FOV diameters of 48, 62 and 98mm at peak $P_F$'s of 1, 4 and 16W, respectively. At 58W, an entire 10.5cm pomelo is excited (Figure 7.4.b). The dark lines in the computed $T_2$* image (Figure 7.4.c) are membranes separating juice compartments whose uniform depiction demonstrates that the composite pulse is robust to $T_2$ losses across the entire FOV.

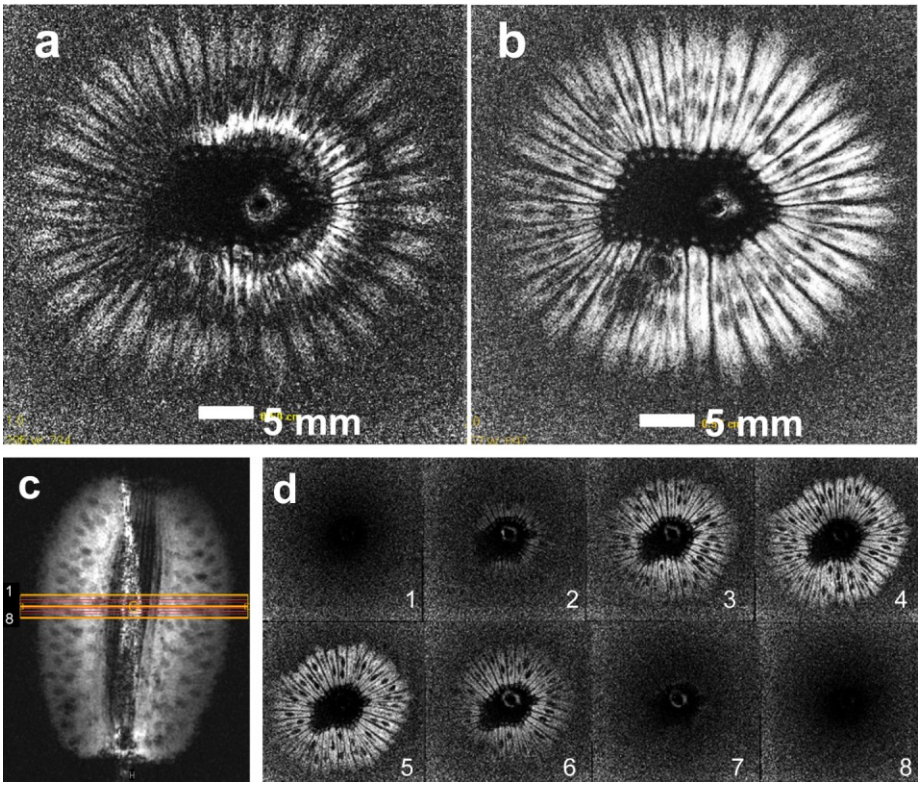


**Figure 7.3.** (a) Axial images acquired with a transmit/receive loopless antenna using a conventional sinc-modulated pulse, and (b) using the 5-Gaussian composite pulse ($T_1$-weighted 2D FFE; TR/TE=200/15ms; FOV=5x5 cm2; voxel-size=100x100μm$^2$; nominal slice thickness, 3.2 mm). (c) Coronal image annotated with orange grid to show the planning of the 3D experiment to demonstrate slice selectivity (T1-weighted 2D FFE; TR/TE=200/15 ms; FOV=5x5cm$^2$; voxel-size=100x100μm$^2$; nominal slice thickness, 3.2mm). (d) Axial 0.8mm thick images from the 3D experiment show signal in 4 slices consistent with the 3.2mm slice thickness (3D FFE; FOV=5x5x0.64cm$^3$).

For *in vitro* and *in vivo* intravascular studies, the global view is afforded by a fast, low-resolution, coronal scan which is brightest around the antenna with an FOV that again increases with $P_F$ (Figure 7.5.a). After locating an ROI on the coronal scan, rapid 100μm axial MRI (Figure 7.5.b) or slower (Figure 7.5.c) higher resolution (50μm) MRI can be performed at reduced power levels and FOV. In vessel specimens *in vitro*, these show a lesion and plaque components including a fibrous cap (annotated). The signal loss in

the biocompatible 3λ/4 nitinol cable used for *in vivo* studies (Figure 7.5.d) was 21% (Insertion loss=2dB) compared to the 'lossless' copper cable used *in vitro*. In an *in vivo* rabbit study using the same MRI protocol but with cardiac-gating, the ~3mm diameter aorta and anatomy is depicted at 300μm resolution with large FOV (Figure 7.5.e), and at 100μm resolution with reduced FOV MRI (Figure 7.5.f).

## 7.4. Discussion

In this chapter, we investigated the feasibility of 7T MRI with an internal transmit/receive loopless antenna and no external coils. RF power requirements, $B_1$-field inhomogeneity, and local SAR are a challenge at 7T. For studies involving internal conductors and/or active MRI detectors, potential coupling with an external transmitted field and dealing with $B_1$-variations if the conductor/detector is moved, represent additional complexities. These on top of an already complicated environment and workflow make interventional MRI at 7T a dubious if not daunting prospect. Nevertheless, the dramatically improved SNR, at least for the loopless antenna, offers an unprecedented high-resolution imaging opportunity that is presently not practical at lower fields[51], or even at 7T with the external detectors developed to date.

Compared to the use of internal loop coils for prostate MRI at 7T[114-116, 198, 201], the sub-millimeter dimensions possible with the loopless antenna enable targeted intravascular access under image guidance[202-204], that is not possible with larger internal coils. Indeed the 50-100μm resolution achieved here *in vitro* and/or *in vivo* are smaller

than the best resolution achieved to date at 7T of 0.5x0.5mm$^2$, using prostate coils with similar slice-thickness[116]. However, prostate coils have already been used in humans at 7T, while the loopless antenna has so far only been used in patients at 1.5T[202] and the best resolution achieved at 1.5T was only ~160µm[8, 54].

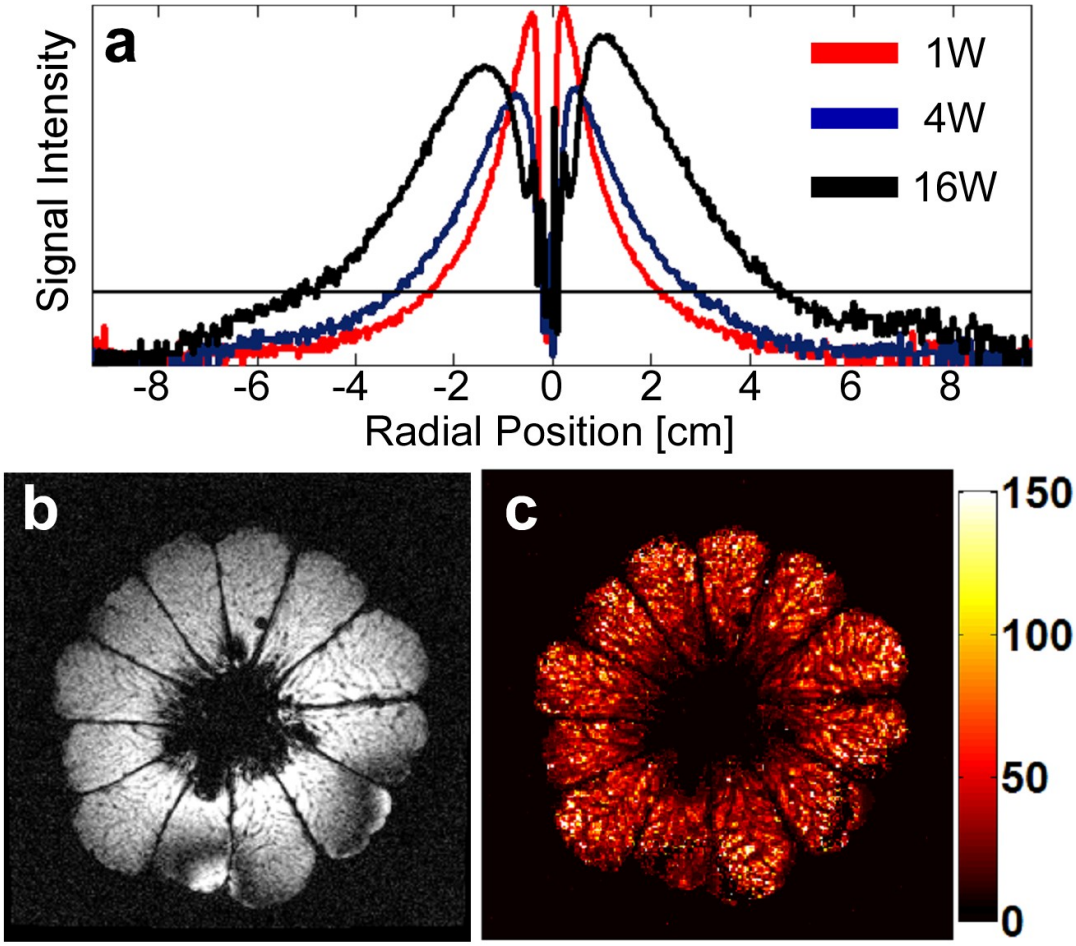


**Figure 7.4.** (a) Signal intensity profiles acquired inside a homogeneous phantom with identical imaging parameters at 1, 4, and 16W (red, blue, and black respectively) of applied peak forward power (PF) are shown. The horizontal line indicates the thresholding level for determining the '20% useable' imaging FOV, which is 48.4, 61.5, and 98.3mm for 1, 4, and 16W of applied peak PF respectively. (b) Large FOV axial (TE=7ms) 2D image acquired inside a pomelo fruit, and (c) $T_2$* map calculated using the magnitude images acquired at different TEs (multi-echo T1-weighted FFE; TR=200ms; echo-times TE=7, 17, 27, 37 ms; FOV=12x12cm$^2$; voxel-size, 0.5x0.5mm$^2$; Peak applied PF, 58W; Average PF, 359mW; 2 averages; duration, 97s; color scale in ms at right).

The primary limitation that we encountered in using the composite pulse was its 90° FA, which limited short-TR Ernst-angle acquisitions and SNR efficiency even while providing the best $B_1$ performance in simulations (Figure 7.1). This resulted in scan-times of ~2 minutes for high-resolution (≤100µm) *in vivo* studies using conventional cardiac-gated 2D FFE imaging. While cardiac-gating was effective in ameliorating motion artifacts, we had previously achieved 80-300µm resolution at up to 1-2 frames/s *in vivo* at 3T using steady-state free-precession (SSFP) sequences[163]. Thus, scan efficiency in future applications of the composite pulse at 7T could benefit from a reduced FA in combination with SSFP approaches.

Using the loopless antenna for both transmit and receive, eliminates both coupling issues and the need for $B_1$-shimming, because the $B_1$-field follows the probe during the procedure. While this is analogous to MRI endoscopy[162], the present approach differs in that MRI endoscopy employs no slice selection and its profile is fixed. However, like MRI endoscopy, the transmit/receive antenna can be excited with a few Watts of peak RF power, and peak local heating can be kept within safe levels, even <1°C (Figure 7.2), by setting input power and TR. The maximum or peak local temperature rise must be calibrated against the power delivered to the coil to ensure safe operation.

Because $B_1$ decays rapidly with radial distance from the antenna, the use of conventional slice-selective pulses results in artifacts at 180° multiples when the

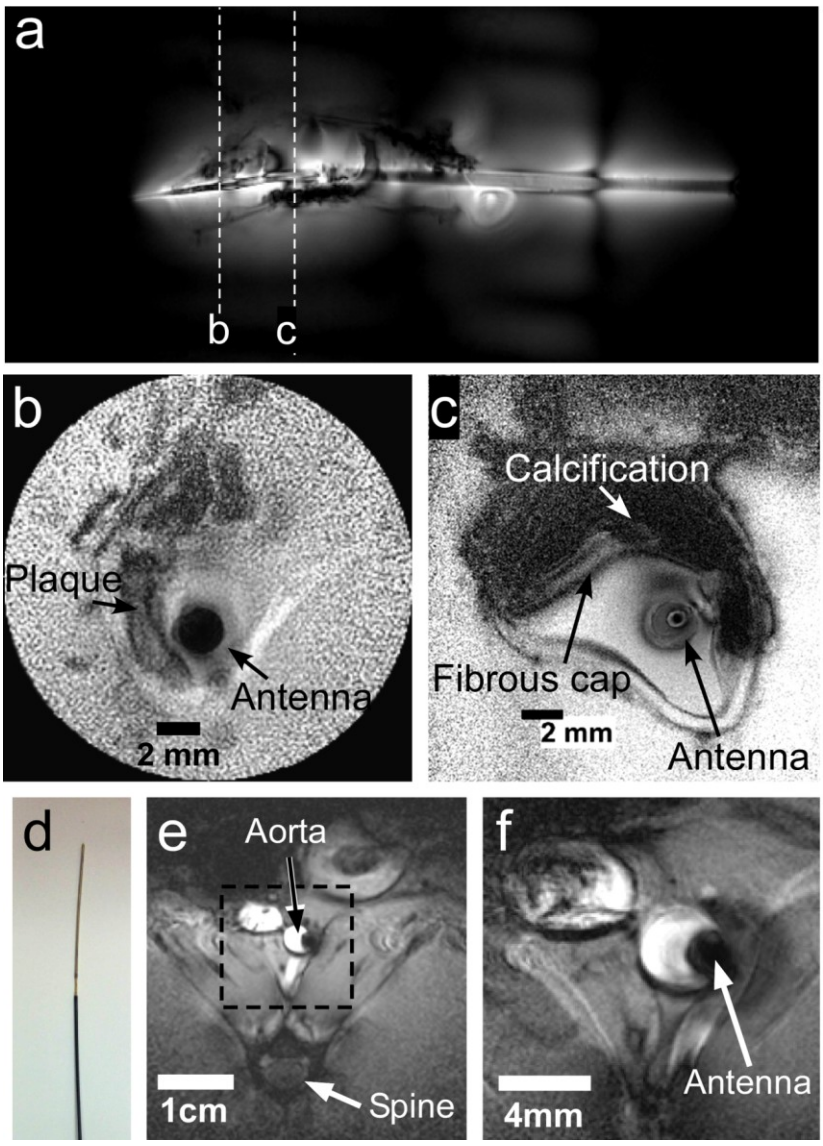


**Figure 7.5.** (a) Large-FOV intravascular coronal scout image of a diseased human iliac vessel in a saline tank annotated to show sections imaged in parts (b) and (c) ($T_1$-weighted FFE; TR/TE=200/15 ms; duration=49s; FOV=16x6cm$^2$; voxel-size=250x94 µm2). (b, c) Annotated high-resolution trans-axial images through the vessel wall (b: TR/TE=100/10ms; duration=10s; FOV=2x2cm$^2$; voxel size=100x100µm$^2$; radial readout with 50% density. c: TR/TE=150/22ms; duration=151s; FOV=5x5cm$^2$; voxel-size =50x50µm$^2$). (d) Photograph of the distal end of the 0.86mm diameter 7T biocompatible nitinol loopless antenna. (e) Large-FOV in vivo axial image through the aorta of a healthy rabbit (TR/TE=231/5.9ms; duration=70s; FOV=9x9cm$^2$; voxel-size=300x300µm$^2$; slice thickness=4mm; Bandwidth=154KHz; Pi=64W). (f). In vivo 100µm image of the annotated region from part (e) (TR/TE=462/9.8ms; duration=140s; FOV=3x3cm$^2$; voxel-size=100x100µm$^2$; slice thickness=4mm; BW=52KHz; Pi=16W).

antenna is used for excitation. Conversely, the use of spatially-selective $B_1$-insensitive composite RF pulses excited up to ~10 cm diameter volumes, without significant artifacts (Figure 7.4). While the excitation profile could be further optimized by increasing the number of sub-pulses or changing the modulation waveforms, there is a tradeoff between modifications that increase pulse length vs. signal loss due to $T_2$ decay.

Decreasing the excitation FOV with conventional 7T external coils[194, 205] is also challenging due to $B_1$ inhomogeneity and SAR restrictions. Without FOV reductions, scan-time may be prohibitive for sub-100µm 7T MRI, regardless of SNR. A transmit/receive internal antenna whose FOV can be varied simply by adjusting the pulse power, offers considerable versatility for interactively adjusting scan-time and spatial resolution. Large-FOV, low-resolution scout MRI performed in a high-power mode can be enjoyed for locating both device and target, and guiding one to the other. After locating an ROI, the operator can switch to a low-power navigation mode, shrinking the imaging FOV. Not only does lower power permit shorter TRs, but scan-time can be further reduced because fewer K-space lines or phase-encoding steps are required for the smaller FOV. Finally, at a target site of intervention or suspect lesion, high-resolution MRI at a ~50µm level is possible (Figure 7.5), where the FOV could be further reduced to increase speed. At this resolution it might be possible to measure fibrous cap thickness in vulnerable atherosclerotic lesions [206], or perhaps senile plaques in ageing brain [207].

# Chapter 8.

# Monitoring Local Heating Around an Interventional Loopless Antenna Using RF Radiometry

## 8.1. Introduction

Microwave radiometry is the science of measuring the emission of electromagnetic (EM) radiation from lossy materials at microwave and RF frequencies. The relationship between the EM emissions and the absolute temperature, first noted in the 1920's [208, 209], led to the routine use of radiometry for environmental and astronomical applications based on noise-power measurements with focused antennae operating in the gigahertz range [210].

Radiometry is a passive detection method that uses no applied radiation in any form, and therefore presents no radiation hazard. It has been applied to measure temperature increases in biological tissue including those associated with fast-growing breast tumors using external antennae [211, 212] and in human carotid atherosclerotic plaques using microwave antennae[213]. Previously, a radiometer concept that operates at low radio frequency (RF) of a 1.5 Tesla (T) magnetic resonance imaging (MRI) scanner using an external loop coil was introduced [214].

Interventional MRI (iMRI) employing active small-diameter catheters, guidewires, needles etc, as MRI detectors, is an application of MRI technology that poses potential safety risks of due to RF heating in the vicinity of the conducting

elements [65, 215-217]. This is compounded when the internal device is used for both MRI transmission and reception in intravascular applications [53, 162], and at ultra-high magnetic field strengths ($B_0$>3T)[53, 116] where MRI access to deep tissue may be limiting [101, 103, 151]. If the MRI device is further used for targeted thermal therapy delivery, for example, to enhance gene therapy[218], for RF ablation as a treatment for cardiac arrhythmias [219], or for tumor ablation[220], then having an independent means of temperature monitoring for assessing safety and thermal dose in real-time, is critical.

Fiber-optic temperature probes offer probably the best option for packaging with an MRI device and avoiding the confounding effects of an extra RF conductor[54]. However, their local sensitivity is limited to a few mg of tissue[55] so that precise placement is critical. Also, although fiber diameters are small, their size may still limit interventional applications (such as catheter deployment over an MRI guidewire) in tight vessels if they have to be added to an existing device. Clearly, there would be more space if the MRI device could independently monitor temperature without adding any other thermal sensor.

Of all the MRI devices in use, the loopless antenna, formed simply from a coaxial line whose center conductor is extended approximately a ¼-wavelength (λ/4), is ideal as an imaging guidewire in narrow vessels and offers spatial resolution of 80μm or better at 3-7T[51, 54, 162]. The losses in a loopless antenna are primarily attributable to the electric field (E-field) distribution in the tissue between the whip and the distal end of the cable [51, 54]. We therefore posit that, in addition to high-resolution MRI, a loopless antenna

could also provide radiometric measures of the local temperature distribution within its sensitive volume. In particular, for devices used for both transmission and reception, based on the Principle of Reciprocity[221], any heating caused during transmission will have the same spatial distribution as the antenna's radiometric thermal sensitivity profile, at least until thermal conductivity in the tissue kicks in.

In this work we report the development and testing of a super-heterodyne RF radiometer (receiver) for an interventional loopless MRI antenna [8] operating at a 3T MRI frequency (128MHz), for monitoring internal temperature in the vicinity of the antenna. Radiometry experiments were performed with the probe in a bio-analogous saline gel phantom in which the gel's temperature was increased uniformly, and also locally, wherein RF power was applied directly to the loopless antenna, to simulate its potential application to monitor thermal dose in ablation studies. The radiometer's experimental performance was compared with numerical computations of spatial distribution of its power sensitivity with the effects of thermal diffusion included, and with results from MRI thermometry studies. We determined the conversion factors for computing the local peak 1g-averaged temperature rise (ΔT) near the loopless antenna based on radiometric temperature readings.

## 8.2. Theory

A lossy medium at an absolute temperature $T$ (Kelvin) emits electromagnetic radiation according to Planck's radiation law:

$$P_n = \frac{\left\langle V_n^2 \right\rangle}{4R} = kTB \qquad \textbf{[8.1]}$$

Here $P_n$ is the available noise power; $\left\langle V_n^2 \right\rangle$ is the variance of the thermal (open-circuit) noise voltage; $R$ is the real part of the equivalent resistance of the medium; $k$ is Boltzmann's constant; and $B$ is the bandwidth of the receiver. Eq. [8.1] enables absolute temperature of a medium to be estimated from the average noise power measured by a radiometer comprised of a receiving antenna, high-gain receiver electronics and a voltage or power measuring device.

The signal reported by the RF radiometer ($S_{radi}$) is proportional to the sensitivity-weighted volume integral of the temperature inside the medium [222, 223]:

$$S_{radio} \sim \frac{\int_V T(r)\sigma(r)\left|E(r)\right|^2 dr}{\int_V \sigma(r)\left|E(r)\right|^2 dr} \qquad \textbf{[8.2]}$$

Here $r$ denotes the spatial coordinates; $\sigma$ is the electrical conductivity of the medium which may vary both spatially and with temperature; and $E$ is the electric field (E-field) distribution of the antenna for unit current excitation. The antenna power receiving pattern ($P_d$) inside the medium is given by:

$$P_d(r) = \sigma(r)\left|E(r)\right|^2 \qquad \textbf{[8.3]}$$

For a loopless antenna, the sensitivity is highest near the cable-whip junction and the conductor, decaying rapidly with radial distance from the device [53]. Therefore, the radiometric temperature measured by the loopless antenna is expected to be most

sensitive to temperature changes at locations with high $P_d$ that lie nearest the cable-whip junction. We introduce a 'H-factor', $H(r)$, defined as the coefficient relating the local ΔT at an arbitrary location to the measured radiometric temperature rise, $\Delta T_{radiometer}$. If the H-factor at a certain location is known, then the actual temperature rise, $\Delta T_a(r)$, at that location can be determined from the radiometer reading via:

$$\Delta T_a(r) = \Delta T_{radiometer} H(r) \qquad \textbf{[8.4]}$$

The H-factor can be computed from the spatial distribution ΔT ($\Delta T_m$), and $P_d$ as follows:

$$H(r) = \Delta T_m(r) \frac{\int_V P_d(r) dr}{\int_V \Delta T_m(r) P_d(r) dr} \qquad \textbf{[8.5]}$$

where the integration is performed over the entire volume of the medium. We define the peak H-factor, $H_{peak}$, as the H-factor coefficient where the highest ΔT occurs. $H_{peak}$ can be used as a metric for determining the maximum expected temperature rise inside the medium based on a radiometry measurement. It is worth noting that the temporal (time, t) thermal response generally must also be considered. We characterize $H(r,t)$ using numerically computed $P_d$ and $\Delta T_m$ distributions, and compare the results with experimental data.

## 8.3. Methods

### 8.3.1. Loopless Antenna and the Experimental Phantom

An experimental loopless antenna was fabricated from a λ/4 (40cm) 2.2mm diameter UT-85C semi-rigid coaxial cable (Micro-coax, Inc., Pottstown, PA) with the inner conductor extended by 3.9cm to form a resonant whip at the 3T MRI frequency (128MHz) [51]. The end of the antenna cable was connected to the front-end of the radiometry receiver via a cable with two bazooka baluns tuned to 128 MHz [123].

An experimental phantom was built from two concentric cylindrical chambers that were sealed from each other. A 20cm long inner chamber having a diameter of 12cm was placed at the iso-center of a cylindrical outer chamber (Figure 8.1). The inner chamber was filled with uniform gel solution (15g/L polyacrylic acid, 0.8g/L salt) whose electrical properties matched those used in numerical simulations (dielectric constant ε=80, electrical conductivity σ=0.6S/m) and were comparable to those of biological tissue [53]. The loopless antenna was inserted inside the inner chamber of the phantom to a depth of 10cm, and connected to the radiometry RF receive chain (Figure 8.1).

The outer chamber of the phantom was filled with water and connected to a temperature-controlled water pump (VWR International LLC, Radnor, PA). Hot water was circulated inside the outer chamber of the phantom to uniformly heat the gel in the phantom's inner chamber (Figure 8.1). The phantom and the loopless antenna were placed inside an RF shielded room (measured shielding factor >100dB at the frequencies

of interest) to minimize external RF interference. The water pump was located outside the room and water was conveyed to the phantom through hoses passed through the room's waveguides. The temperature inside the gel was independently monitored at 1Hz using fiber-optic temperature sensors (Neoptix Inc., Quebec, Canada) placed at the cable-whip junction of the antenna and at other reference positions. These were used to verify temperature distributions and thermal equilibrium. The temperature sensors had a diameter of 1.6mm and their sensitive volumes were assumed to occupy a cube with dimensions of ($1.6mm^3$, 4.1mg of gel weight).

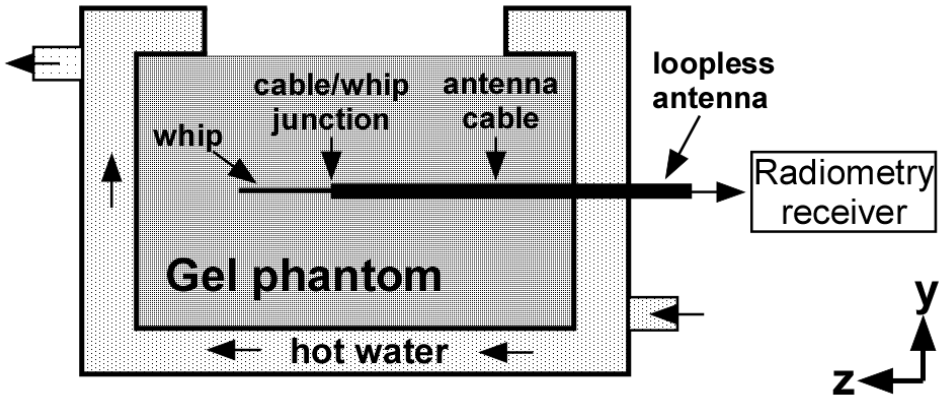


**Figure 8.1.** Side-view of the cylindrical experimental phantom and the placement of the loopless antenna inside the gel.

## 8.3.2. The Radiometry Receiver

A super-heterodyne receiver tuned to 128MHz with a bandwidth of 410KHz was designed and built for the radiometric measurements (Figure 8.2). The front-end of the receiver had two MRI transmit/receive (T/R) switches. The distal T/R switch was used to switch between radiometry for measuring temperature, and an RF power transmission

mode for local heating or ablation of the gel by the antenna, during which time the sensitive receiver electronics must be protected.

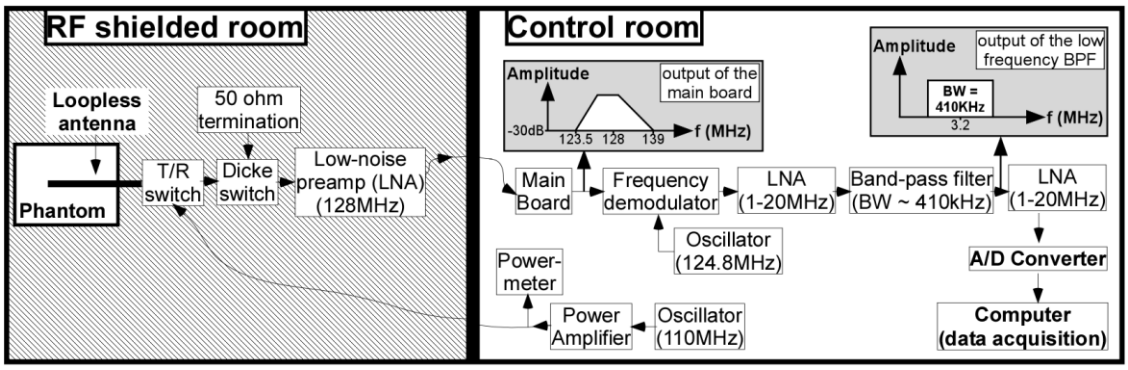


**Figure 8.2.** Block diagram of the radiometry receiver components. The phantom with the loopless antenna, front-end switches and the first preamplifier stage are placed inside the RF shielded room. The rest of the RF receiver components and the RF power delivery components are located outside the shielded room.

The second switch is a Dicke switch, placed between the first T/R switch and the receiver electronics. The third port of the Dicke switch is terminated with a 50Ω load that is kept at a constant temperature for calibrating the radiometer's receiver gain. The main purpose of the Dicke switch is to transition between the loopless antenna and the 50Ω load to acquire either radiometry data or calibration data [224]. During the RF power transmission mode, the Dicke switch provides additional protection for the receiver electronics (Figure 8.3). For bench testing outside of the MRI scanner, we substituted two 12V relays (OMRON, Kyoto, Japan) with >60dB isolation at 128MHz, for the T/R switches. The Dicke switch is connected to a low-noise preamplifier (LNA) (Wantcom Inc., Chanhassen, MN, Gain=28dB; noise figure, NF=0.4dB) and the signal from the LNA conveyed outside the room via a long coaxial cable incorporating several solenoidal and bazooka baluns that maintain signal integrity and minimize interference.

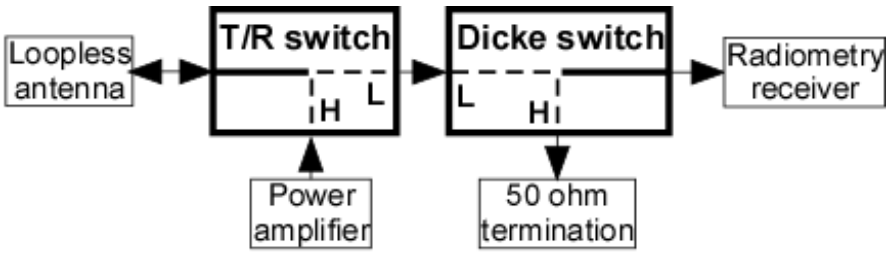


| State | T/R Switch | Dicke Switch | Power Amp |
|---|---|---|---|
| Radiometry (antenna) | L | L | Off |
| Calibration (50Ω) | H | H | Off |
| Local heating (amplifier) | H | H | On |

**Figure 8.3.** Radiometry front-end switches enable transition between the three possible states during the experiments.

The remaining receiver electronics is kept in a monitoring room (outside the RF shield). This includes a 'main board' housing three further LNA stages, and an anti-aliasing band-pass filter (BPF) tuned to 128MHz to restrict the noise bandwidth prior to demodulation (Figure 8.4). The BPF consists of two $14^{th}$-order 'hourglass' high-pass, and a $12^{th}$-order hourglass low-pass filter stages, designed using *Filter Solutions* software (Nuhertz Technologies LLC, Phoenix, AZ). The BPF provides >35dB attenuation for frequencies <123MHz to eliminate potential signal interference from sidebands that could wrap into the bandwidth of interest (127.7-128.3MHz) after demodulation. The filtered output signal from the main board (Figure 8.2) is down-converted to 3.2MHz with a quadrature demodulator (Polyphase Microwave Inc., Bloomington, IN) fed by a 124.8MHz local oscillator signal provided by a frequency synthesizer (Programmed Test Sources Inc., Littleton, MA).

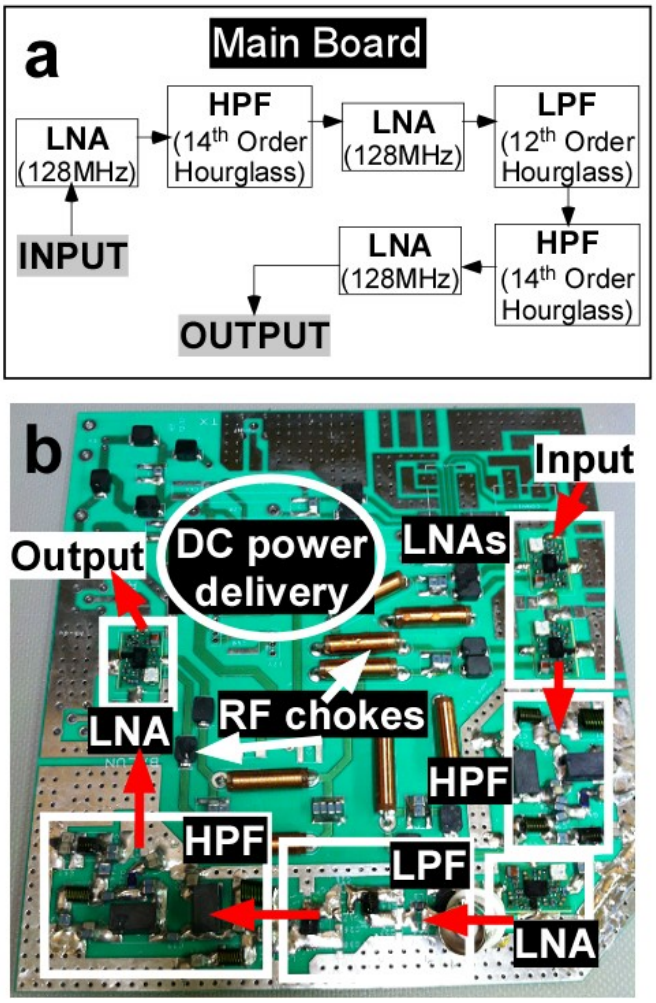


**Figure 8.4.** (a) RF components in the main board include three stages of preamplifiers and an anti-aliasing band-pass filter consisting of a low-pass and two high-pass filtering stages. (b) Photo of the main board is shown with different RF stages annotated.

The 3.2 MHz base-band signal is further boosted by two 20dB preamplifiers (Advanced Receiver Research, Burlington, CT; NF=2.5dB) and filtered with lumped element BPFs designed using the *Filter Solutions* software. The BPFs are tuned to 3.2MHz with bandwidths varying from 410-900KHz. The signal output of the RF receiver chain (Figure 8.2) is connected to a DT9832A, Data Translation Inc. (Marlboro, MA) data

acquisition module (DAQ) for analog-to-digital conversion, sampled at a 2MHz sample rate. Although the radiometry signal is above the Nyquist sampling limit, it is not attenuated by the DAQ whose 3dB bandwidth is >10MHz. The DAQ is connected via USB to a 2.67GHz dual-core laptop computer (8GB working memory), and the signals processed using Matlab (Mathworks Inc., Natick, MA).

Radiometry data were acquired continuously for 5s, followed by a 5s pause during which the data were stored and the average noise power determined at 0.5s intervals (10 readings/acquisition period) from the mean-square value of the acquired samples, using the Matlab timer function. Receiver gain calibration data was acquired at ≤1min intervals using the Dicke switch to switch between the 50Ω termination and the loopless antenna.

## 8.3.3. Experimental Setup

Calibration factors for converting noise power to temperature were determined from the average mean-square noise from entire 5s acquisitions in the uniformly-heated phantom experiments. The noise power measurements were corrected for system and gain variations based on contemporaneous Dicke-switched 50Ω load measurements, and compared to the Neoptix thermal sensor measurements as the standard. In the calibration experiment, the temperature of the gel phantom was increased uniformly from 25°C to 73°C and radiometry data acquired throughout. The radiometric temperature ($T_{radi c}$) was calculated from radiometer readings ($S_{radi}$) using:

$$T_{radio} = \psi S_{radio} + \beta \quad \textbf{[8.6]}$$

where the linear calibration factors $\psi$ and $\beta$ were determined by plotting the temperature measured by a Neoptix sensor placed at the junction (Figure 8.1) against $S_{radi}$.

After the radiometer was calibrated based on measurements with the phantom at thermal equilibrium, local heating was induced by exciting the antenna with RF power at 110MHz. The T/R and Dicke switches connected a continuous wave RF power amplifier (Tomco, Inc., BT00250, Stepney, SA, Australia) to the loopless antenna (Figure 8.1) with the 110MHz signal supplied by the frequency synthesizer. The amplitude of the output of the power amplifier was monitored with an RF power meter (LadyBug Technologies, Santa Rosa, CA). The power loss between the power amplifier and the loopless antenna was measured as 0.33dB (7.3%), using a network analyzer (4395A, Agilent Technologies, Santa Clara, CA). Intervals of radiometric measurement and RF exposure were interleaved, albeit with a 2s latency delay for radiometry after RF exposure ceased.

RF exposure was repeated with different power levels and durations according to Table 8.1. The radiometric temperature was determined using the calibration factors from Eq. [8.6]. The temperature readings from both the radiometer and the fiber-optic sensors reflecting temporal heating and cooling were empirically-fitted to smooth (double-exponential) curves. The experimental H-factors ($H_e$) at temperature sensor

locations experiencing temperature increases ΔT>2°C was determined from:

$$H_e = \frac{\Delta T_{sensor}}{\Delta T_{radiometer}} \quad \textbf{[8.7]}$$

**Table 8.1.** RF exposure parameters that were used during the radiometry experiment.

| **Exposure #** | **1** | **2** | **3** | **4** | **5** | **6** | **7** |
|---|---|---|---|---|---|---|---|
| **Average RF Power (W)** | 4 | 4 | 8 | 8 | 13 | 16 | 15 |
| **RF Duration (s)** | 123 | 119 | 60 | 35 | 31 | 19 | 57 |
| **Pause duration before the excitation (s)** | n/a | 342 | 377 | 217 | 180 | 223 | 138 |

## 8.3.4. MRI Thermometry

MRI thermometry experiments were conducted on a 20cm-long, 15cm diameter cylindrical gel phantom placed in the transmit/receive head coil of a Philips Achieva 3T scanner (Philips Healthcare, Cleveland, OH) using. The loopless antenna was inserted in the phantom to a depth of 10cm. The antenna's cable end was connected to the common port of a manual coaxial switch (CX210N, Diamond Antenna, San Marco, CA) with a slave port connected to a short to decouple the antenna during MRI excitation. The switch's other slave port was connected to the Tomco RF power amplifier set up outside the scanner room to provide RF power at 110MHz to induce local heating in the phantom. The applied power was monitored at the amplifier's output with the power meter, and the cable losses (=1.05dB, or 21.4%) measured with the network analyzer. MRI thermometry was interleaved with RF exposure with a ~5s latency delay for starting the MRI thermometry sequence after RF exposure ended.

A two-dimensional (2D) gradient-echo (GRE) sequence with repetition time/echo time (TR/TE) of 50/25ms was used to acquire MRI thermometry data. The field-of-view (FOV) was set to 12x12cm$^2$ with a 100x100 matrix size, and a coronal slice-thickness of 1.2mm (1mm below the antenna). The scan duration was 5s, repeated 60 times to generate a time-series dataset. The scanner's reconstructed phase images were used to calculate the temperature using the proton ($^1$H) resonance frequency (PRF) shift method [124]:

$$\Delta T_i = \frac{\phi_i - \phi_0}{\gamma \alpha B_0 TE} \quad . \qquad \textbf{[8.8]}$$

Here $\Delta T_i$ is the calculated temperature difference map, $\phi_i$ is the phase map at the i$^{th}$ time frame, $\phi_0$ is the reference phase map, $\gamma$ is the $^1$H gyro-magnetic ratio, $\alpha$ is the PRF change coefficient at $B_0$.

## 8.3.5. Determining the Thermal Conductivity of the Gel

In the phantom in the absence of perfusion, the bio-heat transfer equation (BHTE) [225] is:

$$\rho_t C_t \frac{\partial T(r,t)}{\partial t} = k_t \nabla^2 T(r,t) + P_d(r,t) \qquad \textbf{[8.9]}$$

where $\rho_t$ (kg/m$^3$) is the gel density, $C_t$ (J/g/K) is its thermal heat capacity, and $k_t$ (W/m/K) is the thermal conductivity. Eq. [8.9] assumes only thermal conduction and does not account for the presence of the loopless antenna. The local RF heating from the loopless antenna dissipates radially away from the source. Therefore, the thermal conductivity of the gel surrounding the loopless antenna can be calculated from the

spatial properties of the temperature distribution during thermal washout measured by MRI [226].

The thermal conductivity ($k_t$) of the gel was measured from 2D transverse MRI thermometry data acquired at the antenna's cable-whip junction 5, 10, 15, and 20s following RF exposure. The temperature images were fitted with 2D Gaussian distributions whose full-width half-maximum values (FWHMs) were squared and linearly fitted to obtain a slope, *m,* from which $k_t$ was derived via: [226]

$$k_t = \frac{4m}{\rho_t C_t} \quad \textbf{[8.10]}$$

The measured $k_t$ value was used for all numerical simulations of the temperature distribution around the loopless antenna.

## 8.3.6. Numerical Computations

EM field simulations were performed using full-wave method-of-moments analysis in FEKO software (FEKO Inc., Stellenbosch, South Africa). The loopless antenna was modeled the same as the experimental 2.2mm diameter cable with 39mm resonant whip at 128MHz. The model antenna was inserted 10cm into a uniform cylinder with σ=0.6S/m and ε=80, consistent with the phantom studies. A unit current source was placed at the distal end of the cable which was excited at 110 and 128MHz [51, 54]. The E-field distribution was computed on the coronal antenna plane at a 100μm in-plane resolution. The power sensitivity ( $P_d$ ) distribution was computed at each point using:

$$P_d(r) = \frac{\sigma(r)\left[E_x(r)^2 + E_y(r)^2 + E_z(r)^2\right]}{2\rho_t} \quad \textbf{[8.11]}$$

where $E_X$, $E_Y$, and $E_Z$ are the Cartesian E-field components. The $P_d$ distribution of the loopless antenna is circularly symmetric about the antenna's long axis. The 3-dimensional (3D) $P_d$ map was therefore calculated by rotating the 2D $P_d$ distribution about the antenna axis and re-gridding the result to a Cartesian coordinate system. The voxel-size along the z-axis was down-sampled to 400μm (voxel size: 0.1x0.1x0.4mm$^3$). The FOV of the 3D matrix centered at the antenna was cropped to 5x5x20cm$^3$ (matrix size: 501x501x501) to reduce the computation time.

The theoretical ΔT distribution inside the gel phantom at various RF exposures (accounting for RF power losses) was computed by solving Eq. [8.9] [225]. The gel parameters $\rho_t$, $C_t$, and $k_t$ were assumed to be spatially and temporally uniform inside the phantom, and constant over the temperature range studied. The gel's density ($\rho_t$ =1000kg/m$^3$) and heat capacity ($C_t$ =4.18J/g/K) were assumed to be the same as water, with the $k_t$ as measured above (Sec. 3.e). Ignoring the presence of the antenna, Eq. [8.9] was solved in the spatial frequency domain using: [227]

$$T^*(v,t) = T^*_{init}(v,t)e^{-\frac{4\pi^2 v^2 k_t t}{\rho_t C_t}} + \frac{P_d{}^*(v)}{4\pi^2 v^2 k_t}\left(1 - e^{-\frac{4\pi^2 v^2 k_t t}{\rho_t C_t}}\right) \quad \textbf{[8.12]}$$

where the asterisk denotes a Fourier Transform (FT) operation, $v$ denotes the coordinates in the spatial frequency domain, and the initial temperature distribution,

$T_{init}$, was set to zero. Taking the inverse FT of Eq. [8.12] yielded the ΔT distribution inside the phantom. The temperature distribution following RF exposure was calculated at 5s intervals for a 5-min cool-down period.

Three sets of temperature distributions were numerically computed for: (a) RF exposure parameters used in the MRI thermometry experiment; (b) RF exposure parameters used in the radiometry experiments (Table 8.1); and (c) a fixed 100s RF exposure of 4-16W (average), wherein the thermal conductivity of the medium was varied from 0.15-0.5W/m/K to mimic the human physiological range[228]. Because the RF heating was applied at 110MHz and the radiometer is operated at 128MHz, the ΔT distribution ($\Delta T_{110}$) was calculated from the $P_d$ distribution of the loopless antenna at 110MHz, and the radiometric ΔT ($\Delta T_{radio}$) was calculated from the $P_d$ distribution at 128MHz ($P_d^{128}$):

$$\Delta T_{radio} = \frac{\int_V \Delta T_{110}(r) P_d^{128}(r) dr}{\int_V P_d^{128}(r) dr} \quad \textbf{[8.13]}$$

Theoretical H-factors were calculated using:

$$H(r) = \frac{\Delta T_{110}(r)}{\Delta T_{radio}} \quad \textbf{[8.14]}$$

to compare with the experimental values. The numerically calculated H-factor map has a voxel size of 0.1x0.1x0.4mm$^3$ (4μg of gel). This was spatially averaged to increase the mass of each voxel to 4.1mg (1.6x1.6x1.6mm$^3$) to match the putative sensitivity volume

of the fiber-optic temperature sensors. The peak 1g-averaged H-factor (a regulatory metric) was calculated by averaging the values in a 1x1x1cm$^3$ cube centered at the whip 2mm away from the junction.

## 8.4. Results

### 8.4.1. Hardware

The 100-160 MHz frequency range is cluttered, which necessitated isolation of the radiometry measurements and the first LNA stage inside a RF-shielded room, analogous to those used for MRI. The main board and the rest of the receiver electronics were located outside the screened room to avoid feed-back. The NF and gain for the system was measured at the output of the second LNA as 0.40dB and 56dB, respectively. Overall gain of the receiver is between 105-110dB. The histogram of a 0.5s-long signal acquisition ($10^6$ samples), plotted in Figure 8.5, shows that the noise distribution is Gaussian, with a negligible mean value (-18mV).

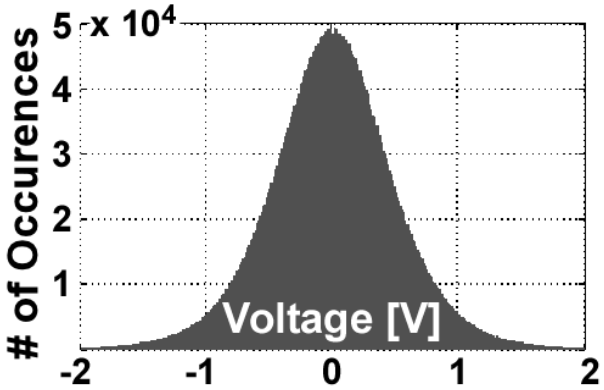


**Figure 8.5.** Histogram of the received samples over a 0.5s period shows a Gaussian distribution.

## 8.4.2. Calibration with a uniform temperature distribution

The raw radiometer readings were linearly proportional to the temperature measured at the sensor located at the cable-whip junction of the loopless antenna in the thermally equilibrated gel phantom, at least up to 73°C. The radiometer was calibrated at two different temperatures of 38°C and 73°C. The standard deviation (SD) of the radiometric temperature readings was ±0.24°C sampled at two measurements/second. The calibration factor factors $\psi$ and $\beta$ were dependent on the radiometer gain and/or load impedance.

Initially, we encountered a problem with temporal variations in the receiver gain, which introduced absolute errors of ±1°C during a 5 hour-long experiment. This necessitated introduction of the Dicke switch and re-scaling the calibration based on the noise power from the 50Ω termination connected by the Dicke switch (see Figs. 2, 3). However, with improvements to the RF chain including better cables and baluns, gain variations were reduced to ±0.3°C with, and ±0.4°C without re-scaling using the 50Ω calibration over a 90min run. Nevertheless, all reported radiometric temperature readings were cross-calibrated against the 50Ω load. Future improvements in power supply regulation could further improve accuracy.

The temperature of the gel inside the phantom was increased uniformly to 73°C by circulating hot water around the phantom, and the radiometer signal acquired continuously. After the 2-point calibration the radiometric temperature precisely

tracked the temperature sensor over the entire course of the experiment (Figure 8.6).

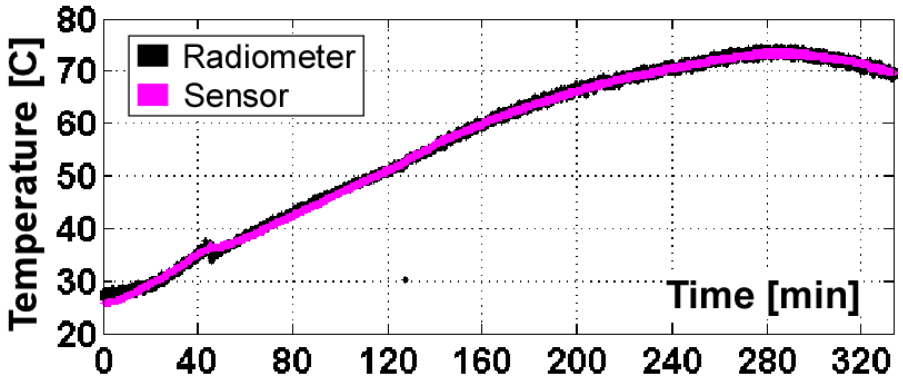


**Figure 8.6.** Linearly calibrated radiometric temperature readings follow the sensor values during the uniform heating experiment. The accuracy of the radiometric measurement is ±0.24°C.

## 8.4.3. Measuring the thermal conductivity of the gel

The Gaussian-fitted temperature profiles through the junction of the loopless antenna obtained from 2D MRI thermometry are shown during the cool-down period in Figure 8.7. A linear plot of the square of the FWHMs of the Gaussian curves (insert, top-left, Figure 8.7.b) yields $k_t$ =0.16W/m/K for the gel, from Eq. [8.10].

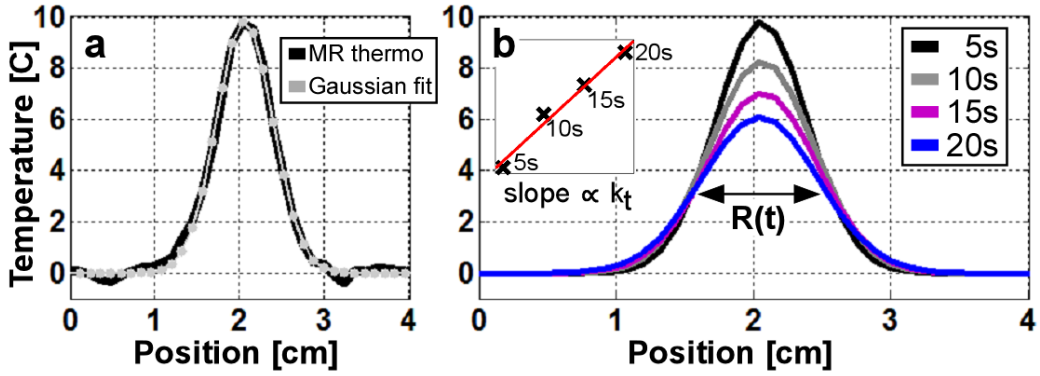


**Figure 8.7.** (a) Temperature profile intersecting the junction from the MRI thermometry data is fitted using a Gaussian curve. (b) Gaussian fits on the MRI thermometry data during the cool-down period between 5-20s. Radii of the Gaussian fits are squared and marked with symbol 'x' on the insert and fitted using a line plotted in red. Slope of the line-fit is proportional to the thermal conductivity ($k_t$) of the gel medium.

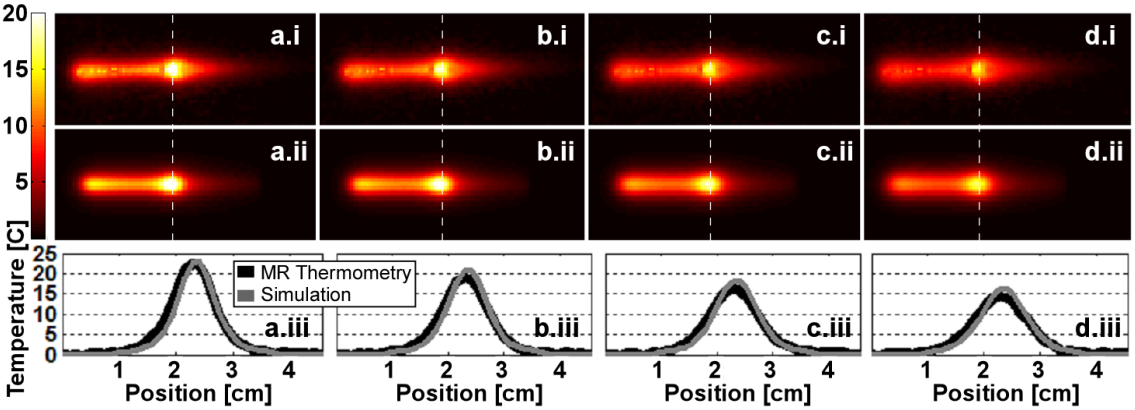


**Figure 8.8.** Along the first row (a-d.i) temperature rise distributions acquired using MRI thermometry and along the second row (a-d.ii) numerically computed temperature rise distributions are shown after 5, 10, 15 and 20s (columns a, b, c, and d; respectively) from the end of the RF exposure. On the third row, profiles of the temperature distributions annotated with dashed white lines are displayed in black for MRI thermometry and in gray for the simulations. Computed and measured peak temperatures are within 13% of each other.

### 8.4.4. MRI Thermometry and Numerically Computed Temperature Rise (ΔT)

The sensitivity of ΔT measured by 2D coronal MRI thermometry was ±0.25°C. The MRI temperature distributions at 5, 10, 15 and 20s following a 40s-long 16.5W RF exposure are shown in Figure 8.8, row I (columns a-d, respectively). The temperature distributions computed numerically assuming identical RF exposure conditions are shown in the second row (ii) of Figure 8.8. The temperature profiles along the white dashed lines in the images are plotted in the third row (Figure 8.8.iii). The difference between the measured and computed peak temperatures was <13%. The FWHM of the measured and computed temperature profiles also agree within 13% of each other. These results suggest that numerical computation can adequately predict the spatial

distribution of ΔT around a loopless antenna in a gel phantom. Heating primarily occurs along the whip, peaking at the cable-whip junction and decreasing along the cable.

### 8.4.5. Measuring peak temperature at the loopless antenna

Radiometric and fiber-optic temperature readings recorded at the junction during the radiometry experiment with local heating are shown in Figure 8.9(a). The radiometric temperature follows the sensors closely. The experimental H-factor relating the bulk temperature measured by the radiometer to the local temperature at the junction, is shown in Figure 8.9 (b). The reduction in H-factor with time reflects the increasing uniformity in the temperature distribution due to thermal diffusion and equilibration, as well as possible slight movements of the temperature sensor and the local gel medium due to thermal expansion and contraction as a result of extensive local heating.

A comparison of the computed and radiometric ΔTs is presented in Figure 8.10. The numerical computations track the measurements closely. The computed radiometric temperature predicted the peak ΔT with an average absolute error of 6.6%. The 14% error in estimating the peak temperature rise following the $7^{th}$ (final) RF exposure was due to an error in monitoring the average applied RF power during the exposure. Note also that the gel's thermal properties may vary locally with repeated heating and cooling that could affect the correlation between the radiometric and computed temperature. Therefore, only the first two RF exposures were used for the purpose of comparing simulated and experimental H-factors.

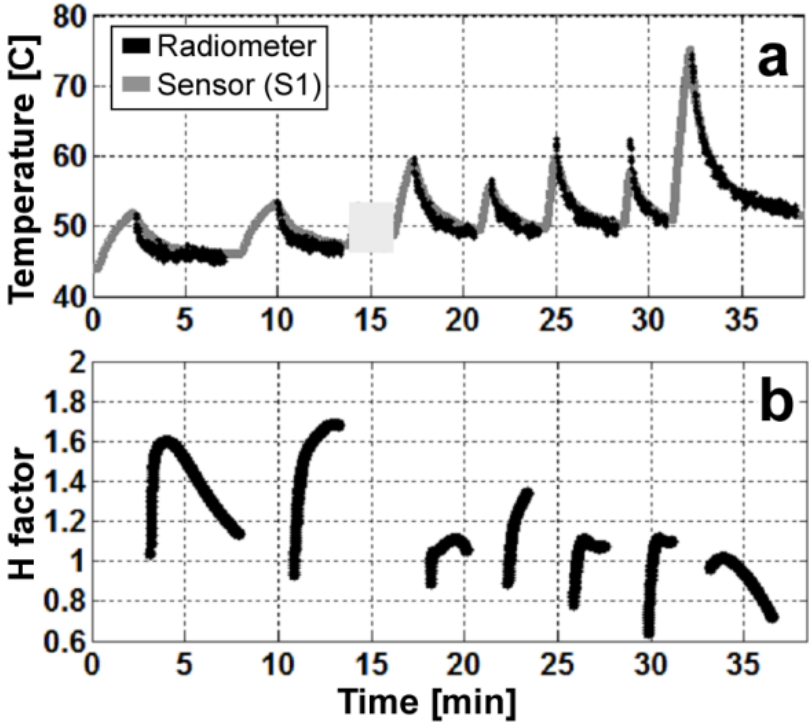


**Figure 8.9.** (a) Radiometric (black) and measured (gray) temperature values during the non-uniform temperature radiometry experiment are used to compute the (b) H-factor distribution. The measured H-factor at the sensor location (junction) is less than 1.7.

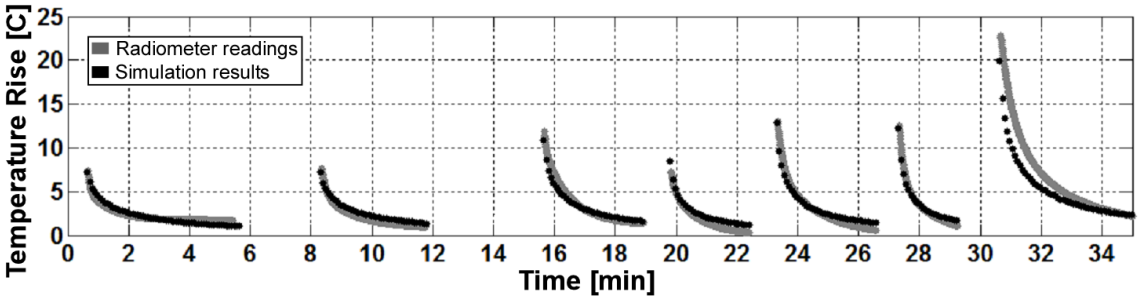


**Figure 8.10.** Experimentally measured (gray) and numerically computer (black) radiometric temperature rises are shown. The average absolute error in simulations is 6.6%.

Computed and measured ΔT values for the 4.1mg-average thermal sensor volume 1.5mm from the cable-whip junction, are plotted in Figure 8.11 for the cool-down periods following the first two RF exposures. The radiometric temperatures were best-

fitted to a bi-exponential curve with a root-mean-square (RMS) error of ±0.47°C. These curves were used for the H-factor calculations. In Figure 8.11(b), the experimental H-factors (solid lines) are plotted against the minimum and maximum of the computed H-factors (dashed lines). The measured absolute ΔT lies between the dashed lines immediately after the end of the RF exposure, but as time progresses, the measured ΔT deviates, decaying slower than the simulated ΔT. Similarly, the calculated H-factors match the measured H-factor at the beginning of the cool-down period but deviate as time progresses.

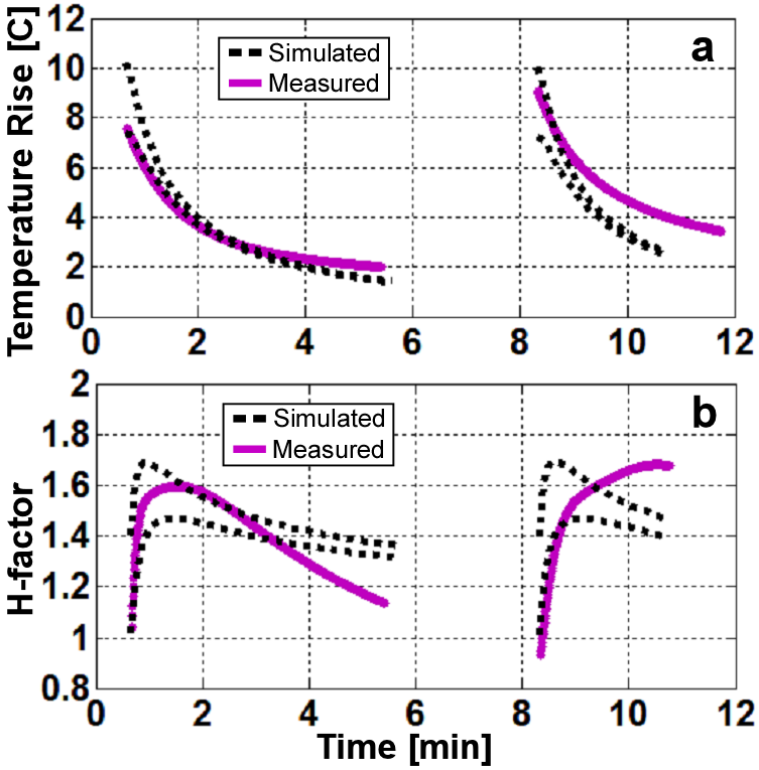


**Figure 8.11.** a. Minimum and maximum values of the simulated temperature rise [inside a 1x1.2mm$^2$ rectangle centered 1.5mm away from the junction] and (b) the H-factor inside the 1.2mm$^2$ region centered 1.5mm away from the junction are plotted in dashed lines. The measured temperature rise and the H-factor are displayed in solid lines in part (a) and (b), respectively. Only two cool-down periods after the first two RF exposures are displayed.

## 8.4.6. Analyzing Different Medium Parameters

Figure 8.12 shows the theoretical 4.1mg-averaged ΔT distribution calculated in the coronal plane intersecting the antenna after a 100s-long 4W RF exposure, for media with thermal conductivities of 0.20, 0.35 and 0.50W/m/K. The profiles for ΔT along the dashed line through the junction show that ΔT is highest for the medium with lowest $k_t$ (Figure 8.12.d). The numerically computed (spatial and temporal) peak radiometric ΔT, and the peak 1g- and 4.1mg-averaged H-factors are listed in Table 8.2. The peak 1g-averaged ΔT are calculated by averaging the pixels inside the cube centered at the antenna plane as shown in Figure 8.12(a). The results show that lowering the thermal conductivity tends to concentrate the temperature distribution around the whip-cable junction with a higher peak temperature. This is where the loopless antenna has its highest sensitivity. Consequently the peak radiometric temperature readings are highest when thermal conductivity is low, while the peak radiometric temperature is lower when the medium has higher thermal conductivity which more uniformly and rapidly distributes temperature differences.

The mean computed peak 1g-averaged H-factor in the simulated thermal conductivity range is 1.36 and the variation of individual numbers is less than 1.2%. Since the peak 1g-averaged H-factor is robust to changes in the simulated physiological thermal conductivity range, the peak 1g-averaged ΔT near an interventional loopless antenna can be reasonably estimated from the radiometry measurements, even though the thermal properties of the surrounding medium may not be exactly known. However,

the peak 1g-averaged H-factor is reached at different times after RF exposure (Figure 8.13). The peak value is reached faster if the medium has a higher thermal conductivity, while in a lower conductivity medium, the peak H-factor is reached later and stays at a higher value for a longer time.

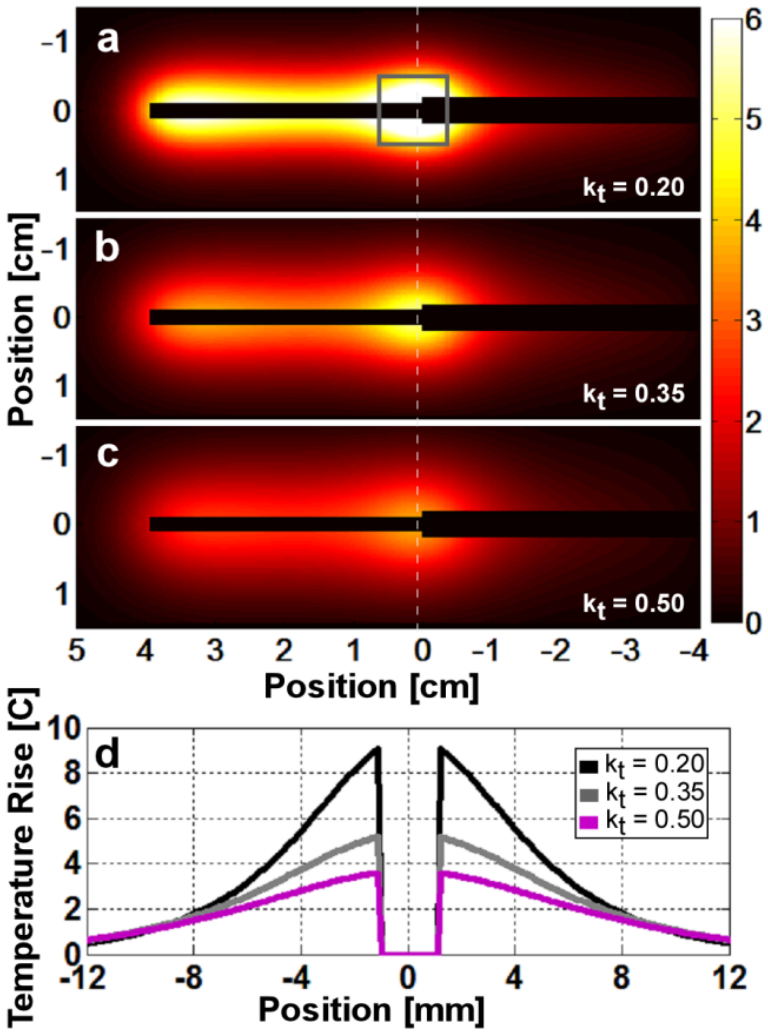


**Figure 8.12.** 4.1mg-averaged simulated temperature rise distributions 10s after 4W 100s-long RF exposure are shown for thermal conductivity values of 0.20, 0.35 and 0.50W/m/K in parts (a), (b) and (c) respectively. (d) The temperature profiles along the white dashed lines show that as the thermal conductivity decreases, the peak temperature rise increases and the distribution is more tightly confined around the junction. The gray annotated square in (a) represents the volume used to calculate the peak 1g-averaged temperature rises and H-factors.

**Table 8.2.** Numerically computed peak radiometric temperature rise, and peak 1g- and 4.1mg-averaged H-factor values are listed following a 4W 100s-long RF exposure with varying medium thermal conductivities in the human physiological range.

| Thermal Conductivity (W/m/K) | RF power (W) | Peak Radiometric ΔT (°C) | Peak 1g-ave H-factor | Peak 4.1mg-ave H-factor |
|---|---|---|---|---|
| **0.15** | 4 | 6.99 | 1.37 | 2.69 |
| **0.20** | 4 | 5.86 | 1.37 | 2.59 |
| **0.25** | 4 | 5.09 | 1.36 | 2.51 |
| **0.30** | 4 | 4.53 | 1.36 | 2.45 |
| **0.35** | 4 | 4.09 | 1.36 | 2.40 |
| **0.40** | 4 | 3.74 | 1.35 | 2.36 |
| **0.45** | 4 | 3.46 | 1.35 | 2.33 |
| **0.50** | 4 | 3.21 | 1.34 | 2.30 |

If the surrounding medium is homogeneous, then the radiometric ΔT is inversely proportional to the logarithm of the thermal conductivity (Figure 8.14), and the thermal conductivity of the medium may be estimated solely by RF radiometry, provided that RF exposure parameters are known. Reducing the averaging volume from 1g to 4.1mg in the calculations in order to match the experimental sampling volume of the thermal sensors, increased the peak ΔT and H-factors due to the antenna's high sensitivity to the temperature around the whip-cable junction. The numerically computed ΔT and H-factors for a 100s RF exposure at various exposure levels in a medium with $k_t$=0.30W/m/K are listed in Table 8.3. The computed H-factors are independent of the average RF power level, while the ΔT values scale linearly with applied power.

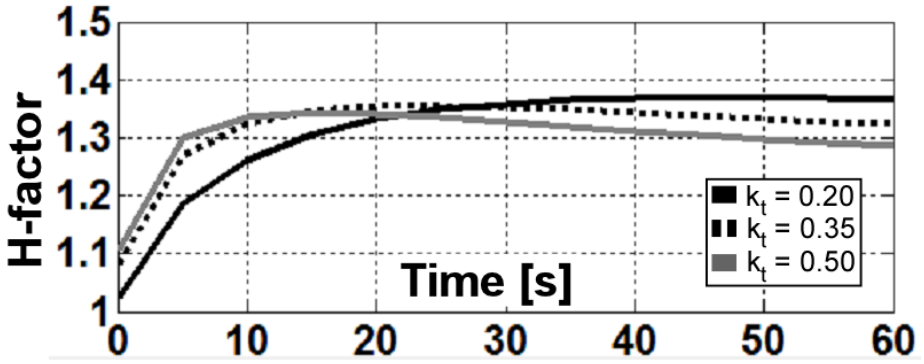


**Figure 8.13.** Computed peak 1g-averaged H-factor depends on the time duration after the end of the RF exposure and also is dependent on the thermal conductivity of the medium.

**Table 8.3.** Numerically computed peak radiometric temperature rise and peak 1g- and 4.1mg-averaged H-factor values inside a medium with thermal conductivity of 0.30W/m/K are listed a 100s-long RF exposure with power levels varying from 4 to 16.

| Thermal Conductivity (W/m/K) | RF power (W) | Peak Radiometric ΔT (°C) | Peak 1g-ave H-factor | Peak 4.1mg-ave H-factor |
|---|---|---|---|---|
| 0.30 | **4** | 4.53 | 1.36 | 2.45 |
| 0.30 | **8** | 9.06 | 1.36 | 2.45 |
| 0.30 | **16** | 18.11 | 1.36 | 2.45 |

## 8.5. Discussion

Here, we have developed a bench-top RF radiometer receiver that operates at the 3T MRI scanner frequency of 128MHz, with a bandwidth of 410kHz. When connected to an interventional MRI loopless antenna, the radiometer can directly measure and monitor the local temperature in the sensitive region of the antenna based on the amplitude of the RF noise detected between regular MRI scanning, thereby eliminating the need for any other thermometric devices. Moreover, due to the

Reciprocity Principle, the loopless antenna radiometer is most sensitive to temperature in the region that heats the most: that near the cable-whip junction [53]. It is indeed surprising that the peak 1g average local temperature in the sample at the antenna is only about 1.4 times the temperature measured by the radiometer from the entire antenna, as given by the peak 'H-factor' introduced herein. This attests to the sensitivity of the radiometer for detecting local peak temperature changes that are directly associated with the presence of the antenna, and provides the antenna with a potential "self-monitoring" function for routinely assessing device safety. Note that the peak local antenna-associated heating is sensitive to the thermal sampling volume, owing to the presence of high SAR gradients that typically occur close to conductor[55]. Reducing the sample size from 1g to 4.1mg to match the size of the fiber-optic sensors, for example, increased the peak H-factor to 1.7.

Importantly, the radiometer uses the existing internal MRI antenna. Therefore it requires no space either on the lead or the antenna for additional wires, cables or transducers that would be required for conventional thermal sensors, other than what already exists. The radiometer uses the intrinsic thermodynamic properties of matter–black body radiation–that does not require MRI, and is independent of $B_0$ the applied RF field, its inhomogeneities etc, in the scanner. Nevertheless, the system's electronics includes components that are common to those of an MRI receiver and it would be relatively simple to integrate it into an MRI scanner with potentially higher bandwidths.

When calibrated in a thermally-equilibrated homogeneous gel phantom whose

electrical and thermal properties were analogous to tissue, the loopless antenna radiometer readings tracked linearly with temperature up to at least 73°C with an accuracy within ±0.3°C at two measurements/second (Figure 8.6). The use of the Dicke switch and 50Ω reference load sufficed to control for gain variations, and could conceivably be adjusted for other load impedances.

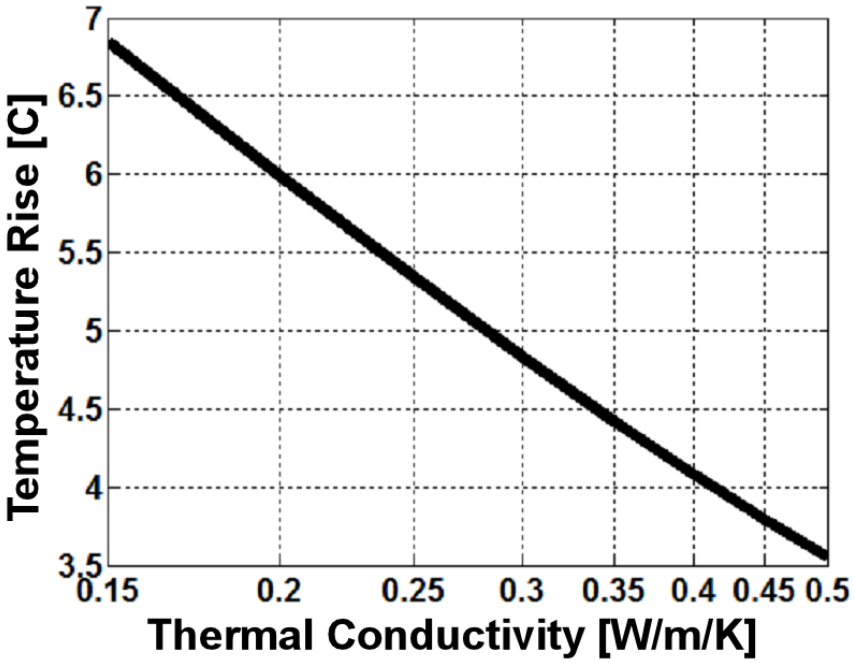


**Figure 8.14.** Numerically computed radiometric temperature rise following a 4W 100s-long RF exposure is inversely proportional to the logarithm of the thermal medium thermal conductivity.

The numerical simulations closely matched the MRI thermometry and radiometry experiments following the first two RF exposures. Results after subsequent exposures tended to deviate from the experimental results due to sensor localization errors and possibly, changes in the thermal properties of the heated medium. In addition, the computations assumed a uniform medium that did not account for the

thermal conductivity of the loopless antenna itself. The accuracy of the thermal computations during cool-down could be improved by modeling the antenna's presence inside the medium and solving the bio-heat equation via finite-difference time-domain (FDTD) based methods [229, 230].

The electrical properties of the medium may also affect the spatial distribution of the noise power, altering the sensitivity profile of the radiometer. While we did not investigate the performance of the radiometer inside media with non-uniform electrical properties, because the antenna's sensitivity is highly localized, only those variations in electrical properties near the cable-whip junction could be expected to have any effect. Moreover, the fact that the numerically computed peak 1g-averaged H-factor at 128MHz varied less than 1.2% over a 3-fold range of $k_t$ parameters for human biological tissue[228] (Table 8.2), suggests that tissue heterogeneity would not be problematic for using such a radiometer for estimating peak power in interventional applications. For example, if the Food and Drug Administration (FDA) local peak exposure guideline of 8W/kg over 5 min in any 1g tissue during MRI [231] were assumed for the loopless antenna, in the absence of thermal perfusion or conduction. The 8W/kg exposure would result in a ΔT of 0.6°C/5 min. Thus the temperature measured by RF radiometry could be used to ensure regulatory compliance to limits on either peak local SAR or peak ΔT during an interventional procedure.

Since the 1-g peak H-factor is 1.36 and the temperature detection sensitivity in a uniform phantom is better than ±0.3°C, the peak 1g-averaged temperature can be

determined to within ±0.41°C at 2Hz with the apparatus described. The radiometer's sensitivity could potentially be improved by increasing the receiver bandwidth and/or extending the signal averaging, albeit at the expense of slower temperature measurements. Also, because the radiometer readings effectively interrogate a larger volume of sensitivity, they can conceivably report peak temperatures that might otherwise be missed by the misplacement or movement of temperature sensors that have highly-localized temperature sensitivity. This may be advantageous for interventional applications.

The thermal washout rate is correlated with the thermal conductivity and perfusion rate in the surrounding medium [226, 232, 233]. Perfusion and $k_t$ can also be important factors for distinguishing tumor and normal tissue, or the stage of a tumor[233, 234]. Tumor perfusion and $k_t$ tend to increase in more advanced stages and decline with tumor necrosis[234]. Given that the radiometric temperature is inversely proportional to the logarithm of the thermal conductivity of a homogenous medium (Figure 8.14), it might be possible to use local RF radiometry measurements to estimate the $k_t$ in tumors that surrounded the detector's sensitive volume.

In conclusion, deploying an internal antenna for the dual purpose of radiometry as well as MRI detection, can offer a potentially useful means to independently monitor peak local temperature. This could not only improve the safe use of these devices during MRI, but also aid the thermal monitoring of therapies such as ablation of tumors and other pathologies[21, 235]. Such monitoring of thermal therapeutic dose could be achieved

without the artifacts that can accompany MRI thermometry: conversely, although the radiometer could be used as an independent internal reference for MRI thermometry measurements.

## 8.6. Appendix

In this section, circuit diagrams and simulation results of the filters used in the radiometer are shown. The simulations were done using AWR Design Environment (AWR Corporation, El Segunda, CA).

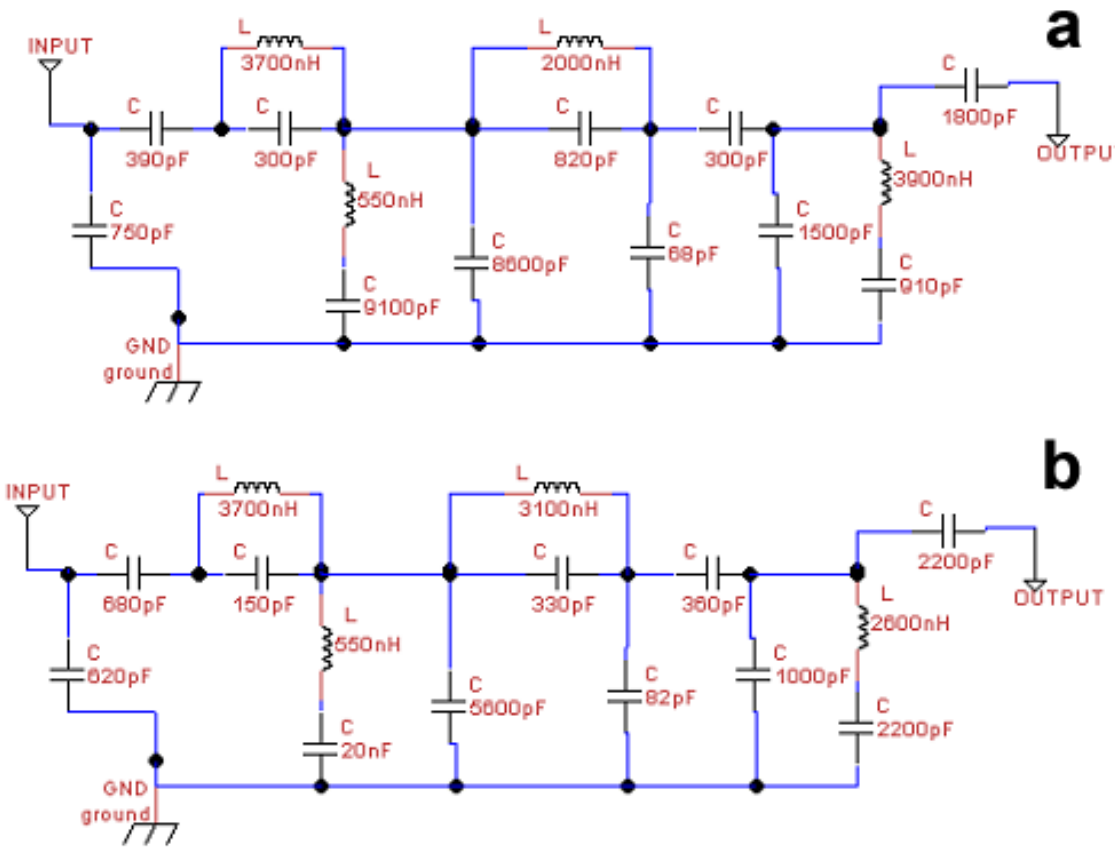


**Figure 8.15.** Circuit diagrams of the band-pass filters tuned to 3.2MHz with bandwidths of (a) 410kHz, and (b) 900kHz.

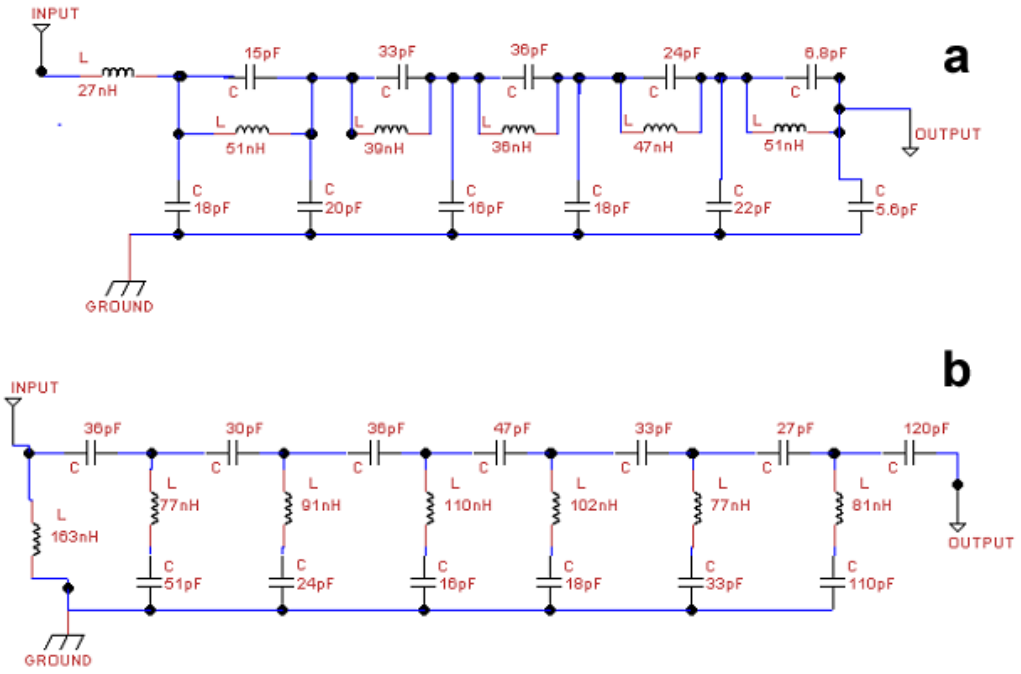


**Figure 8.16.** Circuit diagrams of the (a) 12th order low-pass, and (b) 14th order high-pass filters at 128MHz.

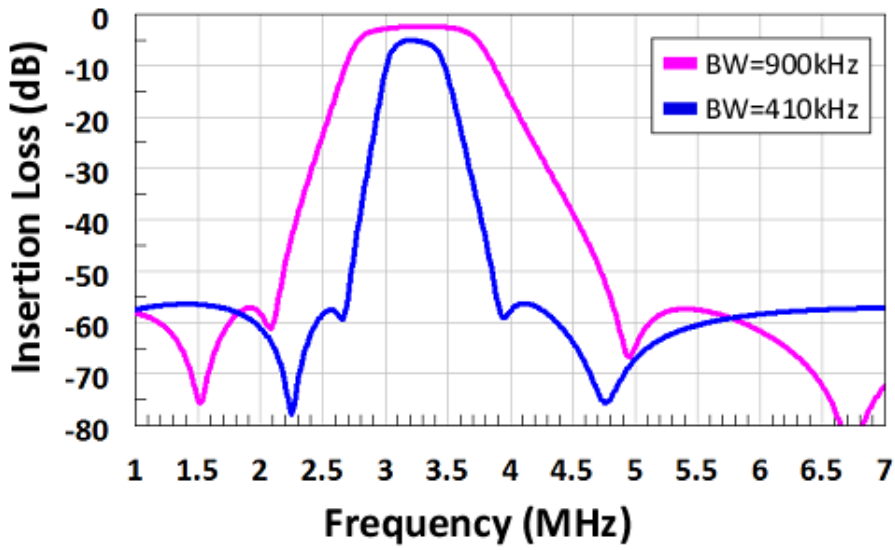


**Figure 8.17.** Simulated insertion loss of the band-pass filters tuned to 3.2MHz with bandwidths of 900kHz (pink) and 410kHz (blue) are displayed in the 1-7MHZ frequency range.

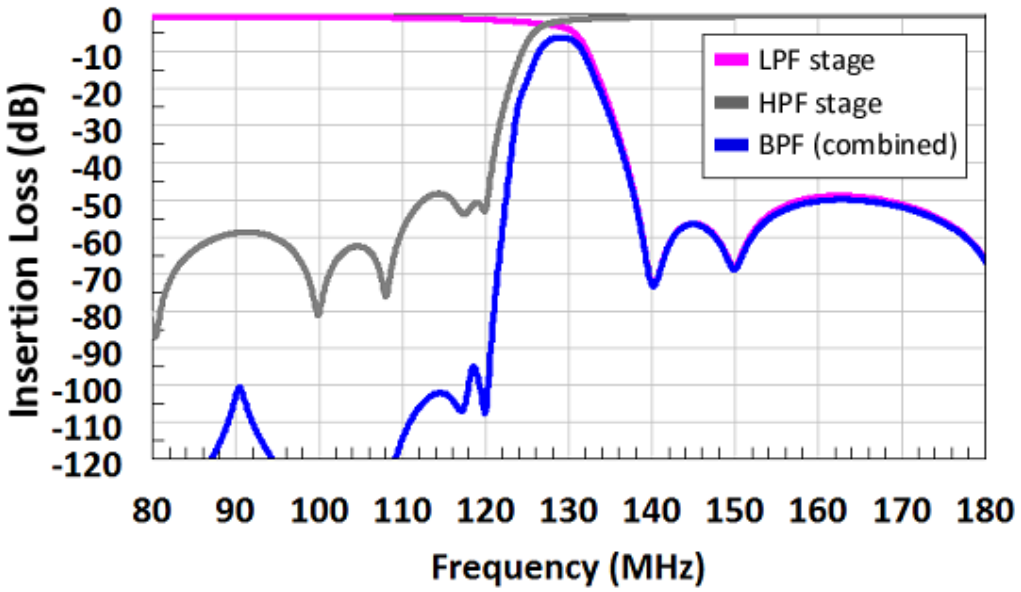


**Figure 8.18.** Simulated insertion loss of the high-frequency low-pass (pink) and high-pass (gray) filtering stages that are used on the main board are plotted. The band-pass filter (blue) on the main board includes two stages of the 14$^{th}$ order high-pass and one stage of the 12$^{th}$ order low-pass filter.

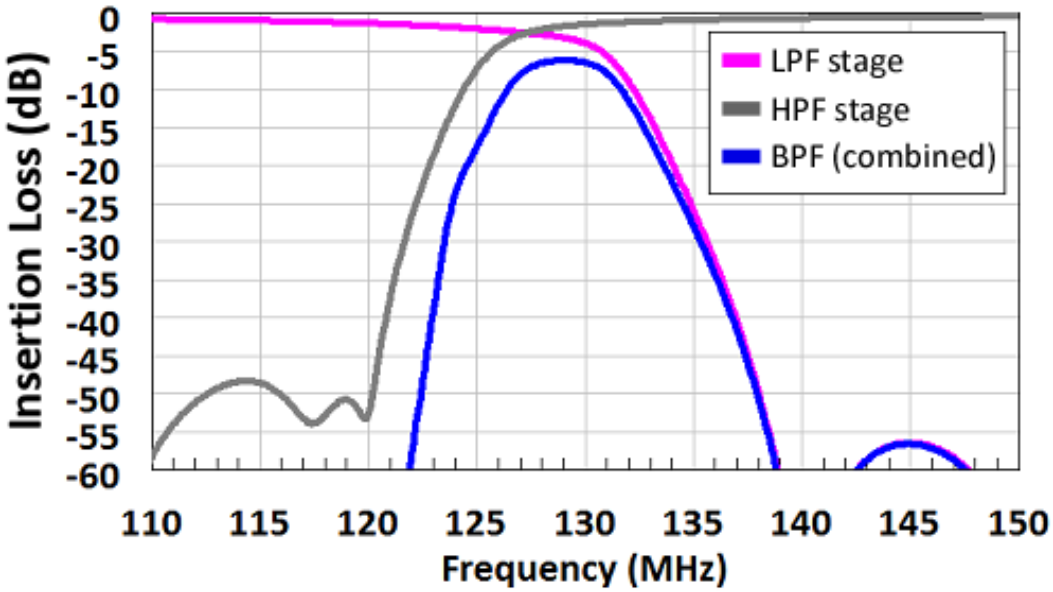


**Figure 8.19.** Simulated insertion loss of the high-frequency low-pass (pink) and high-pass (gray) filtering stages that are used on the main board are plotted. The band-pass filter (blue) on the main board includes two stages of the 14$^{th}$ order high-pass and one stage of the 12$^{th}$ order low-pass filter.

# Chapter 9.

# Conclusions and Future Work

In this work, we have investigated the performance of the interventional loopless antenna at ultra-high field (UHF, $B_0$>3T), reducing it to practice and making it safe to use at 7T. We also created an RF radiometer for measuring local heating of the loopless antenna at 3T.

We started by developing an image de-noising algorithm that is compatible with parallel imaging methods. The de-noising method based on the spectral subtraction algorithm provided up to 45% SNR improvements for single coil and multi coil SENSE reconstructed images (Chapter 3).

In Chapter 4, we have the SNR and safety performance of the 7T receive-only loopless antenna. The results showed that SNR increases quadratically with $B_0$ ($SNR \sim B_0^2$), producing 20-fold more SNR at 7T compared to 1.5T, and more than 10-fold increase in the usable field-of-view (FOV) compared to 3T. The increased SNR of the loopless antenna at 7T enabled MRI at sub-50μm in-plane resolution, which was utilized to distinguish atherosclerotic plaque components in human vessel specimens and hence could be used in future to characterize the severity of atherosclerosis.

In Chapter 5, we investigated two chemically selective imaging methods to distinguish the fat content of atherosclerotic plaques. First, we used a multi-acquisition

three-point Dixon method with the receive-only loopless antenna. Secondly, we employed an intravascular loop coil in transmit/receive mode excited with a spectrally selective modified BIR4 pulses to generate separate fat and water images. Further work is needed to compare the efficiency of these methods. In chapter 6, we acquired high-resolution MRI of brain specimens with Alzheimer's disease (AD) pathology using the loopless antenna at 7T. Initial results showed tiny regions of signal hypo-intensity possibly attributable to senile plaques in the brain with AD pathology, that were not present in tissue MRI of brain without disease. We would need to compare the pathology to confirm these findings.

At 7T, the excitation of tissue deep within the body becomes challenging due to the decreased penetration depth, $B_1$-field inhomogeneity, and increased RF power requirements, which limits the number of pulse sequences that can be safely used. In order to overcome these problems, we use the loopless antenna for both RF excitation, and MR signal reception. Spatially selective $B_1$-insensitive pulses were employed to improve the excitation homogeneity, providing ~10cm FOV which could be used for both device-tracking and target localization inside the body. The imaging FOV can be reduced by decreasing the applied RF pulse amplitude, which in turn reduce the scan time by cutting the number of phase-encoding steps. Only a few Watts of peak RF power is sufficient for local excitation, greatly reducing the RF transmit power requirements on the MR system. (Chapter 7)

Use of MRI active interventional devices in transmit and/or receive mode may

elevate temperatures near the device above levels considered safe. In chapter 8, we built an RF radiometry receiver at 128MHz with a bandwidth of 410kHz and connected it to an interventional loopless antenna, to monitor the local temperature around the device. We investigated the performance of the loopless antenna radiometer experimentally inside bio-analogous phantoms, and numerically using full-wave electromagnetic and thermal simulations. The loopless antenna radiometer was able to detect uniform temperature with an accuracy <0.3°C at 2 measurements per second, and accurately measure peak 1g averaged temperature rise within 0.41°C at the same rate. Local temperature rise can thus now be monitored by RF radiometry to ensure safe operation and/or to calculate thermal dose where the device is used for therapeutic ablation as well. We have also shown that the logarithm of the thermal conductivity of the surrounding medium is inversely proportional to the peak measured radiometric temperature rise, potentially enabling the thermal conductivity of medium to be measured using a loopless antenna radiometer. In the future, the radiometer would need to be tested inside complex media and *in vivo*.

The work presented in this thesis resulted in three journal papers[51, 53, 236], one journal article submission and several conference papers and abstracts[123, 237] so far.

# Bibliography


[1] "A.D.A.M. Medical Encyclopedia. Atlanta (GA): A.D.A.M., Inc.; Alzheimer's disease; [last reviewed 2011 Sep 26; cited 2014 Feb 16]. Available from: http://www.ncbi.nlm.nih.gov/pubmedhealth/PMH0001767/."

[2] F. Barkhof, N.C. Fox, A.J. Bastos-Leite, P. Scheltens, *Neuroimaging in Dementia*. (Springer-Verlag Berlin Heidelberg, 2011).

[3] H.L. Kantor, R.W. Briggs, R.S. Balaban, "Invivo P-31 Nuclear Magnetic-Resonance Measurements in Canine Heart Using a Catheter-Coil," Circ Res **55**, 261-266 (1984).

[4] P.R. Mueller, D.D. Stark, J.F. Simeone, S. Saini, R.J. Butch, R.R. Edelman, J. Wittenberg, J.T. Ferrucci, Jr., "MR-guided aspiration biopsy: needle design and clinical trials," Radiology **161**, 605-609 (1986).

[5] J.F. Schenck, F.A. Jolesz, P.B. Roemer, H.E. Cline, W.E. Lorensen, R. Kikinis, S.G. Silverman, C.J. Hardy, W.D. Barber, E.T. Laskaris, B. Dorri, R.W. Newman, C.E. Holley, B.D. Collick, D.P. Dietz, D.C. Mack, M.D. Ainslie, P.L. Jaskolski, M.R. Figueira, J.C.V. Lehn, S.P. Souza, C.L. Dumoulin, R.D. Darrow, R.L. Stpeters, K.W. Rohling, R.D. Watkins, D.R. Eisner, S.M. Blumenfeld, K.G. Vosburgh, "Superconducting Open-Configuration Mr-Imaging System for Image-Guided Therapy," Radiology **195**, 805-814 (1995).

[6] C.L. Dumoulin, S.P. Souza, R.D. Darrow, "Real-time position monitoring of invasive devices using magnetic resonance," Magnet Reson Med **29**, 411-415 (1993).

[7] E. Atalar, P.A. Bottomley, O. Ocali, L.C.L. Correia, M.D. Kelemen, J.A.C. Lima, E.A. Zerhouni, "High resolution intravascular MRI and MRS by using a catheter receiver coil," Magnet Reson Med **36**, 596-605 (1996).

[8] O. Ocali, E. Atalar, "Intravascular magnetic resonance imaging using a loopless catheter antenna," Magnet Reson Med **37**, 112-118 (1997).

[9] J.L. Duerk, J.S. Lewin, M. Wendt, C. Petersilge, "Remember true FISP? A high SNR, near 1-second imaging method for T2-like contrast in interventional MRI at .2 T," J Magn Reson Imaging **8**, 203-208 (1998).

[10] B.L. Daniel, R.L. Birdwell, K. Butts, K.W. Nowels, D.M. Ikeda, S.G. Heiss, C.R. Cooper, S.S. Jeffrey, F.M. Dirbas, R.J. Herfkens, "Freehand iMRI-guided large-gauge core needle biopsy: A new minimally invasive technique for diagnosis of enhancing breast lesions," J Magn Reson Imaging **13**, 896-902 (2001).

[11] P.R. Eby, C. Lehman, "MRI-guided breast interventions," Semin Ultrasound Ct **27**, 339-350 (2006).

[12] G. Fichtinger, A. Krieger, R.C. Susil, A. Tanacs, L.L. Whitcomb, E. Atalar, "Transrectal prostate biopsy inside closed MRI scanner with remote actuation, under real-time image guidance," Medical Image Computing and Computer-Assisted Intervention-Miccai 2002, Pt 1 **2488**, 91-98 (2002).

[13] A. Krieger, R.C. Susil, G. Fichtinger, E. Atalar, L.L. Whitcomb, "Design of a novel MRI compatible manipulator for image guided prostate intervention," 2004 Ieee International Conference on Robotics and Automation, Vols 1- 5, Proceedings, 377-382 5306 (2004).

[14] G.S. Fischer, I. Iordachita, C. Csoma, J. Tokuda, S.P. DiMaio, C.M. Tempany, N. Hata, G. Fichtinger, "MRI-compatible pneumatic robot for transperineal prostate needle

placement," Ieee-Asme T Mech **13**, 295-305 (2008).

[15] J. Tokuda, S.E. Song, G.S. Fischer, I.I. Iordachita, R. Seifabadi, N.B. Cho, K. Tuncali, G. Fichtinger, C.M. Tempany, N. Hata, "Preclinical evaluation of an MRI-compatible pneumatic robot for angulated needle placement in transperineal prostate interventions," Int J Comput Ass Rad **7**, 949-957 (2012).

[16] G. Adam, A. Bucker, C. Nolte-Ernsting, J. Tacke, R.W. Gunther, "Interventional MR imaging: percutaneous abdominal and skeletal biopsies and drainages of the abdomen," Eur Radiol **9**, 1471-1478 (1999).

[17] R. Catane, A. Beck, Y. Inbar, T. Rabin, N. Shabshin, S. Hengst, R.M. Pfeffer, A. Hanannel, O. Dogadkin, B. Liberman, D. Kopelman, "MR-guided focused ultrasound surgery (MRgFUS) for the palliation of pain in patients with bone metastases - preliminary clinical experience," Ann Oncol **18**, 163-167 (2007).

[18] B. Liberman, D. Gianfelice, Y. Inbar, A. Beck, T. Rabin, N. Shabshin, G. Chander, S. Hengst, R. Pfeffer, A. Chechick, A. Hanannel, O. Dogadkin, R. Catane, "Pain Palliation in Patients with Bone Metastases Using MR-Guided Focused Ultrasound Surgery: A Multicenter Study," Ann Surg Oncol **16**, 140-146 (2009).

[19] J. Fritz, P.L. Pereira, "MR-Guided pain therapy: Principles and clinical applications," Rofo-Fortschr Rontg **179**, 914-924 (2007).

[20] A.C. Lardo, H. Halperin, C. Yeung, P. Jumrussirikul, E. Atalar, E. McVeigh, "Magnetic resonance guided radiofrequency ablation: Creation and visualization of cardiac lesions," Medical Image Computing and Computer-Assisted Intervention - Miccai'98 **1496**, 189-196 (1998).

[21] R.C. Susil, C.J. Yeung, H.R. Halperin, A.C. Lardo, E. Atalar, "Multifunctional interventional devices for MRI: A combined electrophysiology/MRI catheter," Magnet Reson Med **47**, 594-600 (2002).

[22] H. Eggebrecht, H. Kuhl, G. Kaiser, S. Aker, M. Zenge, F. Breuckmann, M.E. Ladd, R. Erbel, H.H. Quick, "Feasibility of real-time magnetic resonance-guided endovascular stent-graft placement in a pig model of aortic dissection," J Am Coll Cardiol **47**, 25b-25b (2006).

[23] L. Feng, C.L. Dumoulin, S. Dashnaw, R.D. Darrow, R. Guhde, R.L. DeLaPaz, P.L. Bishop, J. Pile-Spellman, "Transfemoral catheterization of carotid arteries with real-time MR imaging guidance in pigs," Radiology **234**, 551-557 (2005).

[24] A.N. Raval, P.V. Karmarkar, M.A. Guttman, C. Ozturk, S. Sampath, R. DeSilva, R.J. Aviles, M.N. Xu, V.J. Wright, W.H. Schenke, O. Kocaturk, A.J. Dick, V.K. Raman, E. Atalar, E.R. McVeigh, R.J. Lederman, "Real-time magnetic resonance imaging-guided endovascular recanalization of chronic total arterial occlusion in a swine model," Circulation **113**, 1101-1107 (2006).

[25] D.T. Boll, E.M. Merkle, J.S. Lewin, "Low-flow vascular malformations: MR-guided percutaneous sclerotherapy in qualitative and quantitative assessment of therapy and outcome," Radiology **233**, 376-384 (2004).

[26] R. Razavi, D.L.G. Hill, S.F. Keevil, M.E. Miquel, V. Muthurangu, S. Hegde, K. Rhode, M. Barnett, J. van Vaals, D.J. Hawkes, E. Baker, "Cardiac catheterisation guided by MRI in children and adults with congenital heart disease," Lancet **362**, 1877-1882 (2003).

[27] D.L. Kraitchman, W.D. Gilson, C.H. Lorenz, "Stem cell therapy: MRI guidance and monitoring," J Magn Reson Imaging **27**, 299-310 (2008).

[28] G.R. Sutherland, T. Kaibara, D. Louw, D.I. Hoult, B. Tomanek, J. Saunders, "A mobile high-

field magnetic resonance system for neurosurgery," J Neurosurg **91**, 804-813 (1999).

[29] W.A. Hall, A.J. Martin, H.Y. Liu, E.S. Nussbaum, R.E. Maxwell, C.L. Truwit, "Brain biopsy using high-field strength interventional magnetic resonance imaging," Neurosurgery **44**, 807-813 (1999).

[30] L.C. Markun, P.A. Starr, P.S. Larson, M.M. Volz, A.J. Martin, J.L. Ostrem, "Results of interventional MRI (iMRI)-guided deep brain stimulator placement in children," Movement Disord **28**, S434-S434 (2013).

[31] A.J. Martin, P.S. Larson, F.L. Ostrem, W.K. Sootsman, P. Talke, O.M. Weber, N. Levesque, J. Myers, P.A. Starr, "Placement of deep brain stimulator electrodes using real-time high-field interventional magnetic resonance imaging," Magnet Reson Med **54**, 1107-1114 (2005).

[32] J.C. Chen, J.A. Moriarty, J.A. Derbyshire, R.D. Peters, J. Trachtenberg, S.D. Bell, J. Doyle, R. Arrelano, G.A. Wright, R.M. Henkelman, R.S. Hinks, S.Y. Lok, A. Toi, W. Kucharczyk, "Prostate cancer: MR imaging and thermometry during microwave thermal ablation-initial experience," Radiology **214**, 290-297 (2000).

[33] M.G. Lubner, C.L. Brace, J.L. Hinshaw, F.T. Lee, "Microwave Tumor Ablation: Mechanism of Action, Clinical Results, and Devices," J Vasc Interv Radiol **21**, S192-S203 (2010).

[34] H. Rempp, R. Hoffmann, J. Roland, A. Buck, A. Kickhefel, C.D. Claussen, P.L. Pereira, F. Schick, S. Clasen, "Threshold-based prediction of the coagulation zone in sequential temperature mapping in MR-guided radiofrequency ablation of liver tumours," Eur Radiol **22**, 1091-1100 (2012).

[35] M.R. Callstrom, D.E. Dupuy, S.B. Solomon, R.A. Beres, P.J. Littrup, K.W. Davis, R. Paz-Fumagalli, C. Hoffman, T.D. Atwell, J.W. Charboneau, G.D. Schmit, M.P. Goetz, J. Rubin, K.J. Brown, P.J. Novotny, J.A. Sloan, "Percutaneous image-guided cryoablation of painful metastases involving bone Multicenter Trial," Cancer-Am Cancer Soc **119**, 1033-1041 (2013).

[36] M.R. Callstrom, T.D. Atwell, J.W. Charboneau, M.A. Farrell, M.P. Goetz, J. Rubin, J.A. Sloan, P.J. Novotny, T.J. Welch, T.P. Maus, G.Y. Wong, K.J. Brown, "Painful metastases involving bone: Percutaneous image-guided cryoablation - Prospective trial interim analysis," Radiology **241**, 572-580 (2006).

[37] J. Hindley, W.M. Gedroyc, L. Regan, E. Stewart, C. Tempany, K. Hynnen, N. Macdanold, Y. Inbar, Y. Itzchak, J. Rabinovici, K. Kim, J.F. Geschwind, G. Hesley, B. Gostout, T. Ehrenstein, S. Hengst, M. Sklair-Levy, A. Shushan, F. Jolesz, "MRI guidance of focused ultrasound therapy of uterine fibroids: Early results," Am J Roentgenol **183**, 1713-1719 (2004).

[38] K. Hynynen, G. Clement, "Clinical applications of focused ultrasound-the brain," International Journal of Hyperthermia **23**, 193-202 (2007).

[39] A. Hacker, M.S. Michel, E. Marlinghaus, K.U. Kohrmann, P. Alken, "Extracorporeally induced ablation of renal tissue by high-intensity focused ultrasound," Bju Int **97**, 779-785 (2006).

[40] T. Kahn, H. Busse, *Interventional Magnetic Resonance Imaging*. (Springer, Berlin, 2012).

[41] C.J. Bakker, R.M. Hoogeveen, W.F. Hurtak, J.J. vanVaals, M.A. Viergever, W.P.T.M. Mali, "MR-guided endovascular interventions: Susceptibility-based catheter and near-real-time imaging technique," Radiology **202**, 273-276 (1997).

[42] D. Nanz, D. Weishaupt, H.H. Quick, J.F. Debatin, "TE-switched double-contrast enhanced

visualization of vascular system and instruments for MR-guided interventions," Magnet Reson Med **43**, 645-648 (2000).

[43] O. Unal, J.W. Li, W.G. Cheng, H. Yu, C.M. Strother, "MR-visible coatings for endovascular device visualization," J Magn Reson Imaging **23**, 763-769 (2006).

[44] M.E. Ladd, G.G. Zimmermann, G.C. McKinnon, G.K. von Schulthess, C.L. Dumoulin, R.D. Darrow, E. Hofmann, J.F. Debatin, "Visualization of vascular guidewires using MR tracking," Jmri-J Magn Reson Im **8**, 251-253 (1998).

[45] Q. Zhang, M. Wendt, A.J. Aschoff, J.S. Lewin, J.L. Duerk, "A multielement RF coil for MRI guidance of interventional devices," J Magn Reson Imaging **14**, 56-62 (2001).

[46] S. Zuehlsdorff, R. Umathum, S. Volz, P. Hallscheidt, C. Fink, W. Semmler, M. Bock, "MR coil design for simultaneous tip tracking and curvature delineation of a catheter," Magnet Reson Med **52**, 214-218 (2004).

[47] D.R. Elgort, E.Y. Wong, C.M. Hillenbrand, F.K. Wacker, J.S. Lewin, J.L. Duerk, "Real-time catheter tracking and adaptive imaging," J Magn Reson Imaging **18**, 621-626 (2003).

[48] M.E. Ladd, G.G. Zimmermann, H.H. Quick, J.F. Debatin, P. Boesiger, G.K. von Schulthess, G.C. McKinnon, "Active MR visualization of a vascular guidewire in vivo," Jmri-J Magn Reson Im **8**, 220-225 (1998).

[49] M. Burl, G.A. Coutts, D.J. Herlihy, R. Hill-Cottingham, J.F. Eastham, J.V. Hajnal, I.R. Young, "Twisted-pair RF coil suitable for locating the track of a catheter," Magnet Reson Med **41**, 636-638 (1999).

[50] G.C. McKinnon, J.F. Debatin, D.A. Leung, S. Wildermuth, D.J. Holtz, G.K. vonSchulthess, "Towards active guidewire visualization in interventional magnetic resonance imaging," Magn Reson Mater Phy **4**, 13-18 (1996).

[51] M.A. Erturk, A.M. El-Sharkawy, P.A. Bottomley, "Interventional loopless antenna at 7 T," Magnet Reson Med **68**, 980-988 (2012).

[52] D. Qian, P.A. Bottomley, "High-resolution intravascular magnetic resonance quantification of atherosclerotic plaque at 3T," J Cardiovasc Magn Reson **14**, 20 (2012).

[53] M.A. Erturk, A.M. El-Sharkawy, J. Moore, P.A. Bottomley, "7 Tesla MRI with a transmit/receive loopless antenna and B -insensitive selective excitation," Magnet Reson Med2013).

[54] A.M.M. El-Sharkawy, D. Qian, P.A. Bottomley, "The performance of interventional loopless MRI antennae at higher magnetic field strengths," Med Phys **35**, 1995-2006 (2008).

[55] P.A. Bottomley, A. Kumar, W.A. Edelstein, J.M. Allen, P.V. Karmarkar, "Designing passive MRI-safe implantable conducting leads with electrodes," Med Phys **37**, 3828-3843 (2010).

[56] R.B. Lufkin, "Interventional Mr-Imaging," Radiology **197**, 16-18 (1995).

[57] U.S.F.D.A. (FDA), "Criteria for Significant Risk Investigations of Magnetic Resonance Diagnostic Devices," (2003).

[58] I.E.C. (IEC), "Medical electrical equipment - Part 2-33: Particular requirements for the basic safety and essential performance of magnetic resonance equipment for medical diagnosis," (2013).

[59] C.M. Collins, M.B. Smith, "Calculations of B-1 distribution, SNR, and SAR for a surface coil adjacent to an anatomically-accurate human body model," Magnet Reson Med **45**, 692-699 (2001).

[60] Z.W. Wang, J.C. Lin, W.H. Mao, W.Z. Liu, M.B. Smith, C.M. Collins, "SAR and temperature: Simulations and comparison to regulatory limits for MRI," J Magn Reson Imaging **26**, 437-441 (2007).

[61] M.J. Collins, J.M. Allan, "Modeling and Simulation of SAR Image Texture," Ieee Transactions on Geoscience and Remote Sensing **47**, 3530-3546 (2009).

[62] A.M. El-Sharkawy, D. Qian, P.A. Bottomley, W.A. Edelstein, "A multichannel, real-time MRI RF power monitor for independent SAR determination," Med Phys **39**, 2334-2341 (2012).

[63] D. Qian, A.M.M. El-Sharkawy, P.A. Bottomley, W.A. Edelstein, "An RF dosimeter for independent SAR measurement in MRI scanners," Med Phys **40**2013).

[64] U.S.F.a.D. Administration, "MAUDE - Manufacturer and User Facility Device Experience."

[65] F.G. Shellock, "Radiofrequency energy-induced heating during MR procedures: A review," J Magn Reson Imaging **12**, 30-36 (2000).

[66] C.J. Yeung, E. Atalar, "A Green's function approach to local rf heating in interventional MRI," Med Phys **28**, 826-832 (2001).

[67] ASTM, "ASTM F2182 - 11a: Standard Test Method for Measurement of Radio Frequency Induced Heating On or Near Passive Implants During Magnetic Resonance Imaging," (2011).

[68] K.P. Pruessmann, M. Weiger, M.B. Scheidegger, P. Boesiger, "SENSE: Sensitivity encoding for fast MRI," Magnet Reson Med **42**, 952-962 (1999).

[69] G.H. Glover, E. Schneider, "3-Point Dixon Technique for True Water Fat Decomposition with Bo Inhomogeneity Correction," Magnet Reson Med **18**, 371-383 (1991).

[70] V. Rieke, K.B. Pauly, "MR thermometry," J Magn Reson Imaging **27**, 376-390 (2008).

[71] R. Nezafat, R. Ouwerkerk, A.J. Derbyshire, M. Stuber, E.R. McVeigh, "Spectrally Selective B-1-Insensitive T-2 Magnetization Preparation Sequence," Magnet Reson Med **61**, 1326-1335 (2009).

[72] J. Moore, M. Jankiewicz, A.W. Anderson, J.C. Gore, "Slice-selective excitation with B(1)(+)-insensitive composite pulses," J Magn Reson **214**, 200-211 (2012).

[73] D.G. Nishimura, *Principles of Magnetic Resonance Imaging*. (1996).

[74] J. Pauly, D. Nishimura, A. Macovski, "A K-Space Analysis of Small-Tip-Angle Excitation," J Magn Reson **81**, 43-56 (1989).

[75] F. Bloch, W.W. Hansen, M. Packard, "Nuclear Induction," Phys Rev **69**, 127-127 (1946).

[76] W.A. Edelstein, J.M.S. Hutchison, G. Johnson, T. Redpath, "Spin Warp Nmr Imaging and Applications to Human Whole-Body Imaging," Physics in Medicine and Biology **25**, 751-756 (1980).

[77] A. Haase, J. Frahm, D. Matthaei, W. Hanicke, K.D. Merboldt, "Flash Imaging - Rapid Nmr Imaging Using Low Flip-Angle Pulses," J Magn Reson **67**, 258-266 (1986).

[78] M.A. Bernstein, K.F. King, X.J. Zhou, *Handbook of MRI Pulse Sequences*. (Elsevier Academic Press, 2004).

[79] E.M. Haacke, Y.B. Xu, Y.C.N. Cheng, J.R. Reichenbach, "Susceptibility weighted imaging (SWI)," Magnet Reson Med **52**, 612-618 (2004).

[80] J.R. Reichenbach, R. Venkatesan, D.J. Schillinger, D.K. Kido, E.M. Haacke, "Small vessels in the human brain: MR venography with deoxyhemoglobin as an intrinsic contrast agent," Radiology **204**, 272-277 (1997).

[81] R.D. Peters, R.S. Hinks, R.M. Henkelman, "Ex vivo tissue-type independence in proton-

resonance frequency shift MR thermometry," Magnet Reson Med **40**, 454-459 (1998).

[82] W.T. Dixon, "Simple Proton Spectroscopic Imaging," Radiology **153**, 189-194 (1984).

[83] Y. Wang, D. Li, E.M. Haacke, J.J. Brown, "A three-point Dixon method for water and fat separation using 2D and 3D gradient-echo techniques," J Magn Reson Imaging **8**, 703-710 (1998).

[84] P.B. Roemer, W.A. Edelstein, C.E. Hayes, S.P. Souza, O.M. Mueller, "The Nmr Phased-Array," Magnet Reson Med **16**, 192-225 (1990).

[85] M.A. Griswold, D.K. Sodickson, P.M. Jakob, Q. Chen, J.W. Goldfarb, R.R. Edelman, "Resolution enhancement and artifact reduction in single shot MR imaging using SiMultaneous Acquisition of Spatial Harmonics (SMASH)," Radiology **205**, 1040-1040 (1997).

[86] M.A. Griswold, P.M. Jakob, R.M. Heidemann, M. Nittka, V. Jellus, J.M. Wang, B. Kiefer, A. Haase, "Generalized Autocalibrating Partially Parallel Acquisitions (GRAPPA)," Magnet Reson Med **47**, 1202-1210 (2002).

[87] E.M. Haacke, R.W. Brown, M.R. Thompson, R. Venkatesan, *Magnetic Resonance Imaging: Physical Principles and Sequence Design*. (Wiley, 1999).

[88] S. Trattnig, S. Zbyn, V. Juras, P. Szomolanyi, S. Domayer, I.M. Noebauer-Huhmann, G. Welsch, B. Schmitt, "Ultra High Field (7 Tesla) MRI for Musculoskeletal Applications," in *MAGNETOM Flash*, *Vol. 2* (2012), pp. 95-102.

[89] D. Browning, "Giant magnet makes University of Minnesota attractive to brain mapping researchers," in *Star Tribune* (Minneapolis, 2013).

[90] D.I. Hoult, P.C. Lauterbur, "Sensitivity of the Zeugmatographic Experiment Involving Human Samples," J Magn Reson **34**, 425-433 (1979).

[91] P.A. Bottomley, W.A. Edelstein, "Power Deposition in Whole-Body Nmr Imaging," Med Phys **8**, 510-512 (1981).

[92] C.N. Chen, V.J. Sank, S.M. Cohen, D.I. Hoult, "The Field-Dependence of Nmr Imaging .1. Laboratory Assessment of Signal-to-Noise Ratio and Power Deposition," Magnet Reson Med **3**, 722-729 (1986).

[93] D.I. Hoult, C.N. Chen, V.J. Sank, "The Field-Dependence of Nmr Imaging .2. Arguments Concerning an Optimal Field-Strength," Magnet Reson Med **3**, 730-746 (1986).

[94] H. Wen, T.J. Denison, R.W. Singerman, R.S. Balaban, "The intrinsic signal-to-noise ratio in human cardiac imaging at 1.5, 3, and 4 T," J Magn Reson **125**, 65-71 (1997).

[95] J.H. Duyn, P. van Gelderen, T.Q. Li, J.A. de Zwart, A.P. Koretsky, M. Fukunaga, "High-field MRI of brain cortical substructure based on signal phase," P Natl Acad Sci USA **104**, 11796-11801 (2007).

[96] S. Wharton, A. Schafer, R. Bowtell, "Susceptibility Mapping in the Human Brain Using Threshold-Based k-Space Division," Magnet Reson Med **63**, 1292-1304 (2010).

[97] H. Bomsdorf, T. Helzel, D. Kunz, P. Roschmann, O. Tschendel, J. Wieland, "Spectroscopy and imaging with a 4 tesla whole-body MR system," Nmr Biomed **1**, 151-158 (1988).

[98] P. Roschmann, "Radiofrequency Penetration and Absorption in the Human-Body - Limitations to High-Field Whole-Body Nuclear-Magnetic-Resonance Imaging," Med Phys **14**, 922-931 (1987).

[99] P.A. Bottomley, E.R. Andrew, "Rf Magnetic-Field Penetration, Phase-Shift and Power Dissipation in Biological Tissue - Implications for Nmr Imaging," Physics in Medicine and Biology **23**, 630-643 (1978).

[100] P.A. Bottomley, R.W. Redington, W.A. Edelstein, J.F. Schenck, "Estimating Radiofrequency Power Deposition in Body Nmr Imaging," Magnet Reson Med **2**, 336-349 (1985).

[101] J.T. Vaughan, M. Garwood, C.M. Collins, W. Liu, L. DelaBarre, G. Adriany, P. Andersen, H. Merkle, R. Goebel, M.B. Smith, K. Ugurbil, "7T vs. 4T: RF power, homogeneity, and signal-to-noise comparison in head images," Magnet Reson Med **46**, 24-30 (2001).

[102] P.M. Robitaille, L. Berliner, *Ultra High Field Magnetic Resonance Imaging*. (Springer US, 2006).

[103] T.S. Ibrahim, R. Lee, A.M. Abduljalil, B.A. Baertlein, P.M.L. Robitaille, "Dielectric resonances and B-1 field inhomogeneity in UHFMRI: computational analysis and experimental findings," Magn Reson Imaging **19**, 219-226 (2001).

[104] T.S. Ibrahim, R. Lee, B.A. Baertlein, A.M. Abduljalil, H. Zhu, P.M. Robitaille, "Effect of RF coil excitation on field inhomogeneity at ultra high fields: a field optimized TEM resonator," Magn Reson Imaging **19**, 1339-1347 (2001).

[105] G.C. Wiggins, A. Potthast, C. Triantafyllou, C.J. Wiggins, L.L. Wald, "Eight-channel phased array coil and detunable TEM volume coil for 7 T brain imaging," Magnet Reson Med **54**, 235-240 (2005).

[106] P.F. Van de Moortele, C. Akgun, G. Adriany, S. Moeller, J. Ritter, C.M. Collins, M.B. Smith, J.T. Vaughan, K. Ugurbil, "B(1) destructive interferences and spatial phase patterns at 7 T with a head transceiver array coil," Magnet Reson Med **54**, 1503-1518 (2005).

[107] T. Vaughan, L. DelaBarre, C. Snyder, J.F. Tian, C. Akgun, D. Shrivastava, W.Z. Liu, C. Olson, G. Adriany, J. Strupp, P. Andersen, A. Gopinath, P.F. van de Moortele, M. Garwood, K. Ugurbil, "9.4T human MRI: Preliminary results," Magnet Reson Med **56**, 1274-1282 (2006).

[108] P. Vernickel, P. Roschmann, C. Findeklee, K.M. Ludeke, C. Leussler, J. Overwag, U. Katscher, I. Grasslin, K. Schunemann, "Eight-channel transmit/receive body MRI coil at 3T," Magnet Reson Med **58**, 381-389 (2007).

[109] B. van den Bergen, C.A. Van den Berg, L.W. Bartels, J.J. Lagendijk, "7 T body MRI: B1 shimming with simultaneous SAR reduction," Physics in Medicine and Biology **52**, 5429-5441 (2007).

[110] G.J. Metzger, C. Snyder, C. Akgun, T. Vaughan, K. Ugurbil, P.F. Van de Moortele, "Local B1+ shimming for prostate imaging with transceiver arrays at 7T based on subject-dependent transmit phase measurements," Magnet Reson Med **59**, 396-409 (2008).

[111] C.J. Snyder, L. DelaBarre, G.J. Metzger, P.F. van de Moortele, C. Akgun, K. Ugurbil, J.T. Vaughan, "Initial results of cardiac imaging at 7 Tesla," Magnet Reson Med **61**, 517-524 (2009).

[112] U. Katscher, P. Bornert, "Parallel RF transmission in MRI," Nmr Biomed **19**, 393-400 (2006).

[113] G.J. Metzger, E.J. Auerbach, C. Akgun, J. Simonson, X.M. Bi, K. Ugurbil, P.F. van de Moortele, "Dynamically Applied B-1(+) Shimming Solutions for Non-Contrast Enhanced Renal Angiography at 7.0 Tesla," Magnet Reson Med **69**, 114-126 (2013).

[114] B. van den Bergen, D.W.J. Klomp, A.J.E. Raaijmakers, C.A. de Castro, V.O. Boer, H. Kroeze, P.R. Luijten, J.J.W. Lagendijk, C.A.T. van den Berg, "Uniform prostate imaging and spectroscopy at 7 T: comparison between a microstrip array and an endorectal coil," Nmr Biomed **24**, 358-365 (2011).

[115] C.S. Arteaga de Castro, B. van den Bergen, P.R. Luijten, U.A. van der Heide, M. van Vulpen, D.W. Klomp, "Improving SNR and B1 transmit field for an endorectal coil in 7 T MRI and MRS of prostate cancer," Magnet Reson Med **68**, 311-318 (2012).

[116] G.J. Metzger, P.F. van de Moortele, C. Akgun, C.J. Snyder, S. Moeller, J. Strupp, P. Andersen, D. Shrivastava, T. Vaughan, K. Ugurbil, G. Adriany, "Performance of external and internal coil configurations for prostate investigations at 7 T," Magnet Reson Med **64**, 1625-1639 (2010).

[117] A. Graessl, W. Renz, F. Hezel, M.A. Dieringer, L. Winter, C. Oezerdem, J. Rieger, P. Kellman, D. Santoro, T.D. Lindel, T. Frauenrath, H. Pfeiffer, T. Niendorf, "Modular 32-channel transceiver coil array for cardiac MRI at 7.0T," Magn Reson Med2013).

[118] A. Grassl, L. Winter, C. Thalhammer, W. Renz, P. Kellman, C. Martin, F. von Knobelsdorff-Brenkenhoff, V. Tkachenko, J. Schulz-Menger, T. Niendorf, "Design, evaluation and application of an eight channel transmit/receive coil array for cardiac MRI at 7.0 T," Eur J Radiol **82**, 752-759 (2013).

[119] A. Kumar, W.A. Edelstein, P.A. Bottomley, "Noise Figure Limits for Circular Loop MR Coils," Magnet Reson Med **61**, 1201-1209 (2009).

[120] B.S. Qiu, P. Karmarkar, C. Brushett, F.B. Gao, R. Kon, S. Kar, E. Atalar, X.M. Yang, "Development of a 0.014-inch magnetic resonance imaging guidewire," Magnet Reson Med **53**, 986-990 (2005).

[121] R.C. Susil, C.J. Yeung, E. Atalar, "Intravascular extended sensitivity (IVES) MRI antennas," Magnet Reson Med **50**, 383-390 (2003).

[122] D. Qian, A.M.M. El-Sharkawy, E. Atalar, P.A. Bottomley, "Interventional MRI: Tapering Improves the Distal Sensitivity of the Loopless Antenna," Magnet Reson Med **63**, 797-802 (2010).

[123] M.A. Erturk, A.M. El-Sharkawy, "Characterizing bazooka baluns," in *ISMRM 21st Scientific Meeting & Exhibition* (Salt Lake City USA, 2013), pp. 4372.

[124] R.M. Botnar, P. Steiner, B. Dubno, P. Erhart, G.K. von Schulthess, J.F. Debatin, "Temperature quantification using the proton frequency shift technique: In vitro and in vivo validation in an open 0.5 tesla interventional MR scanner during RF ablation," J Magn Reson Imaging **13**, 437-444 (2001).

[125] S. Michaeli, G. Oz, D.J. Sorce, M. Garwood, K. Ugurbil, S. Majestic, P. Tuite, "Assessment of brain iron and neuronal integrity in patients with Parkinson's disease using novel MRI contrasts," Movement Disord **22**, 334-340 (2007).

[126] P. Perona, J. Malik, "Scale-Space and Edge-Detection Using Anisotropic Diffusion," Ieee Transactions on Pattern Analysis and Machine Intelligence **12**, 629-639 (1990).

[127] A.A. Samsonov, C.R. Johnson, "Noise-adaptive nonlinear diffusion filtering of MR images with spatially varying noise levels," Magnet Reson Med **52**, 798-806 (2004).

[128] J. Tsao, S. Kozerke, P. Boesiger, K.P. Pruessmann, "Optimizing spatiotemporal sampling for k-t BLAST and k-t SENSE: Application to high-resolution real-time cardiac steady-state free precession," Magnet Reson Med **53**, 1372-1382 (2005).

[129] R.D. Nowak, "Wavelet-based Rician noise removal for magnetic resonance imaging," Ieee T Image Process **8**, 1408-1419 (1999).

[130] M. Weiger, P. Boesiger, P.R. Hilfiker, D. Weishaupt, K.P. Pruessmann, "Sensitivity encoding as a means of enhancing the SNR efficiency in steady-state MRI," Magnet Reson Med **53**, 177-185 (2005).

[131] R. Wirestam, A. Bibic, J. Latt, S. Brockstedt, F. Stahlberg, "Denoising of complex MRI data by wavelet-domain filtering: Application to high-b-value diffusion-weighted imaging," Magnet Reson Med **56**, 1114-1120 (2006).

[132] J. Portilla, V. Strela, M.J. Wainwright, E.P. Simoncelli, "Image denoising using scale mixtures of Gaussians in the wavelet domain," Ieee T Image Process **12**, 1338-1351 (2003).

[133] A. Buades, B. Coll, J.M. Morel, "A non-local algorithm for image denoising," 2005 IEEE Computer Society Conference on Computer Vision and Pattern Recognition, Vol 2, Proceedings, 60-65 (2005).

[134] J.V. Manjon, J. Carbonell-Caballero, J.J. Lull, G. Garcia-Marti, L. Marti-Bonmati, M. Robles, "MRI denoising using Non-Local Means," Medical Image Analysis **12**, 514-523 (2008).

[135] J.V. Manjon, P. Coupe, L. Marti-Bonmati, D.L. Collins, M. Robles, "Adaptive Non-Local Means Denoising of MR Images With Spatially Varying Noise Levels," J Magn Reson Imaging **31**, 192-203 (2010).

[136] N.A. Thacker, J.V. Manjon, P.A. Bromiley, "Statistical interpretation of non-local means," Iet Computer Vision **4**, 162-172 (2010).

[137] S.V. Vaseghi, *Advanced Digital Signal Processing and Noise Reduction*, 2 ed. (John Wiley & Sons, Ltd, 2000).

[138] S.F. Boll, "Suppression of Acoustic Noise in Speech Using Spectral Subtraction," Ieee Transactions on Acoustics Speech and Signal Processing **27**, 113-120 (1979).

[139] Y.M. Kadah, "Adaptive denoising of event-related functional magnetic resonance imaging data using spectral substraction," Ieee Transactions on Biomedical Engineering **51**, 1944-1953 (2004).

[140] G. Gerig, O. Kubler, R. Kikinis, F.A. Jolesz, "Nonlinear Anisotropic Filtering of Mri Data," Ieee T Med Imaging **11**, 221-232 (1992).

[141] D. Lopes, "Anisotropic Diffusion," (2007).

[142] F.-H. Lin, *Vol. 2012* (2005).

[143] O. Dietrich, J.G. Raya, S.B. Reeder, M.F. Reiser, S.O. Schoenberg, "Measurement of signal-to-noise ratios in MR images: Influence of multichannel coils, parallel imaging, and reconstruction filters," J Magn Reson Imaging **26**, 375-385 (2007).

[144] Z. Wang, A.C. Bovik, H.R. Sheikh, E.P. Simoncelli, "Image quality assessment: From error visibility to structural similarity," Ieee T Image Process **13**, 600-612 (2004).

[145] J. Sijbers, A.J. den Dekker, "Maximum likelihood estimation of signal amplitude and noise variance from MR data," Magnet Reson Med **51**, 586-594 (2004).

[146] J. Sijbers, A.J. den Dekker, J. Van Audekerke, M. Verhoye, D. Van Dyck, "Estimation of the noise in magnitude MR images," Magn Reson Imaging **16**, 87-90 (1998).

[147] T. Jaermann, K.P. Pruessmann, A. Valavanis, S. Kollias, P. Boesiger, "Influence of SENSE on image properties in high-resolution single-shot echo-planar DTI," Magnet Reson Med **55**, 335-342 (2006).

[148] J. Orchard, M. Ebrahimi, A. Wong, "Efficient Nonlocal-Means Denoising Using the Svd," 2008 15th Ieee International Conference on Image Processing, Vols 1-5, 1732-1735 (2008).

[149] S. Michaeli, M. Garwood, X.H. Zhu, L. DelaBarre, P. Andersen, G. Adriany, H. Merkle, K. Ugurbil, W. Chen, "Proton T-2 relaxation study of water, N-acetylaspartate, and creatine

in human brain using Hahn and Carr-Purcell spin echoes at 4T and 7T," Magnet Reson Med **47**, 629-633 (2002).

150 T.T. Vaughan, C.J. Snyder, L.J. DelaBarre, P.J. Bolan, J. Tian, L. Bolinger, G. Adriany, P. Andersen, J. Strupp, K. Ugurbil, "Whole-Body Imaging at 7T: Preliminary Results," Magnetic Resonance in Medicine **61**, 244-248 (2009).

151 D.I. Hoult, "Sensitivity and power deposition in a high-field imaging experiment," J Magn Reson Imaging **12**, 46-67 (2000).

152 A.C. Zelinski, L.M. Angelone, V.K. Goyal, G. Bonmassar, E. Adalsteinsson, L.L. Wald, "Specific absorption rate studies of the parallel transmission of inner-volume excitations at 7T," Journal of Magnetic Resonance Imaging **28**, 1005-1018 (2008).

153 D.W.J. Klomp, A.K. Bitz, A. Heerschap, T.W.J. Scheenen, "Proton spectroscopic imaging of the human prostate at 7 T," Nmr in Biomedicine **22**, 495-501 (2009).

154 B. van den Bergen, Klomp, D. W., Raaijmakers, A. J., de Castro, C. A., Boer, V. O., Kroeze, H., Luijten, P. R., Lagendijk, J. J. and van den Berg, C. A. T. , "Uniform prostate imaging and spectroscopy at 7 T: comparison between a microstrip array and an endorectal coil," Nmr Biomedonline 2010).

155 A. Kumar, Atalar, E., presented at the 9th Annual Meeting of ISMRM, In: Proceedings of the 9th Annual Meeting of ISMRM Glasgow, Scotland, 2001.

156 J. Serfaty, X. Yang, P. Aksit, M. Solaiyappan, E. Atalar, "Toward MR-guided coronary interventions," Radiology **217**, 422-422 (2000).

157 J.M. Serfaty, X.M. Yang, T.K. Foo, A. Kumar, A. Derbyshire, E. Atalar, "MRI-guided coronary catheterization and PTCA: A feasibility study on a dog model," Magnetic Resonance in Medicine **49**, 258-263 (2003).

158 X.M. Yang, E. Atalar, "Intravascular MR imaging-guided balloon angioplasty with an MR imaging guide wire: Feasibility study in rabbits," Radiology **217**, 501-506 (2000).

159 K.A. Shunk, J. Garot, E. Atalar, J.A.C. Lima, "Transesophageal magnetic resonance imaging of the aortic arch and descending thoracic aorta in patients with aortic atherosclerosis," Journal of the American College of Cardiology **37**, 2031-2035 (2001).

160 C.R. Weiss, C. Georgiades, L.V. Hofmann, R. Schulick, M. Choti, P. Thuluvath, D.A. Bluemke, A. Arepally, "Intrabiliary MR imaging: Assessment of biliary obstruction with use of an intraluminal MR receiver coil," Journal of Vascular and Interventional Radiology **17**, 845-853 (2006).

161 A.M. El-Sharkawy, D. Qian, P.A. Bottomley, "The performance of interventional loopless MRI antennae at higher magnetic field strengths," Medical Physics **35**, 1995-2006 (2008).

162 S. Sathyanarayana, P.A. Bottomley, "MRI endoscopy using intrinsically localized probes," Med Phys **36**, 908-919 (2009).

163 S. Sathyanarayana, M. Schar, D.L. Kraitchman, P.A. Bottomley, "Towards Real-Time Intravascular Endoscopic Magnetic Resonance Imaging," Jacc-Cardiovascular Imaging **3**, 1158-1165 (2010).

164 C.J. Yeung, P. Karmarkar, E.R. McVeigh, "Minimizing RF heating of conducting wires in MRI," Magnetic Resonance in Medicine **58**, 1028-1034 (2007).

165 S. Weiss, P. Vernickel, T. Schaeffter, V. Schulz, B. Gleichl, "Transmission line for improved RF safety of interventional devices," Magnetic Resonance in Medicine **54**, 182-189 (2005).

[166] A. International, "Revision of F2182-09. Standard test method for measurement of radio frequency induced heating on or near passive implants during magnetic resonance imaging," (West Conshohocken, PA 19428, 15 November 2009).

[167] M. Schar, E.J. Vonken, M. Stuber, "Simultaneous B-0- and B-1+-Map Acquisition for Fast Localized Shim, Frequency, and RF Power Determination in the Heart at 3 T," Magnetic Resonance in Medicine **63**, 419-426 (2010).

[168] P.A. Bottomley, "A practical guide to getting NMR spectra in viva," Medical Magnetic Resonance Imaging and Spectroscopy, A Primer, 81-95 (1986).

[169] W.A. Edelstein, G.H. Glover, C.J. Hardy, R.W. Redington, "The Intrinsic Signal-to-Noise Ratio in Nmr Imaging," Magnet Reson Med **3**, 604-618 (1986).

[170] C.f.D.a.R.H. States Food and Drug Administration (FDA), "Guidance for industry and FDA staff. Criteria for significant risk investigations of magnetic resonance diagnostic devices," (FDA, Rockville MD, 14 July 2003).

[171] N. Vayssiere, S. Hemm, M. Zanca, M.C. Picot, A. Bonafe, L. Cif, P. Frerebeau, P. Coubes, "Magnetic resonance imaging stereotactic target localization for deep brain stimulation in dystonic children," J Neurosurg **93**, 784-790 (2000).

[172] P.V. Karmarkar, Baker, K. B., Lowe, M. J., Phillips, M., Steiner, C., Viohl, I., Nyenhuis, J. A., Bottomley, P. A., Rezai, A. R., "An Active Microelectrode System for Experimental MRI-Guided Intracranial Intervention," Proc Intl Soc Mag Reson Med 2005 **13**, 2162 (

[173] H.C. Stary, A.B. Chandler, R.E. Dinsmore, V. Fuster, S. Glagov, W. Insull, Jr., M.E. Rosenfeld, C.J. Schwartz, W.D. Wagner, R.W. Wissler, "A definition of advanced types of atherosclerotic lesions and a histological classification of atherosclerosis. A report from the Committee on Vascular Lesions of the Council on Arteriosclerosis, American Heart Association," Arterioscler Thromb Vasc Biol **15**, 1512-1531 (1995).

[174] M. Garwood, L. DelaBarre, "The return of the frequency sweep: Designing adiabatic pulses for contemporary NMR," J Magn Reson **153**, 155-177 (2001).

[175] K. Ugurbil, M. Garwood, M.R. Bendall, "Amplitude-Modulated and Frequency-Modulated Pulses to Achieve 90-Degrees Plane Rotations with Inhomogeneous-B1 Fields," J Magn Reson **72**, 177-185 (1987).

[176] K. Ugurbil, M. Garwood, A.R. Rath, M.R. Bendall, "Amplitude-Modulated and Frequency Phase-Modulated Refocusing Pulses That Induce Plane Rotations Even in the Presence of Inhomogeneous B1 Fields," J Magn Reson **78**, 472-497 (1988).

[177] G. Wang, A.M. El-Sharkawy, W.A. Edelstein, M. Schar, P.A. Bottomley, "Measuring T(2) and T(1), and imaging T(2) without spin echoes," J Magn Reson **214**, 273-280 (2012).

[178] R. Nezafat, M. Stuber, R. Ouwerkerk, A.M. Gharib, M.Y. Desai, R.I. Pettigrew, "B-1-insensitive T-2 preparation for improved coronary magnetic resonance angiography at 3 T," Magnet Reson Med **55**, 858-864 (2006).

[179] R.A. de Graaf, Y. Luo, M. Terpstra, M. Garwood, "Spectral editing with adiabatic pulses," J Magn Reson B **109**, 184-193 (1995).

[180] W. Thies, L. Bleiler, "2013 Alzheimer's disease facts and figures," Alzheimers Dement **9**, 208-245 (2013).

[181] C.R. Jack, Jr., D.S. Knopman, W.J. Jagust, L.M. Shaw, P.S. Aisen, M.W. Weiner, R.C. Petersen, J.Q. Trojanowski, "Hypothetical model of dynamic biomarkers of the Alzheimer's pathological cascade," Lancet Neurol **9**, 119-128 (2010).

[182] J.L. Cummings, H.V. Vinters, G.M. Cole, Z.S. Khachaturian, "Alzheimer's disease:

etiologies, pathophysiology, cognitive reserve, and treatment opportunities," Neurology **51**, S2-17; discussion S65-17 (1998).

183 W.E. Klunk, H. Engler, A. Nordberg, Y. Wang, G. Blomqvist, D.P. Holt, M. Bergstrom, I. Savitcheva, G.F. Huang, S. Estrada, B. Ausen, M.L. Debnath, J. Barletta, J.C. Price, J. Sandell, B.J. Lopresti, A. Wall, P. Koivisto, G. Antoni, C.A. Mathis, B. Langstrom, "Imaging brain amyloid in Alzheimer's disease with Pittsburgh Compound-B," Ann Neurol **55**, 306-319 (2004).

184 M.C. Tartaglia, H.J. Rosen, B.L. Miller, "Neuroimaging in dementia," Neurotherapeutics **8**, 82-92 (2011).

185 C.R. Jack, Jr., M. Garwood, T.M. Wengenack, B. Borowski, G.L. Curran, J. Lin, G. Adriany, O.H. Grohn, R. Grimm, J.F. Poduslo, "In vivo visualization of Alzheimer's amyloid plaques by magnetic resonance imaging in transgenic mice without a contrast agent," Magn Reson Med **52**, 1263-1271 (2004).

186 R. Chamberlain, D. Reyes, G.L. Curran, M. Marjanska, T.M. Wengenack, J.F. Poduslo, M. Garwood, C.R. Jack, Jr., "Comparison of amyloid plaque contrast generated by T2-weighted, T2*-weighted, and susceptibility-weighted imaging methods in transgenic mouse models of Alzheimer's disease," Magn Reson Med **61**, 1158-1164 (2009).

187 J. Zhang, P. Yarowsky, M.N. Gordon, G. Di Carlo, S. Munireddy, P.C. van Zijl, S. Mori, "Detection of amyloid plaques in mouse models of Alzheimer's disease by magnetic resonance imaging," Magn Reson Med **51**, 452-457 (2004).

188 S. Jaffar, S.E. Counts, S.Y. Ma, E. Dadko, M.N. Gordon, D. Morgan, E.J. Mufson, "Neuropathology of mice carrying mutant APP(swe) and/or PS1(M146L) transgenes: alterations in the p75(NTR) cholinergic basal forebrain septohippocampal pathway," Exp Neurol **170**, 227-243 (2001).

189 M.N. Gordon, L.A. Holcomb, P.T. Jantzen, G. DiCarlo, D. Wilcock, K.W. Boyett, K. Connor, J. Melachrino, J.P. O'Callaghan, D. Morgan, "Time course of the development of Alzheimer-like pathology in the doubly transgenic PS1+APP mouse," Exp Neurol **173**, 183-195 (2002).

190 H. Benveniste, G. Einstein, K.R. Kim, C. Hulette, G.A. Johnson, "Detection of neuritic plaques in Alzheimer's disease by magnetic resonance microscopy," Proc Natl Acad Sci U S A **96**, 14079-14084 (1999).

191 C.H. Meyer, J.M. Pauly, A. Macovski, D.G. Nishimura, "Simultaneous Spatial and Spectral Selective Excitation," Magnet Reson Med **15**, 287-304 (1990).

192 C.J. Hardy, P.A. Bottomley, M. Odonnell, P. Roemer, "Optimization of Two-Dimensional Spatially Selective Nmr Pulses by Simulated Annealing," J Magn Reson **77**, 233-250 (1988).

193 E.U. Saritas, C.H. Cunningham, J.H. Lee, E.T. Han, D.G. Nishimura, "DWI of the spinal cord with reduced FOV single-shot EPI," Magnet Reson Med **60**, 468-473 (2008).

194 B.J. Wilm, J. Svensson, A. Henning, K.P. Pruessmann, P. Boesiger, S.S. Kollias, "Reduced field-of-view MRI using outer volume suppression for spinal cord diffusion imaging," Magnet Reson Med **57**, 625-630 (2007).

195 T.S. Ibrahim, R. Lee, B.A. Baertlein, A.M. Abduljalil, H. Zhu, P.M.L. Robitaille, "Effect of RF coil excitation on field inhomogeneity at ultra high fields: A field optimized TEM resonator," Magn Reson Imaging **19**, 1339-1347 (2001).

196 Y.D. Zhu, "Parallel excitation with an array of transmit coils," Magnet Reson Med **51**,

775-784 (2004).
197 U. Katscher, P. Bornert, C. Leussler, J.S. van den Brink, "Transmit SENSE," Magnet Reson Med **49**, 144-150 (2003).
198 C.S.A. de Castro, M.P. Luttje, M. van Vulpen, P.R. Luijten, U.A. van der Heide, D.W.J. Klomp, "Composite slice-selective adiabatic excitation for prostate MRSI," Nmr Biomed **26**, 436-442 (2013).
199 R. Ouwerkerk, R.G. Weiss, P.A. Bottomley, "Measuring human cardiac tissue sodium concentrations using surface coils, adiabatic excitation, and twisted projection imaging with minimal T-2 losses," J Magn Reson Imaging **21**, 546-555 (2005).
200 L. Biasiolli, Lindsay AC, Choudhury RP, Robson MD, presented at the J Cardiov Magn Reson, Orlando, FL, USA, 2012 (unpublished).
201 D.W. Klomp, T.W. Scheenen, C.S. Arteaga, J. van Asten, V.O. Boer, P.R. Luijten, "Detection of fully refocused polyamine spins in prostate cancer at 7 T," Nmr Biomed **24**, 299-306 (2011).
202 A.J. Dick, V.K. Raman, A.N. Raval, M.A. Guttman, R.B. Thompson, C. Ozturk, D.C. Peters, A.M. Stine, V.J. Wright, W.H. Schenke, R.J. Lederman, "Invasive human magnetic resonance imaging: feasibility during revascularization in a combined XMR suite," Catheter Cardiovasc Interv **64**, 265-274 (2005).
203 X. Yang, B.D. Bolster, Jr., D.L. Kraitchman, E. Atalar, "Intravascular MR-monitored balloon angioplasty: an in vivo feasibility study," J Vasc Interv Radiol **9**, 953-959 (1998).
204 A. Arepally, P.V. Karmarkar, C. Weiss, E.R. Rodriguez, R.J. Lederman, E. Atalar, "Magnetic resonance image-guided trans-septal puncture in a swine heart," J Magn Reson Imaging **21**, 463-467 (2005).
205 B.A. Hargreaves, C.H. Cunningham, D.G. Nishimura, S.M. Conolly, "Variable-rate selective excitation for rapid MRI sequences," Magnet Reson Med **52**, 590-597 (2004).
206 A. Tanaka, T. Imanishi, H. Kitabata, T. Kubo, S. Takarada, T. Tanimoto, A. Kuroi, H. Tsujioka, H. Ikejima, S. Ueno, H. Kataiwa, K. Okouchi, M. Kashiwaghi, H. Matsumoto, K. Takemoto, N. Nakamura, K. Hirata, M. Mizukoshi, T. Akasaka, "Morphology of exertion-triggered plaque rupture in patients with acute coronary syndrome: an optical coherence tomography study," Circulation **118**, 2368-2373 (2008).
207 L. Cruz, B. Urbanc, S.V. Buldyrev, R. Christie, T. GomezIsla, S. Havlin, M. McNamara, H.E. Stanley, B.T. Hyman, "Aggregation and disaggregation of senile plaques in Alzheimer disease," P Natl Acad Sci USA **94**, 7612-7616 (1997).
208 J.B. Johnson, "Thermal agitation of electricity in conductors," Physical Review **32**, 97-109 (1928).
209 H. Nyquist, "Thermal agitation of electric charge in conductors," Physical Review **32**, 110-113 (1928).
210 D.M. Pozar, *Microwave Engineering*, 3 ed. (John Wiley & Sons, Inc., New York, 2005).
211 K.L. Carr, "Microwave Radiometry - Its Importance to the Detection of Cancer," Ieee Transactions on Microwave Theory and Techniques **37**, 1862-1869 (1989).
212 K.L. Carr, "Microwave Radiometry ... Noninvasive Measurement of Temperature at Depth," 29th Microwave Power Symposium - Proceedings, 3-4 (1994).
213 K. Toutouzas, M. Drakopoulou, C. Aggeli, C. Nikolaou, I. Felekos, H. Grassos, A. Synetos, K. Stathogiannis, A. Karanasos, E. Tsiamis, E. Siores, C. Stefanadis, "In vivo measurement of plaque neovascularisation and thermal heterogeneity in intermediate lesions of

human carotid arteries," Heart **98**, 1716-1721 (2012).

[214] A.M. El-Sharkawy, P.P. Sotiriadis, P.A. Bottomley, E. Atalar, "Absolute Temperature Monitoring Using RF Radiometry in the MRI Scanner," IEEE Trans Circuits Syst I Regul Pap **53**, 2396-2404 (2006).

[215] C.I. Yeung, R.C. Susil, E. Atalar, "RF safety of wires in interventional MRI: Using a safety index," Proceedings of the 23rd Annual International Conference of the Ieee Engineering in Medicine and Biology Society, Vols 1-4 **23**, 2496-2498 (2001).

[216] E. Atalar, "Radiofrequency safety for interventional MRI procedures," Academic Radiology **12**, 1149-1157 (2005).

[217] W.R. Nitz, A. Oppelt, W. Renz, C. Manke, M. Lenhart, J. Link, "On the heating of linear conductive structures as guide wires and catheters in interventional MRI," J Magn Reson Imaging **13**, 105-114 (2001).

[218] B.S. Qiu, A.M. El-Sharkawy, V. Paliwal, P. Karmarkar, F.B. Gao, E. Atalar, X.M. Yang, "Simultaneous radiofrequency (RF) heating and magnetic resonance (MR) thermal mapping using an intravascular MR imaging/RF heating system," Magnet Reson Med **54**, 226-230 (2005).

[219] A. Kolandaivelu, M.M. Zviman, V. Castro, A.C. Lardo, R.D. Berger, H.R. Halperin, "Noninvasive Assessment of Tissue Heating During Cardiac Radiofrequency Ablation Using MRI Thermography," Circ-Arrhythmia Elec **3**, 521-U134 (2010).

[220] J.S. Lewin, C.F. Connell, J.L. Duerk, Y.C. Chung, M.E. Clampitt, J. Spisak, G.S. Gazelle, J.R. Haaga, "Interactive MRI-guided radiofrequency interstitial thermal ablation of abdominal tumors: clinical trial for evaluation of safety and feasibility," J Magn Reson Imaging **8**, 40-47 (1998).

[221] D.I. Hoult, "The principle of reciprocity in signal strength calculations - A mathematical guide," Concept Magnetic Res **12**, 173-187 (2000).

[222] E.A. Cheever, K.R. Foster, "Microwave Radiometry in Living Tissue - What Does It Measure," Ieee Transactions on Biomedical Engineering **39**, 563-568 (1992).

[223] K. Ridaoui, A. Mamouni, R.A. Abdelmalek, B. Bocquet, Y. Leroy, "Near-Field Weighting Functions for Microwave Radiometric Signals," Ieee Transactions on Magnetics **31**, 2166-2169 (1995).

[224] R.H. Dicke, "The Measurement of Thermal Radiation at Microwave Frequencies," Review of Scientific Instruments **17**, 268-275 (1946).

[225] H.H. Pennes, "Analysis of Tissue and Arterial Blood Temperatures in the Resting Human Forearm," Journal of Applied Physiology **1**, 93-122 (1948).

[226] H.L.M. Cheng, D.B. Plewes, "Tissue thermal conductivity by magnetic resonance thermometry and focused ultrasound heating," J Magn Reson Imaging **16**, 598-609 (2002).

[227] J.L. Dillenseger, S. Esneault, "Fast FFT-based bioheat transfer equation computation," Computers in Biology and Medicine **40**, 119-123 (2010).

[228] N.E. Hasgall PA, Gosselin MC, Klingenböck A, Kuster N, "IT'IS Database for thermal and electromagnetic parameters of biological tissues, version 2.4," (July 30th, 2013 www.itis.ethz.ch/database).

[229] J.Q. Wang, O. Fujiwara, "FDTD computation of temperature rise in the human head for portable telephones," Ieee T Microw Theory **47**, 1528-1534 (1999).

[230] A. Trakic, S. Crozier, F. Liu, "Numerical modelling of thermal effects in rats due to high-

field magnetic resonance imaging (0.5-1 GHz)," Phys Med Biol **49**, 5547-5558 (2004).

[231] "Guidance for Industry and FDA Staff Criteria for Significant Risk Investigations of Magnetic Resonance Diagnostic Devices," edited by F.a.D.A. U.S. Department of Health and Human Services, Center for Devices and Radiological Health. (July 14, 2003 (http://www.fda.gov/downloads/MedicalDevices/DeviceRegulationandGuidance/GuidanceDocuments/UCM072688.pdf)).

[232] T.S. Sandhu, "Measurement of Blood-Flow Using Temperature Decay - Effect of Thermal Conduction," Int J Radiat Oncol **12**, 373-378 (1986).

[233] T.V. Samulski, P. Fessenden, R. Valdagni, D.S. Kapp, "Correlations of Thermal Washout Rate, Steady-State Temperatures, and Tissue-Type in Deep Seated Recurrent or Metastatic Tumors," Int J Radiat Oncol **13**, 907-916 (1987).

[234] J.C. Chato, "Measurement of thermal properties of growing tumors," Ann N Y Acad Sci **335**, 67-85 (1980).

[235] P.S. Yarmolenko, E.J. Moon, C. Landon, A. Manzoor, D.W. Hochman, B.L. Viglianti, M.W. Dewhirst, "Thresholds for thermal damage to normal tissues: An update," International Journal of Hyperthermia **27**, 320-343 (2011).

[236] M.A. Erturk, P.A. Bottomley, A.M. El-Sharkawy, "Denoising MRI using spectral subtraction," IEEE Trans Biomed Eng **60**, 1556-1562 (2013).

[237] M.A. Erturk, Bottomley. P. A., El-Sharkawy, A-M. M., presented at the 6th Cairo International Biomedical Engineering Conference, Cairo, Egypt, 2012 (unpublished).

# Curriculum Vita

*M. Arcan Ertürk*

**Personal Information**

Date and Place of Birth: July 27, 1988; Ankara, Turkey
email: arcanerturk@gmail.com
personal website: http://www.mri.jhu.edu/~arcanm/

**Educational Background**

**Ph.D**. 2014 Johns Hopkins University, Baltimore, MD, USA
**M.Sc.** 2011 Johns Hopkins University, Baltimore, MD, USA
Electrical & Computer Engineering,
Advisor: Paul A. Bottomley, PhD

**B.Sc.** 2009 Bilkent University, Ankara, Turkey
Electrical & Electronics Engineering
Advisor: Ergin Atalar, PhD

**Publications**

*Journal Papers*

1. **M. Arcan Erturk**, AbdEl-Monem M. El-Sharkawy, Paul A. Bottomley. *"Monitoring Local Heating Around an Interventiona MRI Antenna with RF Radiometry"*. Medical Physics, (under review).

2. **M. Arcan Erturk**, AbdEl-Monem M. El-Sharkawy, Jay Moore, Paul A. Bottomley. *"7 Tesla MRI with a Transmit/Receive Loopless Antenna and $B_1$-Insensitive Selective Excitation"*. Magnetic Resonance in Medicine, published online: August 20, 2013.

3. **M. Arcan Erturk**, Paul A. Bottomley, AbdEl-Monem M. El-Sharkawy. *"Denoising MRI Using Spectral Subtraction"*. IEEE Transactions on Biomedical Engineering, Volume 60, No. 6, pages 1556-1562, June 2013.

4. **M. Arcan Erturk**, AbdEl-Monem M. El-Sharkawy, Paul A. Bottomley. *"Interventional loopless antenna at 7 T"*. Magnetic Resonance in Medicine, Volume 68, Issue 3, pages 980-988, Sep 2012.

*Conference Abstracts and Papers*

1. **M. Arcan Erturk**, AbdEl-Monem M. El-Sharkawy, Paul A. Bottomley. *"Monitoring local heating around an interventional probe with RF radiometry"*. ISMRM 22nd Scientific Meeting & Exhibition, Milan, Italy, (May 2014). (traditional poster)

2. Guan Wang, **M. Arcan Erturk**, Shashank S. Hegde, Paul A. Bottomley. *"High-resolution multi-parametric characterization of atherosclerotic lesions with 3T intravascular MRI"*. ISMRM 22nd Scientific Meeting & Exhibition, Milan, Italy, (May 2014). (traditional poster)

3. **M. Arcan Erturk**, AbdEl-Monem M. El-Sharkawy. *"Characterizing bazooka baluns"*. ISMRM 21st Scientific Meeting & Exhibition, Salt Lake City USA, (Apr 2013). (educational e-poster)

4. Shashank S. Hegde, Clifford R. Weiss, **M. Arcan Erturk**, Paul A. Bottomley. *"3T intravascular MRI, IVUS and OCT: A study in contrast"*. ISMRM 21st Scientific Meeting & Exhibition, Salt Lake City USA, (Apr 2013). (traditional poster)

5. **M. Arcan Erturk**, Bottomley PA, AbdEl-Monem M. El-Sharkawy. *"Spectral Subtraction De-noising of MRI"*. 6th Cairo International Biomedical Engineering Conference (Dec 2012). (oral presentation)

6. **M. Arcan Erturk**, AbdEl-Monem M. El-Sharkawy, Jay Moore, Paul A. Bottomley. *"Interventional MRI 'Endoscopy' Using a Transmit/Receive Loopless Antenna at 7 Tesla"*. 9th Interventional MRI Symposium, p52, Boston USA, (Sep 2012). (oral presentation)

7. **M. Arcan Erturk**, AbdEl-Monem M. El-Sharkawy, Paul A. Bottomley. *"The Interventional Loopless Antenna at 7 Tesla"*. ISMRM 20th Scientific Meeting & Exhibition, p2944, Melbourne Australia, (May 2012). (e-poster)

**JOHN WILEY AND SONS LICENSE**
**TERMS AND CONDITIONS**

Feb 16, 2014

This is a License Agreement between Mehmet A Erturk ("You") and John Wiley and Sons ("John Wiley and Sons") provided by Copyright Clearance Center ("CCC"). The license consists of your order details, the terms and conditions provided by John Wiley and Sons, and the payment terms and conditions.

**All payments must be made in full to CCC. For payment instructions, please see information listed at the bottom of this form.**

| | |
|---|---|
| License Number | 3330580002487 |
| License date | Feb 16, 2014 |
| Licensed content publisher | John Wiley and Sons |
| Licensed content publication | Magnetic Resonance in Medicine |
| Licensed content title | Interventional loopless antenna at 7 T |
| Licensed copyright line | Copyright © 2011 Wiley Periodicals, Inc. |
| Licensed content author | Mehmet Arcan Ertürk,AbdEl-Monem M. El-Sharkawy,Paul A. Bottomley |
| Licensed content date | Dec 12, 2011 |
| Start page | 980 |
| End page | 988 |
| Type of use | Dissertation/Thesis |
| Requestor type | Author of this Wiley article |
| Format | Print and electronic |
| Portion | Full article |
| Will you be translating? | No |
| Title of your thesis / dissertation | ENABLING INTERVENTIONAL MRI USING LOOPLESS ANTENNA AT ULTRA-HIGH FIELD |
| Expected completion date | Mar 2014 |
| Expected size (number of pages) | 180 |
| Total | 0.00 USD |
| Terms and Conditions | |

## TERMS AND CONDITIONS

This copyrighted material is owned by or exclusively licensed to John Wiley & Sons, Inc. or one of its group companies (each a "Wiley Company") or a society for whom a Wiley Company has exclusive publishing rights in relation to a particular journal (collectively "WILEY"). By clicking

**JOHN WILEY AND SONS LICENSE**
**TERMS AND CONDITIONS**

Feb 16, 2014

This is a License Agreement between Mehmet A Erturk ("You") and John Wiley and Sons ("John Wiley and Sons") provided by Copyright Clearance Center ("CCC"). The license consists of your order details, the terms and conditions provided by John Wiley and Sons, and the payment terms and conditions.

**All payments must be made in full to CCC. For payment instructions, please see information listed at the bottom of this form.**

| | |
|---|---|
| License Number | 3330571380547 |
| License date | Feb 16, 2014 |
| Licensed content publisher | John Wiley and Sons |
| Licensed content publication | Magnetic Resonance in Medicine |
| Licensed content title | 7 Tesla MRI with a transmit/receive loopless antenna and B1-insensitive selective excitation |
| Licensed copyright line | Copyright © 2013 Wiley Periodicals, Inc. |
| Licensed content author | M. Arcan Erturk,AbdEl-Monem M. El-Sharkawy,Jay Moore,Paul A. Bottomley |
| Licensed content date | Aug 20, 2013 |
| Start page | n/a |
| End page | n/a |
| Type of use | Dissertation/Thesis |
| Requestor type | Author of this Wiley article |
| Format | Print and electronic |
| Portion | Full article |
| Will you be translating? | No |
| Title of your thesis / dissertation | ENABLING INTERVENTIONAL MRI USING LOOPLESS ANTENNA AT ULTRA-HIGH FIELD |
| Expected completion date | Mar 2014 |
| Expected size (number of pages) | 180 |
| Total | 0.00 USD |
| Terms and Conditions | |

## TERMS AND CONDITIONS

This copyrighted material is owned by or exclusively licensed to John Wiley & Sons, Inc. or one of its group companies (each a "Wiley Company") or a society for whom a Wiley Company has

exclusive publishing rights in relation to a particular journal (collectively "WILEY"). By clicking "accept" in connection with completing this licensing transaction, you agree that the following terms and conditions apply to this transaction (along with the billing and payment terms and conditions established by the Copyright Clearance Center Inc., ("CCC's Billing and Payment terms and conditions"), at the time that you opened your RightsLink account (these are available at any time at http://myaccount.copyright.com).

**Terms and Conditions**

1. The materials you have requested permission to reproduce (the "Materials") are protected by copyright.

2.You are hereby granted a personal, non-exclusive, non-sublicensable, non-transferable, worldwide, limited license to reproduce the Materials for the purpose specified in the licensing process. This license is for a one-time use only with a maximum distribution equal to the number that you identified in the licensing process. Any form of republication granted by this license must be completed within two years of the date of the grant of this license (although copies prepared before may be distributed thereafter). The Materials shall not be used in any other manner or for any other purpose. Permission is granted subject to an appropriate acknowledgement given to the author, title of the material/book/journal and the publisher. You shall also duplicate the copyright notice that appears in the Wiley publication in your use of the Material. Permission is also granted on the understanding that nowhere in the text is a previously published source acknowledged for all or part of this Material. Any third party material is expressly excluded from this permission.

3. With respect to the Materials, all rights are reserved. Except as expressly granted by the terms of the license, no part of the Materials may be copied, modified, adapted (except for minor reformatting required by the new Publication), translated, reproduced, transferred or distributed, in any form or by any means, and no derivative works may be made based on the Materials without the prior permission of the respective copyright owner. You may not alter, remove or suppress in any manner any copyright, trademark or other notices displayed by the Materials. You may not license, rent, sell, loan, lease, pledge, offer as security, transfer or assign the Materials, or any of the rights granted to you hereunder to any other person.

4. The Materials and all of the intellectual property rights therein shall at all times remain the exclusive property of John Wiley & Sons Inc or one of its related companies (WILEY) or their respective licensors, and your interest therein is only that of having possession of and the right to reproduce the Materials pursuant to Section 2 herein during the continuance of this Agreement. You agree that you own no right, title or interest in or to the Materials or any of the intellectual property rights therein. You shall have no rights hereunder other than the license as provided for above in Section 2. No right, license or interest to any trademark, trade name, service mark or other branding ("Marks") of WILEY or its licensors is granted hereunder, and you agree that you shall not assert any such right, license or interest with respect thereto.

5. NEITHER WILEY NOR ITS LICENSORS MAKES ANY WARRANTY OR REPRESENTATION OF ANY KIND TO YOU OR ANY THIRD PARTY, EXPRESS,

IMPLIED OR STATUTORY, WITH RESPECT TO THE MATERIALS OR THE ACCURACY OF ANY INFORMATION CONTAINED IN THE MATERIALS, INCLUDING, WITHOUT LIMITATION, ANY IMPLIED WARRANTY OF MERCHANTABILITY, ACCURACY, SATISFACTORY QUALITY, FITNESS FOR A PARTICULAR PURPOSE, USABILITY, INTEGRATION OR NON-INFRINGEMENT AND ALL SUCH WARRANTIES ARE HEREBY EXCLUDED BY WILEY AND ITS LICENSORS AND WAIVED BY YOU.

6. WILEY shall have the right to terminate this Agreement immediately upon breach of this Agreement by you.

7. You shall indemnify, defend and hold harmless WILEY, its Licensors and their respective directors, officers, agents and employees, from and against any actual or threatened claims, demands, causes of action or proceedings arising from any breach of this Agreement by you.

8. IN NO EVENT SHALL WILEY OR ITS LICENSORS BE LIABLE TO YOU OR ANY OTHER PARTY OR ANY OTHER PERSON OR ENTITY FOR ANY SPECIAL, CONSEQUENTIAL, INCIDENTAL, INDIRECT, EXEMPLARY OR PUNITIVE DAMAGES, HOWEVER CAUSED, ARISING OUT OF OR IN CONNECTION WITH THE DOWNLOADING, PROVISIONING, VIEWING OR USE OF THE MATERIALS REGARDLESS OF THE FORM OF ACTION, WHETHER FOR BREACH OF CONTRACT, BREACH OF WARRANTY, TORT, NEGLIGENCE, INFRINGEMENT OR OTHERWISE (INCLUDING, WITHOUT LIMITATION, DAMAGES BASED ON LOSS OF PROFITS, DATA, FILES, USE, BUSINESS OPPORTUNITY OR CLAIMS OF THIRD PARTIES), AND WHETHER OR NOT THE PARTY HAS BEEN ADVISED OF THE POSSIBILITY OF SUCH DAMAGES. THIS LIMITATION SHALL APPLY NOTWITHSTANDING ANY FAILURE OF ESSENTIAL PURPOSE OF ANY LIMITED REMEDY PROVIDED HEREIN.

9. Should any provision of this Agreement be held by a court of competent jurisdiction to be illegal, invalid, or unenforceable, that provision shall be deemed amended to achieve as nearly as possible the same economic effect as the original provision, and the legality, validity and enforceability of the remaining provisions of this Agreement shall not be affected or impaired thereby.

10. The failure of either party to enforce any term or condition of this Agreement shall not constitute a waiver of either party's right to enforce each and every term and condition of this Agreement. No breach under this agreement shall be deemed waived or excused by either party unless such waiver or consent is in writing signed by the party granting such waiver or consent. The waiver by or consent of a party to a breach of any provision of this Agreement shall not operate or be construed as a waiver of or consent to any other or subsequent breach by such other party.

11. This Agreement may not be assigned (including by operation of law or otherwise) by you without WILEY's prior written consent.

12. Any fee required for this permission shall be non-refundable after thirty (30) days from receipt

13. These terms and conditions together with CCC's Billing and Payment terms and conditions (which are incorporated herein) form the entire agreement between you and WILEY concerning

this licensing transaction and (in the absence of fraud) supersedes all prior agreements and representations of the parties, oral or written. This Agreement may not be amended except in writing signed by both parties. This Agreement shall be binding upon and inure to the benefit of the parties' successors, legal representatives, and authorized assigns.

14. In the event of any conflict between your obligations established by these terms and conditions and those established by CCC's Billing and Payment terms and conditions, these terms and conditions shall prevail.

15. WILEY expressly reserves all rights not specifically granted in the combination of (i) the license details provided by you and accepted in the course of this licensing transaction, (ii) these terms and conditions and (iii) CCC's Billing and Payment terms and conditions.

16. This Agreement will be void if the Type of Use, Format, Circulation, or Requestor Type was misrepresented during the licensing process.

17. This Agreement shall be governed by and construed in accordance with the laws of the State of New York, USA, without regards to such state's conflict of law rules. Any legal action, suit or proceeding arising out of or relating to these Terms and Conditions or the breach thereof shall be instituted in a court of competent jurisdiction in New York County in the State of New York in the United States of America and each party hereby consents and submits to the personal jurisdiction of such court, waives any objection to venue in such court and consents to service of process by registered or certified mail, return receipt requested, at the last known address of such party.

**Wiley Open Access Terms and Conditions**

Wiley publishes Open Access articles in both its Wiley Open Access Journals program [http://www.wileyopenaccess.com/view/index.html] and as Online Open articles in its subscription journals. The majority of Wiley Open Access Journals have adopted the Creative Commons Attribution License (CC BY) which permits the unrestricted use, distribution, reproduction, adaptation and commercial exploitation of the article in any medium. No permission is required to use the article in this way provided that the article is properly cited and other license terms are observed. A small number of Wiley Open Access journals have retained the Creative Commons Attribution Non Commercial License (CC BY-NC), which permits use, distribution and reproduction in any medium, provided the original work is properly cited and is not used for commercial purposes.

Online Open articles - Authors selecting Online Open are, unless particular exceptions apply, offered a choice of Creative Commons licenses. They may therefore select from the CC BY, the CC BY-NC and the Attribution-NoDerivatives (CC BY-NC-ND). The CC BY-NC-ND is more restrictive than the CC BY-NC as it does not permit adaptations or modifications without rights holder consent.

Wiley Open Access articles are protected by copyright and are posted to repositories and websites in accordance with the terms of the applicable Creative Commons license referenced on the article. At the time of deposit, Wiley Open Access articles include all changes made during peer review, copyediting, and publishing. Repositories and websites that host the article are responsible

for incorporating any publisher-supplied amendments or retractions issued subsequently.
Wiley Open Access articles are also available without charge on Wiley's publishing platform, **Wiley Online Library** or any successor sites.

Conditions applicable to all Wiley Open Access articles:

- The authors' moral rights must not be compromised. These rights include the right of "paternity" (also known as "attribution" - the right for the author to be identified as such) and "integrity" (the right for the author not to have the work altered in such a way that the author's reputation or integrity may be damaged).

- Where content in the article is identified as belonging to a third party, it is the obligation of the user to ensure that any reuse complies with the copyright policies of the owner of that content.

- If article content is copied, downloaded or otherwise reused for research and other purposes as permitted, a link to the appropriate bibliographic citation (authors, journal, article title, volume, issue, page numbers, DOI and the link to the definitive published version on Wiley Online Library) should be maintained. Copyright notices and disclaimers must not be deleted.
    - Creative Commons licenses are copyright licenses and do not confer any other rights, including but not limited to trademark or patent rights.

- Any translations, for which a prior translation agreement with Wiley has not been agreed, must prominently display the statement: "This is an unofficial translation of an article that appeared in a Wiley publication. The publisher has not endorsed this translation."

**Conditions applicable to non-commercial licenses (CC BY-NC and CC BY-NC-ND)**

For non-commercial and non-promotional purposes individual non-commercial users may access, download, copy, display and redistribute to colleagues Wiley Open Access articles. In addition, articles adopting the CC BY-NC may be adapted, translated, and text- and data-mined subject to the conditions above.

**Use by commercial "for-profit" organizations**

Use of non-commercial Wiley Open Access articles for commercial, promotional, or marketing purposes requires further explicit permission from Wiley and will be subject to a fee. Commercial purposes include:

- Copying or downloading of articles, or linking to such articles for further redistribution, sale or licensing;

- Copying, downloading or posting by a site or service that incorporates advertising with such content;

- The inclusion or incorporation of article content in other works or services (other than normal quotations with an appropriate citation) that is then available for sale or licensing, for a fee (for example, a compilation produced for marketing purposes, inclusion in a sales pack)

- Use of article content (other than normal quotations with appropriate citation) by for-profit organizations for promotional purposes

- Linking to article content in e-mails redistributed for promotional, marketing or educational purposes;

- Use for the purposes of monetary reward by means of sale, resale, license, loan, transfer or other form of commercial exploitation such as marketing products

- Print reprints of Wiley Open Access articles can be purchased from: corporatesales@wiley.com

The modification or adaptation for any purpose of an article referencing the CC BY-NC-ND License requires consent which can be requested from RightsLink@wiley.com .

Other Terms and Conditions:

BY CLICKING ON THE "I AGREE..." BOX, YOU ACKNOWLEDGE THAT YOU HAVE READ AND FULLY UNDERSTAND EACH OF THE SECTIONS OF AND PROVISIONS SET FORTH IN THIS AGREEMENT AND THAT YOU ARE IN AGREEMENT WITH AND ARE WILLING TO ACCEPT ALL OF YOUR OBLIGATIONS AS SET FORTH IN THIS AGREEMENT.

**v1.8**

**If you would like to pay for this license now, please remit this license along with your payment made payable to "COPYRIGHT CLEARANCE CENTER" otherwise you will be invoiced within 48 hours of the license date. Payment should be in the form of a check or money order referencing your account number and this invoice number RLNK501227383. Once you receive your invoice for this order, you may pay your invoice by credit card. Please follow instructions provided at that time.**

**Make Payment To:**
**Copyright Clearance Center**
**Dept 001**
**P.O. Box 843006**